



TECHNISCHE  
UNIVERSITÄT  
WIEN

Dissertation

# Experimental Studies on Combustion of Jet, Automotive and Alternative Fuels

ausgeführt unter der Anleitung von

**Ao.Univ.Prof. Dipl.-Ing Dr.techn. Ernst Pucher**

Institut für Fahrzeugantriebe und Automobiltechnik  
Technische Universität Wien

und

**Prof. Dr. Kalyanasundaram Seshadri**

Department of Mechanical and Aerospace Engineering  
University of California, San Diego

eingereicht an der Technischen Universität Wien  
Fakultät für Maschinenwesen und Betriebswissenschaften

von

**Gerald Mairinger**

Matrikel Nr. 0657700

Tischlerweg 3

A – 4064 Oftering

Wien, April 2018

Dissertation

# **Experimental Studies on Combustion of Jet, Automotive and Alternative Fuels**

**Gerald Mairinger**

Institute for Powertrains and Automotive Technology  
Faculty of Mechanical and Industrial Engineering

Vienna University of Technology

Advisors:

**Ao. Univ-Prof. Dipl.-Ing. Dr.techn. Ernst Pucher**

Institute for Powertrains and Automotive Technology  
Vienna University of Technology, Austria

**Prof. Dr. Kalyanasundaram Seshadri**

Department of Mechanical and Aerospace Engineering  
University of California, San Diego, USA

Vienna, April 2018

Ich nehme zur Kenntnis, dass ich zur Drucklegung meiner Arbeit unter der Bezeichnung

**Dissertation**

nur mit Bewilligung der Prüfungskommission berechtigt bin.

*Eidesstattliche Erklärung*

Ich erkläre an Eides statt, dass die vorliegende Arbeit nach den anerkannten Grundsätzen für wissenschaftliche Abhandlungen von mir selbstständig erstellt wurde. Alle verwendeten Hilfsmittel, insbesondere die zugrunde gelegte Literatur, sind in dieser Arbeit genannt und aufgelistet. Die aus den Quellen wörtlich entnommenen Stellen, sind als solche kenntlich gemacht.

Das Thema dieser Arbeit wurde von mir bisher weder im In- noch Ausland einer Beurteilerin/einem Beurteiler zur Begutachtung in irgendeiner Form als Prüfungsarbeit vorgelegt. Diese Arbeit stimmt mit der von den Begutachterinnen/Begutachtern beurteilten Arbeit überein.

Wien, April, 2018

---

*Unterschrift*

© Copyright  
Gerald Mairinger, 2018  
All rights reserved

## Abstract

Experimental and computational studies are carried out to elucidate the fundamental characteristics of hydrocarbon diffusion flames. The motivation for this study is to increase the knowledge of combustion processes of hydrocarbon fuels and help to develop clean and efficient future combustion devices. The counterflow configuration is employed to carry out experimental investigations at atmospheric and elevated pressures. This configuration provides a simple and accurate way to conduct research on one-dimensional diffusion flame and enforce boundary conditions defined in computational models. The hydrocarbon fuels considered in this dissertation involve aviation, automotive type gasoline and alternative fuels.

The aviation fuels investigated in this study are three jet fuels, commercial and military grade, three jet fuel surrogates and three n-paraffin hydrocarbons. This research project is supported by the U.S. Army Research Office (ARO) to further the U.S. Army Single Fuel Forward policy. For this purpose, a new counterflow burner is designed, which allows for conducting experiments on autoignition characteristics of high molecular weight hydrocarbon fuels at elevated pressures. Experiments are carried out in the pressure range of 3 to 6 bar to elucidate the effect of pressure on autoignition characteristics of these fuels. The obtained experimental data is compared to numerical computations carried out in collaboration with the Creck modeling group at the Polytechnic University of Milan. The results show a decrease in autoignition temperature with increasing pressure. Low-temperature chemistry is found to play an important role in promoting autoignition. It is observed, that the influence of low-temperature chemistry increases with increasing pressure.

The gasoline fuels investigated are the so called Fuels for Advanced Combustion Engines (FACE). These fuels were formulated to provide researches around the globe with a set of gasoline test fuels for better comparison of their experimental results. The atmospheric counterflow configuration is employed to study the autoignition and extinction characteristics for varying reactant stream strain rates. The liquid fuel is first vaporized and then diluted with gaseous nitrogen before it enters the counterflow burner. The results are compared with numerical simulations

## Abstract

carried out in collaboration with the Combustion and Pyrolysis Group from the King Abdullah University of Science and Technology in Saudi Arabia. The results show good agreement between the numerical simulations and the obtained experimental data, for both the limits of critical conditions for autoignition and extinction.

The alternative fuel investigated is dimethyl ether. The experiment is carried out employing the atmospheric counterflow configuration to elucidate the influence of stoichiometric mixture fraction and adiabatic flame temperature on extinction behavior of non-premixed dimethyl-ether flames. The mass fractions for fuel and oxidizer are chosen, so that the adiabatic flame temperature is fixed. The value for the stoichiometric mixture fraction in this experiment ranges from 0.1 to 0.8. The strain rate at extinction is measured as a function of the stoichiometric mixture fraction. With the stoichiometric mixture fraction increasing, the strain rate at extinction is first found to decrease and then increase. The experimental results are compared with numerical computations with detailed chemistry, carried out in collaboration with colleagues from the Indian Institute of Technology Madras. The predictions agree with the experimental data for small values of the stoichiometric mixture fraction but significantly disagree for higher values of the stoichiometric mixture fraction.

## Kurzfassung

Bei den in dieser Arbeit durchgeführten Studien handelt es sich um experimentelle und simulationstechnische Untersuchungen zu den Verbrennungseigenschaften von Kohlenwasserstoffen. Das Ziel der durchgeführten experimentellen Untersuchungen ist das Schaffen von Grundlagenwissen zu Phänomenen der Verbrennung von Kohlenwasserstoffen um die Entwicklung zukünftiger effizienter und schadstoffarmer Verbrennungskraftmaschinen zu unterstützen. Die experimentellen Untersuchungen werden an einem sogenannten Gegenstrombrenner durchgeführt. Der Versuchsaufbau besteht aus zwei vertikal angeordneten gegenüberliegenden Auslässen. Aus der oben liegenden Düse tritt ein gasförmiger Oxidator aus, aus dem untenliegenden Auslass tritt je nach Konfiguration ein gasförmiger oder flüssiger Brennstoff aus. In der Mitte des Strömungsfelds bildet sich eine nicht vorgemischte, laminare und stabile Flamme aus. Ein konzentrisch angeordneter Strom aus gasförmigen Stickstoff auf beiden Seiten des Brenners schützt die Reaktionszone von der Umgebung. Durch die simple Geometrie eines solchen Brenners und dadurch wohldefinierten Randbedingungen, eignen sich die dadurch gewonnen Ergebnisse für die Validierung von numerischen Simulationen. Bei den in dieser Arbeit berücksichtigten Kraftstoffen handelt es sich um militärische und zivile Luftfahrttreibstoffe, Benzin-kraftstoffe und einen alternativen Kraftstoff welche an zwei verschiedenen Gegenstrombrennerkonfigurationen bei atmosphärischen und erhöhten Drücken untersucht werden.

Die untersuchten Luftfahrkraftstoffe sind die beiden militärischen Kraftstoffe JP-8 und JP-5 und der zivile Kraftstoff Jet-A. Zusätzlich werden drei verschiedene Ersatzkraftstoffe und deren Komponenten auf das Selbstentflammungsverhalten bei erhöhten Drücken untersucht. Dafür wird die bereits existierende *UC San Diego High Pressure Experimental Combustion Facility (HPCEF)* weiterentwickelt und mit einem neuentwickelten Gegenstrombrenner ausgestattet, welcher das Durchführen von Selbstentzündungsexperimenten mit hochmolekularen flüssigen Treibstoffen bis zu Drücken von 25 bar ermöglicht. Dabei wird ein heißer Oxidator auf ein mit flüssigen Kraftstoff gefülltes Becken geleitet. Die Temperatur wird bei konstanter *Strain Rate* solange erhöht bis Selbstentzündung eintritt. Die Oxidatortemperatur wird dabei kontinuierlich

gemessen. Unterstützt wird dieses Forschungsprojekt vom *U.S. Army Research Office (ARO)*. Gewonnene experimentellen Daten werden mit numerischen Simulationen verglichen, welche gemeinsam mit Kollegen der Creck Modelling Group des Polytechnikum Mailand durchgeführt werden. Die Ergebnisse zeigen eine Abnahme der Selbstentzündungstemperaturen bei steigendem Druck für alle untersuchten Kraftstoffe. Gemeinsam mit den durchgeführten numerischen Untersuchungen deuten die experimentellen Ergebnisse auf einen entscheidenden Einfluss von Niedertemperatur-Chemie auf das Zündverhalten hin.

Bei den untersuchten Benzinkraftstoffen handelt es sich um die sogenannten *Fuels for Advanced Combustion Engines (FACE)*, sechs standardisierte Ottokraftstoffe welche entwickelt wurden um die Vergleichbarkeit von experimentellen Ergebnissen verschiedener Forschungseinrichtungen zu verbessern. Die Experimente werden an einem Gegenstrombrenner bei atmosphärischen Bedingungen durchgeführt. Der bei Raumtemperatur flüssig vorliegende Kraftstoff wird dabei in einem Verdampfer verdampft, mit gasförmigen Stickstoff vermischt und dem Brenner zugeführt. Als Oxidator diene reine Luft. Ziel der Untersuchung ist das Selbstentzündungs- und Auslöschverhalten bei kritischen Bedingungen. Die gewonnen Daten werden mit numerischen Simulationen verglichen, welche gemeinsam mit Kollegen der König-Abdullah-Universität für Wissenschaft und Technologie in Saudi-Arabien durchgeführt werden. Die Ergebnisse zeigen eine gute Übereinstimmung zwischen den experimentellen Daten und den durchgeführten numerischen Simulationen, sowohl für Selbstentzündung als auch für Auslöschung.

Bei dem untersuchten alternativen Kraftstoff handelt es sich um Dimethyl Ether. Dabei wird das Auslöschverhalten von Dimethyl-Ether Flammen bei verschiedenen Brenngas- und Oxidatorstromzusammensetzungen im Gegenstrombrenner bei atmosphärischen Bedingungen untersucht. Die Zusammensetzung des Brenngas- und Oxidatorstrom wird so gewählt, dass die adiabate Flammentemperatur für jeden Messpunkt gleich bleibt. Der Wert des stöchiometrischen Mischungsverhältnisses bei diesem Experiment reicht von 0,1 bis 0,8. Die *Strain Rate* bei Auslöschung der Flamme wird als Funktion des stöchiometrischen Mischungsverhältnisses gemessen. Es wird beobachtet, dass die *Strain Rate* bei Auslöschung der Flamme bei steigenden stöchiometrischen Mischungsverhältnis zuerst abnimmt und danach stark zunimmt. Die Daten



der experimentellen Untersuchung werden mit Ergebnissen einer numerischen Simulation verglichen, welche gemeinsam mit Kollegen des *Indian Institute of Technology in Madras* durchgeführt werden. Die experimentellen Daten und numerischen Berechnungen stimmen für kleine Werte des stöchiometrischen Mischungsverhältnisses weitgehend überein, jedoch zeigt sich für größere Werte des stöchiometrischen Mischungsverhältnisses eine signifikante Abweichung.

## Acknowledgment

First of all, I would like to express my sincere gratitude to my advisor at Vienna University of Technology Prof. Dr. Ernst Pucher who encouraged me to take this great opportunity and conduct research at the University of California in San Diego. Also I would also like to thank Prof. Dr. Kalyanasundaram Seshadri for inviting me to San Diego and make this once in a lifetime opportunity possible. Special thanks go to Dr. Ulrich Niemann and Dr. Ryan Gehmlich for the fruitful conversations and keeping the lab life entertaining. I would also like to express my gratitude towards the Austrian Marshall Plan Foundation for supporting me financially.

The research at UCSD is supported by the U. S. Army Research Office, Grant # W911NF-16-1-0054 (Program Manager Dr. Ralph A. Anthenien Jr).

# Table of Content

Abstract.....	iv
Kurzfassung.....	vi
Acknowledgment .....	ix
Table of Content .....	x
List of Nomenclature.....	xii
List of Figures .....	xiv
List of Tables .....	xvii
1 Introduction .....	1
1.1 History .....	1
1.2 Motivation.....	2
1.3 Diffusion Flames.....	3
1.4 Counterflow Configuration .....	5
1.4.1 Liquid Pool Configuration .....	7
2 Investigated Hydrocarbon Fuels.....	9
2.1 Jet Fuels and Surrogates .....	9
2.2 Fuels for Advanced Combustion Engines.....	13
2.3 Dimethyl Ether .....	17
2.3.1 Determining Experimental Boundary Values .....	19
3 Experimental Setup .....	23
3.1 Atmospheric Counterflow Setup.....	23
3.1.1 Atmospheric Fuel Duct.....	26
3.1.2 Atmospheric Autoignition Oxidizer Duct .....	27
3.1.3 Atmospheric Extinction Oxidizer Duct .....	28
3.1.4 Vaporizer .....	29
3.2 High Pressure Combustion Experimental Facility (HPCEF) .....	29
3.2.1 Experimental Pressure Chamber .....	35
3.2.2 High Pressure Autoignition Oxidizer Duct .....	39

## Table of Content

3.2.3	Liquid Pool Duct .....	42
3.2.4	HPCEF Control Station.....	44
3.3	Counterflow Control Software .....	45
3.4	Flow Control .....	50
3.5	Gas Supply .....	51
3.6	Measurement of Autoignition Temperature .....	52
3.6.1	Temperature Correction .....	53
3.7	Experimental Procedure.....	55
3.7.1	Atmospheric Counterflow Procedure .....	55
3.7.2	HPCEF Procedure .....	57
4	Numerical Computations.....	61
4.1	Jet Fuel Surrogates .....	61
4.2	FACE Fuels .....	64
4.3	Dimethyl Ether .....	66
5	Results and Discussion.....	67
5.1	Jet Fuels and Surrogates .....	67
5.1.1	Pure Fuels.....	67
5.1.2	Jet Fuels and Surrogates .....	70
5.2	FACE Fuels .....	75
5.3	Dimethyl Ether .....	79
6	Conclusion and Outlook .....	84
	References .....	85
	Appendix .....	94
	Appendix A .....	94
	Appendix B .....	101
	Appendix C .....	102
	Appendix D .....	103
	Curriculum Vitae .....	105

# List of Nomenclature

Symbols	Description	Units
a	Strain rate	1/s
A	Pre-exponential factor or interaction parameter	-
A	Area	m <sup>3</sup>
c	Heat capacity per unit mass	J/kg_K
D	Diameter	m
Da	Damköhler number	-
erfc-1	Inverse of the complementary error function	-
E	Activation energy	-
F	View factor	-
h	Heat transfer rate coefficient	-
JP	Jet Propellant	-
k	Reaction rate	-
l	Length	mm
L	Separation distance	mm
Le	Lewis number	-
MW	Molecular weight	kg/mol
p	Pressure	Pa
q	Heat transfer rate	W
Q	Heat release	J/mol
R	Gas constant	J/mol·K
slpm	Standard Liters per Minute	l/min
T	Temperature	K
V	Velocity	m/s
$\dot{V}$	Volume flux	m <sup>3</sup> /s
VAC	Voltage (Alternating Current)	VAC
W	Molecular Weight	g/mole
x	Spatial coordinate	mm
X	Mole fraction	-
Y	Mass fraction	-
Z	Mixture fraction	-

## Greek Symbols Description Units

$\varepsilon$	Emissivity	-
$\lambda$	Thermal conductivity	W/m_K
$\mu$	Dynamic viscosity	Pa_s
$\nu$	Kinematic viscosity	m <sup>2</sup> /s
$\xi$	Mixture fraction	-

## List of Nomenclature

$\rho$	Density	kg/m <sup>3</sup>
$\sigma$	Stefan-Boltzmann	W/m <sup>2</sup> K <sup>4</sup>
$\chi$	Scalar dissipation rate	-
$\varphi$	Equivalence ratio	-

### Subscripts Description

0	Overall
1	Fuel side
2	Oxidizer side
b	Bead
ad	Adiabatic
conv	Convective
F	Fuel
gas	gas stream
ig	Ignition
jun	Thermocouple wire junction
mix	Mixture
i; j	Species or directional indices
Ox	Oxidizer
p	At constant pressure
rad	Radiative
ref	Reference
st	Stoichiometric
surr	Surroundings
u	Unburned
q	Extinction
w	Wire

# List of Figures

Figure 1-1: The maximum temperature in the reaction zone as a function of the Damköhler number.....	4
Figure 1-2: Basic Counterflow Configuration.....	6
Figure 1-3: Liquid Pool Counterflow Configuration.....	8
Figure 2-1: FACE fuel design matrix [31].....	14
Figure 2-2: Dimethyl Ether molecule. ....	17
Figure 3-1: Schematic illustration of the atmospheric counterflow setup.....	24
Figure 3-2: Counterflow burner in autoignition (left) and extinction (right) configuration.....	25
Figure 3-3: Cross-sectional view of the atmospheric fuel duct. ....	26
Figure 3-4: Cross-sectional view of the atmospheric oxidizer autoignition duct. ....	27
Figure 3-5: Cross-sectional view of the atmospheric oxidizer extinction duct. ....	28
Figure 3-6: Schematic illustration of the HPCEF. ....	30
Figure 3-7: Remote controlled transformer to adjust the heating element voltage. ....	32
Figure 3-8: Experimental setup inside the pressure chamber.....	33
Figure 3-9: Screenshot of the live video feed of the experiments. ....	34
Figure 3-10: Stainless steel pressure chamber. ....	36
Figure 3-11: View port with the glass insert and the adapter plate.....	37
Figure 3-12: Upper part of the pressure chamber with the safety devices. ....	38
Figure 3-13: Cross-sectional view of the autoignition duct.....	39
Figure 3-14: The "autoignition top" for elevated pressures.....	41
Figure 3-15: Cross sectional view of the liquid pool duct.....	43
Figure 3-16: Close up view of the liquid pool experiment.....	44
Figure 3-17: HPCEF Control Station. ....	44
Figure 3-18: Main screen of the counterflow control software. ....	46
Figure 3-19: HPCEF mass flow controller setup.....	50
Figure 3-20: Part of the gas supply used for the HPCEF. ....	51
Figure 3-21: Thermocouple used to measure oxidizer duct temperature. ....	52

## List of Figures

Figure 3-22: DME flame in the atmospheric counterflow burner. ....	57
Figure 3-23: Detail of the liquid pool cup. ....	58
Figure 3-24: Autoignition event of Jet-A at 4 bar captured in slow motion at 1000 frames per second. ....	59
Figure 4-1: Comparison of ignition-delay time predictions to experimental data for n-heptane. ....	62
Figure 4-2: Comparison of ignition-delay time predictions to experimental data for n-decane. ....	63
Figure 4-3: Comparison of ignition-delay time predictions to experimental data for n-dodecane. ....	63
Figure 5-1: Comparison of experimental results and simulations for the three pure fuels. ....	68
Figure 5-2: $\Delta T$ and $T_s$ as a function of $T_2$ for n-heptane and n-dodecane. ....	69
Figure 5-3: Experimental results of autoignition experiments for jet fuels and surrogates. ....	71
Figure 5-4: $\Delta T$ and $T_s$ as a function of $T_2$ for the jet fuel surrogates. ....	72
Figure 5-5: Mole-fractions of $H_2O_2$ and $KET$ as a function of $T_2$ . ....	73
Figure 5-6: Experimental and computational results for the jet fuel surrogates. ....	74
Figure 5-7: Experimental results of the extinction experiments for all FACE gasoline fuels. ....	75
Figure 5-8: Experimental data vs. numerical simulations for extinction experiments. ....	76
Figure 5-9: Experimental results of the autoignition experiments for all the FACE gasoline fuels. ....	77
Figure 5-10: Experimental data vs. numerical simulations for autoignition experiments. ....	78
Figure 5-11: Experimental results for DME extinction experiments at different adiabatic flame temperatures. ....	79
Figure 5-12: Comparison of experimental results and predictions with various mechanisms. ...	80
Figure 5-13: Comparison of experimental results with predictions of the San Diego mechanism with and without low-temperature chemistry. ....	81
Figure 5-14: The scalar dissipation rate at extinction $\chi_{st,q}$ as a function of the stoichiometric mixture fraction $\xi_{st}$ . ....	82
Figure 5-15: Profiles of $T$ and mass fractions of $CH_3OCH_3$ , $O_2$ , $H_2$ , $CO$ , $CO_2$ , and $H_2O$ calculated using the San Diego mechanism as functions of $\xi_{st}$ for $\phi=0.19$ , $a_2=400$ , $T_{st}=2000K$ . ....	83



## List of Figures

Figure 5-16: Profiles of  $T$  and mass fractions of  $\text{CH}_3\text{OCH}_3$ ,  $\text{O}_2$ ,  $\text{H}_2$ ,  $\text{CO}$ ,  $\text{CO}_2$ , and  $\text{H}_2\text{O}$  calculated using the San Diego mechanism as functions of  $\xi_{st}$  for  $\xi=0.6$ ,  $a_2=400$ ,  $T_{st}=2000\text{K}$ . ... 83

# List of Tables

Table 2-1: Composition of jet fuels.....	12
Table 2-2: Target properties and actual measured values of the FACE gasoline fuels [36]. .....	15
Table 2-3: Detailed analysis of the FACE gasoline fuels. ....	15
Table 2-4: Selected parameters for the experimental investigation.....	21
Table 2-5: Additional selected parameters for the experimental investigation .....	22
Table 4-1: Surrogate blends compositions in mole percentage [36]. ....	66
Table B-1: Autoignition temperatures for n-heptane, n-decane and n-dodecane. ....	101
Table B-2: Autoignition temperatures of the jet fuels and jet fuel surrogates. ....	101
Table C-1: Strain rate at extinction $a_{2,q}$ for the FACE fuels for several fuel mass fractions $Y_{F,1}$ .102	
Table C-2: Autoginition temperatures $T_{ig}$ for the FACE fuels for several oxidizer strain rates $a_2$ . .....	102
Table D-1: Experimental data of the study on critical limits of extinction for $T_{st}=2000K$ . ....	103
Table D-2: Experimental data of the study on critical limits of extinction for several $T_{st*}$ . ....	104

# 1 Introduction

## 1.1 History

With one million years, combustion is the oldest technology used by mankind and played a pivotal role in the advancement of humanity [1]. In the early times combustion was used to make fire to provide warmth and prepare food. With metallurgic advancements it was used to produce copper, bronze and iron. For thousands of years the objective was more to control fire rather than understanding its mechanisms. It was with the start of the first industrial revolution in the second half of the 18th century that the desire arose to understand combustion. Since then, with the development of gas turbines and internal combustion engines the demand for scientific combustion research has only increased. With all the advances this development brought, it also started to cause environmental problems, like the Great Smog of London in 1952. The first and second oil crisis in 1973 and 1979 showed that fossil fuels are not an unlimited resource and that they should be used effectively. In the 1990s most countries in the world started to acknowledge the greenhouse effect and with the founding of the United Nations Framework Convention on Climate Change (UNFCCC), started to take measures to prevent dangerous anthropogenic interference with the global climate system. These circumstances created the necessity to increase the efficiency of power generating and propulsion systems to reduce the emissions of greenhouse gases and foreign dependencies. The Paris agreement is the latest effort to reduce the magnitude of the anthropogenic climate change and aims to limit the increase in global average temperature to 1.5 °C compared to pre-industrial time by the end of the 21<sup>st</sup> century [2]. As of today, approximately 90% of the worldwide energy supply is provided by combustion of either fossil or renewable fuels [3]. Therefore, it makes it worthwhile to study combustion phenomena to make next generation propulsion systems and power generation more efficient and reduce toxic emissions. This includes automobile traffic, electrical power

supply, heating, air traffic, transport, etc. The major sources for these fuels are crude oil products, natural gas, coal, biofuels and waste.

### **1.2 Motivation**

The work resulting in this dissertation is driven by the demand for new low pollution and high efficiency internal combustion engines and therefore requiring a detailed understanding of the combustion process of hydrocarbon fuels. Combustion science helps to understand and predict combustion events in order to optimize combustion processes like in power plants or internal combustion engines. This is either done analytical or numerical by developing balance equations for conservation of mass, energy, momentum and species mass fractions for all the chemical species involved in the reaction. An analytical solution of such a system is often very work intensive if even possible at all. This is why numerical solvers are often used for predictions of combustion processes. These numerical simulation tools have become powerful instruments to predict combustion events and help to design next generation clean and efficient combustion devices. Experimental studies are required to validate chemical kinetic mechanisms used for making these predictions. There are several experimental configurations to carry out experiments involving homogenous reactant mixtures to obtain knowledge of chemical kinetics, since important parameters such as flame speed and ignition delay time are governed by temperature, pressure and reactant concentrations. There are however combustion processes where molecular transport also plays a dominant role in the combustion process.

The focus of this dissertation is only a small portion of the vast field of combustion science, namely one-dimensional diffusion flames. The counterflow configuration allows for conducting experiments on the least complex form of diffusion flames. In this configuration two opposing streams of oxidizer and fuel form a stagnation plane with a stable laminar flame in the center of the flow-field. The studied hydrocarbon fuels in this work are jet fuels, automotive type gasoline fuels and dimethyl ether, which is considered a renewable fuel.

## 1.3 Diffusion Flames

In non-premixed combustion processes fuel and oxidizer are initially separated. Mixing of the two is achieved by convection and diffusion. A chemical reaction between the fuel and oxidizer can only occur when the two are mixed on a molecular level. In diffusion flames the reaction takes place where fuel and oxidizer are in stoichiometric proportions. The time scale of chemical reactions is much shorter than the one of diffusion, therefore diffusion is the rate limiting factor, hence the name diffusion flame. A simple example for such a flame is the flame of a candle where the paraffin of the candle evaporates due to radiative heat from the flame, mounts into the wick due to capillary forces and then evaporates and mixes with surrounding air. Another practical application for this type of flame is a diesel engine, where a jet of diesel fuel is injected into a compressed volume of hot air. The flame ignites at the interface where evaporated fuel and air diffuse into each other and react. Due to the spatial homogeneity, experiments on premixed fuel-air mixtures are sufficiently defined in terms of a length scale which reduces the complexity of simulating the combustion process. For non-premixed systems, due to the diffusive nature, at least one spatial dimension is involved and thus requires time and length scales.

By plotting the maximum reaction temperature of a reactive flow-field versus the system Damköhler number, the concept of combustion limits can be visualized [4, 5]. The resulting "S-curve" consists of three solution branches and is shown in Figure 1-1. The Damköhler number is a characteristic quantity for a diffusion flame and is a non-dimensional number which is defined as the ratio of the characteristic flow time scale and chemical time scale. For one value of the Damköhler number several solutions for maximum reaction zone temperatures exist. The vertical axis represents the maximum temperature in the reaction zone, the horizontal axis represents the Damköhler number of the reaction. The lower branch represents the maximum temperature of the reactants at ignition. The upper branch represents the highest temperatures of a burning flame under given conditions. Starting out on the far right side of the lower branch, the flow-field is considered frozen. Here the reaction rates are negligible and the maximum

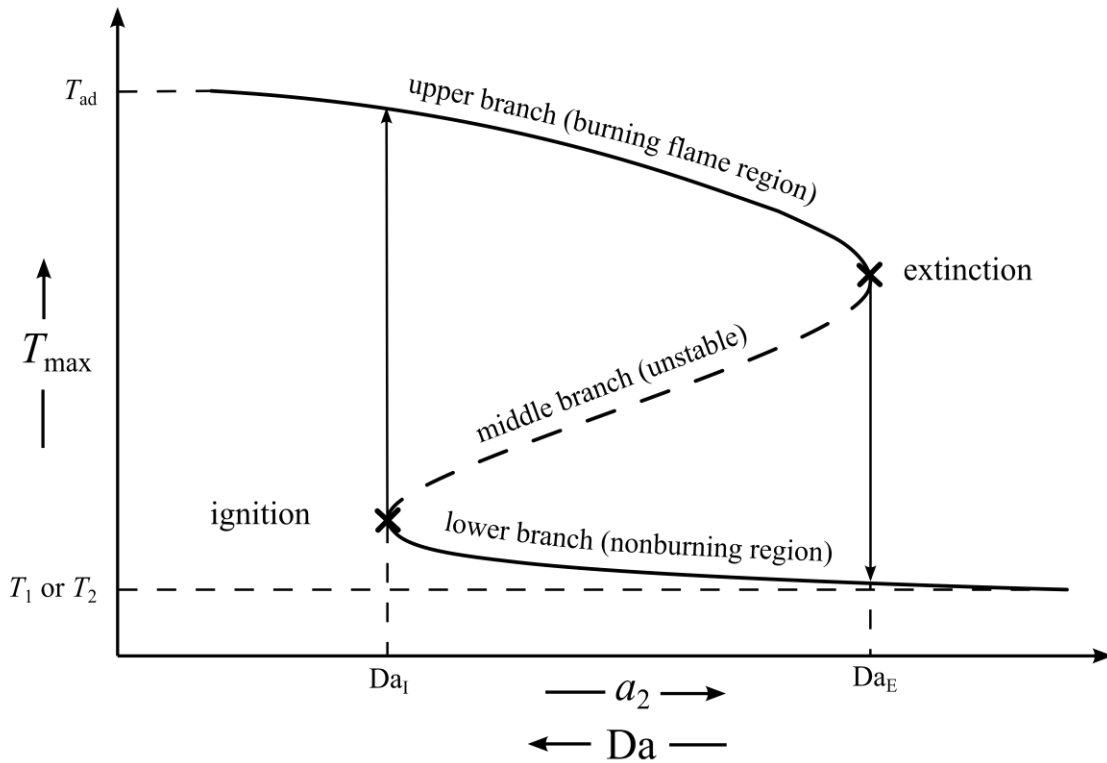


Figure 1-1: The maximum temperature in the reaction zone as a function of the Damköhler number.

temperature of the flow-field is the higher temperature of the two opposing streams. To accurately characterize the flow-field, the strain rate " $a$ " is introduced. The strain rate is defined as the normal gradient of the normal component of the flow velocity. It is the reciprocal of the characteristic flow time in the flow-field of a counterflow flame. This formulation of the strain rate was derived by Seshadri *et al.* [6]. A decrease in strain rate results in an increase of residence time of the reactants in the mixing layer and an increase in temperature results in an increase of reaction rates in the mixing layer. When the critical strain rate and temperature is reached, the mixture will ignite with the corresponding maximum temperature represented in the upper branch. Increasing the strain rate in the upper branch results in a decrease in residence time of the reactants in the reaction zone, therefore a decrease in temperature and ultimately in extinguishing the flame. The maximum temperature in the reaction zone drops back to the lower branch. The middle branch represents a physically unstable condition which cannot be realized in experiments. In the counterflow configuration the characteristic chemical

time is determined by the composition and thermodynamic state of the reactant streams while the characteristic flow time is determined by the reactant stream velocities.

### 1.4 Counterflow Configuration

Experimental investigations as carried out in this study require very specific equipment, some of which are unique. The counterflow configuration is used to elucidate the autoignition and extinction characteristics of hydrocarbon fuels at atmospheric and elevated pressures. The counterflow burner is a well-known device to conduct research on laminar diffusion flames and has been used in combustion science since the 60s of the 20th century [7]. Combustion processes in practical applications, such as jet engines, usually result in a very complex three dimensional problem which makes it difficult to make predictions on the chemistry in such a flame. The counterflow setup reduces this problem to only one spatial dimension and therefore simplifies the problem.

The counterflow burner consists of two opposing axisymmetric ducts. The upper part of the burner is referred to as the oxidizer duct. The temperature, flow velocity and oxygen mass fraction at the oxidizer duct boundary are  $T_2$ ,  $V_2$  and  $Y_{O,2}$ , respectively. The two ducts are separated by the separation distance  $L$ . The lower part of the burner is referred to as the fuel duct. The temperature, flow velocity and oxygen mass fraction at the fuel duct boundary are  $T_1$ ,  $V_1$  and  $Y_{O,1}$ , respectively. The two opposing laminar flows form the so called stagnation plane in the center of the flow-field. A stack of three fine wire Inconel mesh screens, retained by four Inconel rings, at the outlets of both fuel and oxidizer duct makes the tangential component of the flow velocity negligible and establishes plug flow conditions. The fuel duct as well as the oxidizer duct are surrounded by a so called "nitrogen curtain". These annular ducts protect the reaction zone from the surrounding atmosphere with a stream of nitrogen gas and have no influence on the combustion process. The product gases are sucked down toward the fuel side of the burner into another annular duct surrounding the curtain duct area, where they are cooled with fine mist water sprays and evacuated out of the burner. The water sprays also prevent

## 1. Introduction

unwanted flame propagation into the suction system. Boundary conditions defined for computational models must be strictly enforced during experiments. Figure 1-2 shows a schematic illustration of the basic counterflow configuration. The red line near the center represents the visible chemiluminescence of the flame shifted towards the oxidizer side of the reaction zone.

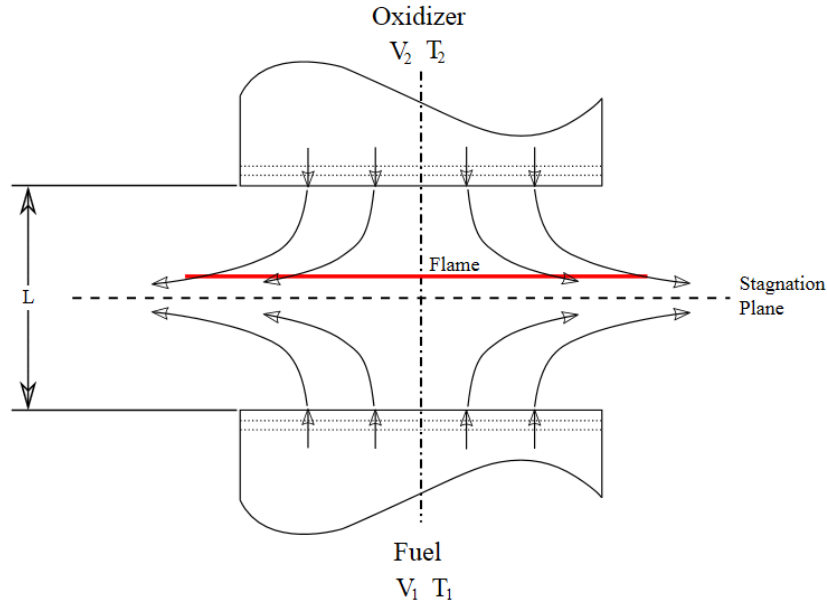


Figure 1-2: Basic Counterflow Configuration.

Index 1 represents the conditions at the fuel duct boundary of the flow-field, index 2 represents the oxidizer duct boundary conditions. The strain rate at the oxidizer duct boundary  $a_2$  is given by

$$a_2 = \frac{2|V_2|}{L} \left( 1 + \frac{|V_1|\sqrt{\rho_1}}{|V_2|\sqrt{\rho_2}} \right) \quad (1)$$

where  $L$  denotes the distance between the two duct outlets,  $\rho$  the density of the gas streams at the duct outlets and  $V$  the exit velocity of the gas streams at the fuel and oxidizer boundaries.

For conducting experiments with gaseous or pre-vaporized reactants, a momentum balance between the oxidizer stream and the fuel stream is desired, such as



## 1. Introduction

$$\rho_1 V_1^2 = \rho_2 V_2^2 \quad (2)$$

The stagnation plane of the two reactant streams and therefore the flame are forced in the center of the flow-field. This reduces heat loss of the flame to the ducts and improves the visibility of the flame. By applying a momentum balance (2), equation (1) becomes

$$a_2 = \frac{4V_2}{L} \quad (3)$$

### 1.4.1 Liquid Pool Configuration

The liquid pool counterflow configuration allows for investigation of critical conditions at autoignition or extinction of high molecular weight liquid hydrocarbon fuels. For the study carried out in this dissertation, this configuration is only used to carry out experiments on autoignition.

In this setup, an axisymmetric laminar flow of a gaseous oxidizer is directed over an evaporating pool of liquid hydrocarbon fuel. Here, subscript '2' represents conditions at the oxidizer boundary. The oxidizer mass fraction is denoted as  $Y_{O_2,2}$ . The oxidizer stream is a mixture of medical grade air and nitrogen. At the oxidizer boundary, the oxidizer injection velocity is  $V_2$ , the temperature  $T_2$  and the density  $\rho_2$ . A stack of three fine wire Inconel mesh screens at the oxidizer duct makes the tangential component of the flow velocity negligible and establishes plug flow conditions. The radial component of the flow velocity at the oxidizer boundary is presumed to be equal to zero. The distance between the oxidizer duct outlet plane and the surface of the liquid pool is denoted as  $L$ . For autoignition experiments, the distance from the oxidizer duct outlet to the surface of liquid pool is set to 12 mm. Here, subscript 's' represents conditions at the gas side of the liquid-gas interface. The temperature at the liquid-gas interface is  $T_s$ , the mass average velocity at the gas side of the liquid gas-interface is  $V_s$ . Figure 1-3 show a schematic illustration of the condensed fuel counterflow burner configuration.

## 1. Introduction

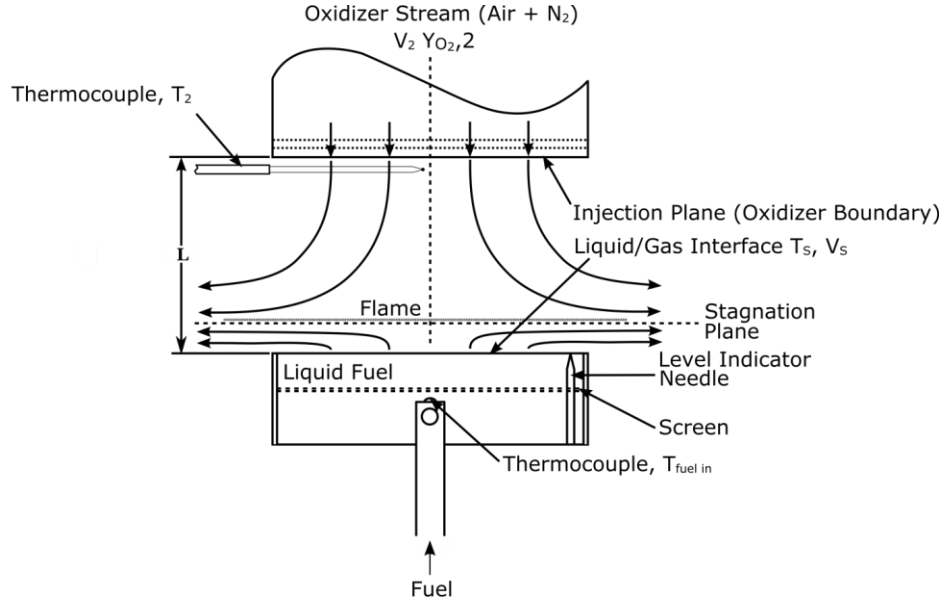


Figure 1-3: Liquid Pool Counterflow Configuration.

A previous study showed [8], that the radial component of the flow velocity at the liquid-gas interface is small and can be presumed to be equal to zero. It has been shown, that in the asymptotic limit of large Reynolds numbers, the stagnation plane formed between the oxidizer stream and the fuel vapors is close to the liquid-gas interface and a thin boundary layer is established there. The inviscid flow outside the boundary layer is rotational. In case of the liquid pool configuration,  $V_1 \approx 0$ , equation (3) becomes

$$a_2 = \frac{2V_2}{L} \quad (4)$$

## 2 Investigated Hydrocarbon Fuels

The experimental investigations carried out in this dissertation include three categories of hydrocarbon fuels, jet fuels, gasoline type fuels and an alternative fuel. The specific fuels and the motivation for their experimental investigation are explained in this chapter. Each category of fuel poses its own challenge for the experimental investigation and requires a specific experimental configuration.

### 2.1 Jet Fuels and Surrogates

Commercial and military grade aviation fuels consist of several hundred species of hydrocarbons and therefore makes it difficult to conduct numerical modeling and make predictions of combustion phenomena. A way to reduce the complexity of this problem is to formulate a jet fuel surrogate which is designed to emulate the combustion properties of the real more complex jet fuel. A surrogate reduces the amount of different hydrocarbons species drastically and therefore reduces the complexity of modeling.

This research is supported by the U.S. Army Research office (ARO) to support the efforts of the U.S. Army Single Fuel Forward policy which mandates that deployed military vehicles must refuel with the aviation fuel JP-8. The experiments carried out seek to provide fundamental knowledge about dominant aspects of reacting flows encountered in gas turbines and compression ignition engines. Since in both, jet turbines and Diesel engines, a liquid fuel is injected into a pressurized volume of air and burned in a turbulent diffusion flame, special attention is given to combustion research at elevated pressures. Funding by the U.S. Army was allocated under the objective to extend the capabilities of the High Pressure Experimental Combustion Facility to carry out experiments on critical conditions of autoignition of condensed hydrocarbon fuels up to 25 bar. The work carried out in this study focuses on the fundamental mechanisms of

## 2. Investigated Hydrocarbon Fuels

autoignition of high molecular weight liquid hydrocarbon fuels in a non-premixed flow at elevated pressures. The obtained experimental data is compared to computational data. The experimental device employed for this experiment is an updated version of the counterflow burner in the High Pressure Combustion Experimental Facility (HPCEF) at the University of California San Diego. Results of the investigations described in this chapter have been published or submitted for publication, in G. Mairinger, A. Frassoldati, R. Gehmlich, U. Niemann, A. Stagni, E. Ranzi, K. Seshadri, Autoignition of condensed hydrocarbon fuels in non-premixed flows at elevated pressures, *Combustion Theory and Modelling*, Vol. 20, No. 6, pages 995-1009, 2016 and G. Mairinger, A. Frassoldati, A. Cuoci, M. Pelucchi, E. Pucher, K. Seshadri, Experimental and Computational Investigation of Autoignition of Jet Fuels and Surrogates in Nonpremixed Flows at Elevated Pressures, *Proceedings of the Combustion Institute*. The thesis author is primary investigator in these publications.

Several experimental, computational and analytical studies have focused on combustion of high molecular weight hydrocarbon fuels, methane, ethane, ethene and hydrogen at elevated pressure [7-18]. These studies address measurements and predictions of the combustion mechanisms in rapid compression machines, flow reactors and shock tubes [9-14], extinction experiments of a non-premixed laminar flame in a counterflow setup [15-18], autoignition of non-premixed flows [19] and laminar premixed flames [20]. In contrast to several studies of autoignition of high molecular weight hydrocarbon fuels in homogenous systems [9-14], there are very few studies of these fuels in non-uniform flows at elevated pressures. However, there are several studies of autoignition of these fuels at atmospheric pressure in non-uniform flows [21-25]. A previous study measured critical conditions of extinction and autoignition for several condensed hydrocarbon fuels in non-premixed flows at atmospheric pressure [25]. The fuels tested were n-heptane, n-decane, n-dodecane, n-hexadecane, and iso-octane. It was observed, that at low strain rates the order of autoignition is as follows: n-hexadecane has the lowest autoignition temperature of the four, followed by n-dodecane, n-decane and n-heptane. In order to interpret the results, activation-energy asymptotic theory was employed [8]. A semi-detailed chemical kinetic mechanism was used in a following study to predict critical conditions

## 2. Investigated Hydrocarbon Fuels

of autoignition for these fuels [24]. The experimental data and the numerical computations agree. It was observed, that the reactivity of these fuels are resulting from a competition between the rates of low-temperature chemistry, the rates of high temperature chemistry and the rates of molecular transport. It has been shown, that for low strain rates autoignition is promoted by low-temperature chemistry and the influence of molecular transport is not pronounced [24]. A previous study has addressed autoignition characteristics of jet fuels and jet fuel surrogates at atmospheric pressures in a counterflow configuration [22]. In this study, the Aachen Surrogate and the Surrogate C replicated the autoignition behavior of JP-8 the best. Studies on autoignition characteristics of jet fuels and jet fuel surrogates at elevated pressures have been carried out employing rapid compression machines measuring ignition delay times [26, 27]. Kumar *et al.* [26] observed a shorter ignition delay time for Jet-A compared to JP-8. Two-stage ignition and Negative Temperature Coefficient (NTC) behavior has been observed for both fuels tested. Oxygen concentration was found to play an important role on the overall ignition delay. Valco *et al.* [27] observed nearly identical ignition delay times for JP-8, JP-5 and Jet-A. NTC-behavior and signs for low-temperature chemistry were observed.

The investigated fuels consist of nine different hydrocarbon fuels, three jet fuels, three jet fuel surrogates and three n-paraffin hydrocarbons.

The first group are the jet fuels. The jet fuels tested here are JP-8 (POSF 10264), JP-5 (POSF 10289) and Jet A (POSF 10325). JP stands for Jet Propellant. The POSF number is an identification number for fuels assigned by the United States Air Force. Jet A is the standard fuel for commercial aviation. JP-8 is a fuel based on commercial Jet A containing a military fuel additive package to suite the demands for applications of the United States military. JP-5 is a jet fuel with a higher flash point ( $\geq 60^{\circ}\text{C}$ ) than JP-8 ( $\geq 38^{\circ}\text{C}$ ) and is used by the United States Navy aboard aircraft carriers, where the risk of fire is particularly great [29]. The jet fuels were obtained from Edwards Air Force Base. Table 2-1 lists the composition of hydrocarbon classes found in the jet fuels in weight percentages [29]. Kerosene-type based jet fuels have a carbon number distribution between about 8 and 16 carbon atoms per molecule [30].

## 2. Investigated Hydrocarbon Fuels

	Jet-A (POSF 10325)	JP-8 (POSF 10264)	JP-5 (POSF 10289)
Alkylbenzenes	12,90 %	10,80 %	10,30 %
Alkyl naphthalenes	2,33 %	1,06 %	1,34 %
Cycloaromatics	3,43 %	1,49 %	8,88 %
n-Paraffins	20,00 %	26,80 %	13,90 %
Isoparaffins	29,40 %	39,60 %	18,10 %
Cycloparaffins	31,90 %	20,20 %	47,40 %

Table 2-1: Composition of jet fuels.

The second group is referred to as the jet fuel surrogates. These fuels, containing only a few different hydrocarbon species, are designed to emulate certain aspects of the combustion properties of the much more complex real jet fuels. Modern hydrocarbon fuels for internal combustion engines and gas turbines contain several hundred different hydrocarbon species. This high amount of different hydrocarbon molecules makes it difficult to make predictions using numerical modeling. A way to reduce the complexity of this problem is formulating surrogate fuels, containing only a handful different hydrocarbon molecules and thereby reducing the complexity of numerical modeling. The jet fuel surrogates tested are the Aachen Surrogate, the Surrogate C and the 2nd generation Princeton Surrogate (POSF 4658). The Aachen Surrogate contains 80% n-decane ( $C_{10}H_{22}$ ) and 20% 1,3,5 trimethylbenzene ( $C_9H_{12}$ ) by weight. In a study by Humer et. al. [22], several batches of JP-8 and Jet-A together with 15 different possible jet fuel surrogates were tested in a counterflow configuration at atmospheric pressure. In this study and several other studies [18], the Aachen Surrogate and the Surrogate C were found to reproduce the key aspects of non-premixed combustion of JP-8. The Surrogate C is a mixture of 60% n-dodecane ( $C_{12}H_{26}$ ), 20% methylcyclohexane ( $C_7H_{14}$ ) and 20% o-xylene ( $C_8H_{10}$ ) by volume. The Aachen Surrogate was found to reproduce the characteristics of critical conditions at autoignition the best but not at extinction. The 2nd generation Princeton Surrogate by Dooley et. al. [7], is a mixture of 49.6% n-dodecane ( $C_{12}H_{26}$ ), 24.3% iso-octane ( $C_8H_{18}$ ), 19.8% n-propylbenzene ( $C_9H_{12}$ ) and 6.3% 1,3,5 trimethylbenzene ( $C_9H_{12}$ ) by mass and was not available for the studies mentioned above.

## 2. Investigated Hydrocarbon Fuels

The third group is referred to as the pure fuels and consist of n-heptane, n-decane and n-dodecane. These three n-paraffin hydrocarbons are chosen because they are important constituents of jet fuel surrogates.

This study extends previous work carried out to elevated pressures to study the influence of low-temperature and high temperature chemistry on autoignition. An experimental and kinetic modelling study is carried out on the mechanisms of autoignition of n-heptane, n-decane, n-dodecane, Jet-A, JP-8, JP-5, Aachen surrogate, surrogate C and the Princeton surrogate at elevated pressures. Critical conditions of autoignition are measured and compared with predictions obtained using skeletal chemical kinetic mechanisms.

### 2.2 Fuels for Advanced Combustion Engines

The Fuels for Advanced Combustion Engines (FACE) is a set of ten standardized gasoline type test fuels. The motivation for designing standardized test fuels is to allow researches, conducting research on new advanced combustion engines, to compare their results to results from different research facilities using the same set of fuels. These FACE gasoline test fuels were formulated by the U.S. Department of Energy and the Coordinating Research Council's (CRC) FACE working group. The CRC is a non-profit organization coordinating environmental and engineering studies between the automotive and petroleum industry. The sustaining members of the CRC are the American Petroleum Institute and several automobile manufacturers. The FACE working group is a collaboration between the CRC member companies and the United States Department of Energy National Laboratories.

The FACE gasoline fuels are designed around four target properties of significant importance for the performance of modern advanced combustion engines: The research octane number (RON), octane sensitivity ( $S = \text{RON} - \text{MON}$ ), aromatics content, and normal paraffin (n-paraffin) content. The target properties for the fuels are: RONs of 75, 85 and 95, octane sensitivity of  $\leq 2$  and  $\sim 10$ , aromatics content 5 and 35 Vol% and n-paraffin contents of 5 and 25 Vol% [31]. The

## 2. Investigated Hydrocarbon Fuels

RON and S parameters are a measure for the fuels autoignition quality. Some of these target properties are conflicting and require trade-offs which result, that in some cases target properties are not completely met. RON target values like 70 and 85 and octane sensitivity  $S \leq 2$  are lower and n-paraffin content of 25 Vol% are higher than current commercial available gasolines but they are potentially relevant for emerging advanced low-temperature combustion engines and were therefore included in the design matrix. Figure 2-1 shows the FACE fuel design matrix.

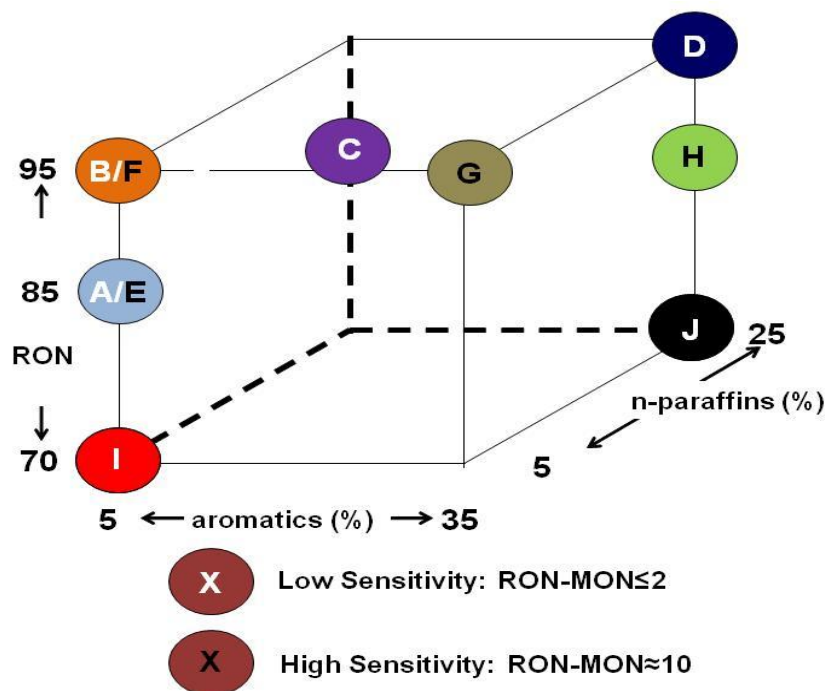


Figure 2-1: FACE fuel design matrix [31].

A commercial vendor (Chevron Phillips Chemical) produced the ten test fuels according to the specified target properties and made them available to the research community to enable consistent comparisons of experimental results from different research facilities and test platforms based on the same set of test fuels.

As already mentioned before, refined gasoline is a complex hydrocarbon mixture which makes predictions on characteristics of combustion difficult. The approach to simplify this task is to develop gasoline surrogates. This is done by grouping the fuels molecules together and formulate a surrogate to match the original fuels properties. The goal is to develop predictive chemical kinetic models for gasoline fuel surrogates. Table 2-2 lists the target design properties for



## 2. Investigated Hydrocarbon Fuels

the FACE fuels and measured values of the actual final fuels. Table 2-3 lists a detailed analysis of the FACE gasoline fuels.

	FACE A	FACE C	FACE F	FACE I	FACE J	FACE G
<b>Target RON</b>	85	85	95	70	70	95
<b>Target Sensitivity</b>	≤2	≤2	10	≤2	≤2	10
<b>Target n-Paraffins Vol%</b>	5%	25%	5%	5%	25%	5%
<b>Target Aromatics Vol%</b>	5%	5%	5%	5%	35%	35%
<b>RON</b>	83,5	84,7	94,4	70,3	71,8	96,8
<b>MON</b>	83,6	83,6	88,8	79,5	68,8	85,8
<b>Sensitivity</b>	0,1	1,1	5,6	0,7	3	0,7

Table 2-2: Target properties and actual measured values of the FACE gasoline fuels [36].

	FACE A	FACE C	FACE F	FACE I	FACE J	FACE G
<b>isoparaffins mol%</b>	83,15	65,60	61,07	73,44	31,24	35,41
<b>n-paraffins mol%</b>	13,75	30,24	4,98	14,06	32,39	7,96
<b>cycloparaffins mol%</b>	2,09	0,14	15,38	3,72	2,50	14,96
<b>aromatics mol%</b>	0,82	3,98	8,86	1,54	33,23	33,06
<b>olefins mol%</b>	0,19	0,03	9,72	7,24	0,64	8,61
<b>H/C ratio</b>	2,29	2,27	2,13	2,25	1,97	1,83
<b>avg mol. Wt</b>	97,84	97,19	94,78	96,33	100,28	99,69

Table 2-3: Detailed analysis of the FACE gasoline fuels.

New forms of automotive propulsion systems like hydrogen or battery electric vehicles are considered to increase their respective market shares within the upcoming decades but the internal combustion engine will still likely remain the major source of power for automobiles. For once, hybrid powertrains, which is a combination of an internal combustion engine and an electric motor, is getting increasingly more popular due to the more and more restrictive emissions regulations. Electric vehicles will most likely still remain a minority on a global scale due to the high costs and missing infrastructure in most parts of the world. Another factor are emerging markets like India where more and more people seek mobility and demand cost effective propulsion systems. In any scenario, the internal combustion engine will remain a crucial part of

## 2. Investigated Hydrocarbon Fuels

the portfolio for automotive propulsion systems and with the latest efforts to reduce emissions and increase efficiency, the market demands new advanced combustion engines and therefore the knowledge of combustion characteristics of hydrocarbon fuels becomes more important. Examples for advanced combustion systems are reactivity controlled compression ignition (RCCI), premixed charged compression ignition (PCCI), homogenous charge compression ignition (HCCI), controlled auto-ignition (CAI), high efficiency clean combustion (HECC) and advanced stoichiometric high efficiency engine combustion engines. In these engine concepts, ignition is primarily controlled by chemical kinetics which makes it desirable to develop tools to predict the ignition behavior of gasoline fuels [32]. Gasoline is the most widely used fuel for light duty vehicles in the world. Refined gasoline fuels consist of hundreds of different hydrocarbons which also vary with geographic location [33]. It consists of hydrocarbons in the  $C_4 - C_{10}$  range, including linear and branched paraffins, naphthalenes, olefins and aromatics [34]. This makes modeling of their combustion behavior difficult. In order to reduce the complexity of this problem surrogate fuels are formulated.

There have been several experimental and computational studies on the combustion characteristics of the FACE gasoline fuels [32, 35-37]. Sarathy et al. conducted experiments employing shock tubes and rapid compression machines comparing ignition delay times of PRF 84 (PRF = Primary Reference Fuel) and the two FACE gasoline fuels FACE A and FACE C [32]. The study showed that multi-component surrogate blends could replicate the experimental ignition delay times of FACE A and FACE C better than PRF 84. Jaye *et al.* measured Ignition delay times for FACE A and FACE C by employing a laser-based method and suggested the octane number as a target property for surrogate formulation [35]. Several target properties for the development of surrogate fuels have been proposed. Ranzi et al. suggested viscosity, octane number, thermal stability among other physical and chemical properties as target properties for the development of gasoline surrogates [38]. Others recommended H/C ratio, research octane number (RON), distillation curve and density as the target properties a surrogate should have to replicate combustion behavior of a gasoline fuel [39]. In practical combustion systems ignition takes place in the presence of concentration and temperature gradients. In non-premixed systems,

autoignition temperatures of multi-component surrogates are sensitive to diffusion and kinetics [40]. In homogenous systems transport occurs so fast that it does not contribute much to ignition. However, experimental studies on combustion characteristics of FACE gasoline fuels under non-premixed combustion remain scarce. There have been experimental studies on gasoline fuels in a counterflow configuration [41] but not including the FACE gasoline fuels.

Due to the lack of experimental data on the ignition and extinction limits of the FACE gasoline fuels, an experimental study employing the counterflow configuration is carried out. In this study, critical conditions of autoignition and extinction are measured for several strain rates and reactant mass fractions. The obtained experimental data is then compared to numerical computations carried out in collaboration with the Combustion and Pyrolysis Group from the King Abdullah University of Science and Technology in Saudi Arabia. For the conducted numerical computations, the FACE gasoline surrogate blends modeled by Sarathy et al. are utilized.

### 2.3 Dimethyl Ether

With the rising efforts to reduce global CO<sub>2</sub> emissions and especially local particulate emissions in urban areas, dimethyl ether (DME) is becoming increasingly more interesting as an alternative fuel for vehicles with compression ignition engines. Particularly the possibility to produce DME from multiple sources, including biomass, makes it an attractive alternative fuel considering the latest efforts to reduce the impact of manmade climate change. Dimethyl ether (DME) is the simplest ether with a chemical formula of CH<sub>3</sub>OCH<sub>3</sub>. Figure 2-2 shows the molecule structure of dimethyl ether.

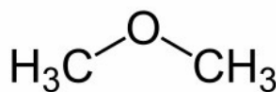


Figure 2-2: Dimethyl Ether molecule.

## 2. Investigated Hydrocarbon Fuels

DME has various properties that make it attractive for the use in compression ignition engines. It has a high cetan number of 55 which leads to a short ignition delay time and lower engine noise. Diesel engines can be operated with dimethyl ether requiring only moderate modifications to the injection system. DME burns with a visible blue flame and since there are no carbon to carbon bonds, it burns with no formation of particulate matter and very low formation of NO<sub>x</sub> and CO which could reduce the cost of exhaust gas aftertreatment systems for diesel engines. It also is not carcinogenic, mutagenic or toxic to the human body. With a heating value of 28,4 MJ/kg, DME has half the energy density of diesel. At room temperature and atmospheric pressure DME is gaseous and becomes liquid above 6.1 atm. This leads to bigger and more expensive fuel storage solutions in vehicles than conventional diesel fuel tanks. DME can also be blended with liquefied petroleum gas (LPG) and used to power vehicles with Otto engines [42].

Numerous experimental and computational studies have addressed combustion characteristics of dimethyl ether carrying out experiments in shock tubes, rapid compression machines and other devices [43, 44]. There have also been several studies addressing the performance of DME in internal combustion engines with promising results [45-53]. A detailed chemical kinetic model was developed by Curran *et al.* based on data in a jet-stirred reactor and ignition delay times [48]. However, there have been very few experimental studies addressing critical limits of extinction of DME in non-premixed flames. Wang *et al.* [54] carried out an experimental and computational study on dimethyl ether in a counterflow configuration under atmospheric conditions investigating critical conditions at extinction. In this study the oxidizer was a stream of pure air and the fuel stream was a stream of DME diluted with nitrogen preheated to 333 K. The study aimed to elucidate the influence of the fuel/N<sub>2</sub> ratio on the extinction behavior of non-premixed DME flames. The carried out numerical computations predicted higher strain rates at extinction than the obtained experimental data.

An experimental study is carried out to elucidate the extinction characteristics of dimethyl ether employing the atmospheric counterflow configuration. A similar experiment has already been conducted together with Mairhofer *et al.* [55] for only one chosen adiabatic flame tem-

perature. In this study, these experiments are carried out with additional measures to increase accuracy and multiple adiabatic flame temperatures. The reaction rate of a chemical reaction is strongly dependent on the temperature, therefore it is useful to make a comparison of extinction experiments of different reactant mixtures for the same adiabatic flame temperature  $T_{st}$ . For this experiment the adiabatic flame temperature  $T_{st}$  is kept constant at 2000K. The Lewis number is  $Le_{dme} = 1,5$ . The experiment is carried out for different oxidizer and fuel stream mixture fractions. Additional measurements are taken for adiabatic flame temperatures of  $T_{st} = 1950K, 1975K, 2025K, 2050K$  to study the influence of adiabatic flame temperature on the extinction behavior. The obtained experimental data is compared to numerical simulations carried out in collaboration with colleagues from the Indian Institute of Technology Madras. Results of the investigations described in this chapter have been submitted for publication in G. Mairinger, R. Khare, K. Narayanaswamy, M. Hunyadi-Gall, V. Raghavan, K. Seshadri, Experimental and Computational Investigation of the Influence of Stoichiometric Mixture Fraction on Structure and Extinction of Laminar, Non-premixed Methoxymethane Flames, *Proceedings of the Combustion Institute*. The thesis author is primary investigator in this publication.

### 2.3.1 Determining Experimental Boundary Values

The boundary values employed in this experiment are calculated by an asymptotic model developed by Prof. Seshadri. The equations used in this chapter are a result of this model which is attached in Appendix A.

The initial temperature of the reactants  $T_1$  and  $T_2$  is presumed to be room temperature which is kept constant at 295 K. The heat release rate  $Q_{DME}$  and heat capacity  $c_{p,st}$  of DME is  $Q_{DME} = 132,8$  kJ/mol and  $c_{p,st} = 1300$  J/kgK. The experiments are carried out for an adiabatic flame temperature  $T_{st} = 2000$  K and a Lewis number  $Le_{DME} = 1.5$ . Additionally, single data points are taken for  $T_{st} = 1950$  K, 1975 K, 2025 K and 2050 K. The mass fraction of DME in the fuel stream is referred to as  $Y_{DME,1}$  and the mass fraction of oxygen in the oxidizer stream is referred to as  $Y_{O_2,2}$  respectively. Described below is the calculation of the fuel and oxidizer mass fractions for  $T_{st} = 2000$  K.

## 2. Investigated Hydrocarbon Fuels

For the case of pure oxygen in the oxidizer stream  $Y_{O_2,2} = 1$ , the stoichiometric mixture fraction  $\xi_{st}$  is calculated as follows,

$$\xi_{st} = 1 - \frac{3c_p(T_{st} - T_u)W_{O_2}}{Q_{dme}} \quad (5)$$

For the case of pure DME in the fuel stream  $Y_{dme,1} = 1$ , the stoichiometric mixture fraction  $\xi_{st}$  is calculated by the solution of the following equation,

$$\frac{\xi_{st}(1 - \xi_{st})}{1 - \xi_{dme,st}} = \frac{c_p W_{C_2H_6O} \sqrt{Le_{dme}} (T_{st} - T_u)}{Q_{dme}} \left\{ \exp \left[ \frac{x_{st}^2 (Le_{dme} - 1)}{2} \right] \right\} \quad (6)$$

Fuel and oxidizer mass fractions for each stoichiometric mixture fraction have to be calculated individually. With

$$\xi_{dme,st} = \frac{1}{2} \operatorname{erfc} \left( x_{st} \sqrt{\frac{1}{2}} \right) \quad (7)$$

It follows

$$x_{st} = \sqrt{2} [\operatorname{erfc}^{-1}(2\xi_{st})] \quad (8)$$

$\operatorname{Erfc}^{-1}$  is the inverse of the complementary error function. The stoichiometric mixture fraction can then be calculated with

$$\xi_{dme,st} = \frac{1}{2} \operatorname{erfc} \left( x_{st} \sqrt{\frac{Le_{dme}}{2}} \right) \quad (9)$$

The fuel and oxidizer mass fractions can be calculated by introducing

$$m = \frac{c_p(T_{st} - T_u)}{Q_{dme}\xi_{st}(1 - \xi_{st})} \quad (10)$$

## 2. Investigated Hydrocarbon Fuels

This leads to

$$Y_{O_2,2} = 3m\xi_{st}W_{O_2} \quad (11)$$

$$Y_{dme,1} = mW_{C_2H_6O}\sqrt{Le_{dme}}(1 - \xi_{dme,st}) \left\{ \exp \left[ \frac{x_{st}^2(Le_{dme} - 1)}{2} \right] \right\} \quad (12)$$

Table 2-4 lists the calculated DME ( $Y_{DME,1,2000}$ ) and oxygen ( $Y_{O_2,2,2000}$ ) mass fractions for an adiabatic flame temperature of 2000 K for several stoichiometric mixture fractions  $\xi_{st,2000}$ .

$\xi_{st,2000}$	$Y_{DME,1,2000}$	$Y_{O_2,2,2000}$
0,13432	1	0,1848
0,16	0,7945	0,1904
0,19	0,6351	0,1975
0,22	0,5256	0,2051
0,3136	0,3349	0,2330
0,4	0,2471	0,2666
0,5	0,1877	0,3199
0,6	0,1503	0,3999
0,7	0,1247	0,5332
0,8	0,1060	0,7997
0,82	0,1028	0,8886
0,84005	0,0998	1

Table 2-4: Selected parameters for the experimental investigation.

Additionally, experiments are conducted to study the influence of the adiabatic flame temperature on the extinction strain rate. The additional selected adiabatic flame temperatures and stoichiometric mixture fractions are listed in Table 2-5.

## 2. Investigated Hydrocarbon Fuels

$\xi_{st}$	$Y_{DME,1, 2050}$	$Y_{O_2,2} \text{ 2050}$	$Y_{DME,1} \text{ 2025}$	$Y_{O_2,2} \text{ 2025}$
0,22000	0,5411	0,2111	0,5334	0,2081
0,4	0,2544	0,2744	0,2508	0,2705
0,6	0,1547	0,4116	0,1525	0,4057
$\xi_{st}$	$Y_{DME,1} \text{ 1975}$	$Y_{O_2,2} \text{ 1975}$	$Y_{DME,1} \text{ 1950}$	$Y_{O_2,2} \text{ 1950}$
0,22000	0,5179	0,2020	0,5102	0,1990
0,4	0,2435	0,2627	0,2399	0,2587
0,6	0,1481	0,3940	0,1459	0,3881

Table 2-5: Additional selected parameters for the experimental investigation.



## 3 Experimental Setup

Two types of counterflow configurations have been employed for the experimental investigations described in this dissertation, the atmospheric counterflow configuration and the High Pressure Combustion Experimental Facility. In this chapter, a description of the capabilities of the facilities is given with an emphasis on elements of the facility which have been modified or improved for the experimental studies carried out in this dissertation.

### 3.1 Atmospheric Counterflow Setup

The atmospheric counterflow burner at UC San Diego has been employed for numerous experimental studies in the past [21, 41, 56-64]. For the experimental investigations carried out in this dissertation, the counterflow burner is employed in the autoignition and extinction configuration.

Figure 3-1 shows a schematic illustration of the experimental setup including the counterflow burner in the extinction configuration, gas supply, mass flow controllers, liquid fuel supply pump, vaporizer, data acquisition and control system. The counterflow burner can be either equipped with the autoignition or the extinction oxidizer duct. In case of experiments involving a gaseous fuel, the vaporizer and liquid fuel supply pump can be bypassed.

The atmospheric counterflow setup is equipped with several mass flow controllers with varying flow ranges from 5 to 100 standard liters per minute. The mass flow controllers provide their maximum accuracy if they are operated between the range of 10 to 90 % of their maximum flow range. The flow controller setup for every data point is specifically chosen to provide maximum accuracy. For calibrating the mass flow controllers a Ritter TG5ER gas meter is used. The liquid fuel is supplied by a high precision Teledyne Isco 500D syringe pump with a volumetric flow accuracy of  $\pm 0.01$  ml/min. The experiment is automated using the LabVIEW counterflow control software. The software automatically calculates the required reactant stream flow rates

### 3. Experimental Setup

depending on the entered experimental parameters and sends signals to the mass flow controllers and syringe pump. An E-type thermocouple measures the fuel duct temperature right beneath the fuel duct Inconel screens and provides feedback to the counterflow control software. The fuel duct temperature usually is above room temperature due to heat conduction from product gases to the aluminum burner body. The oxidizer stream consists of pure air which is sourced from the UC San Diego campus pressured air system and is presumed to be room temperature which is kept constant at 22°C. Experimental pressure is presumed to be 1 atm. Nitrogen is introduced into to exhaust to prevent flame propagation into the suction system.

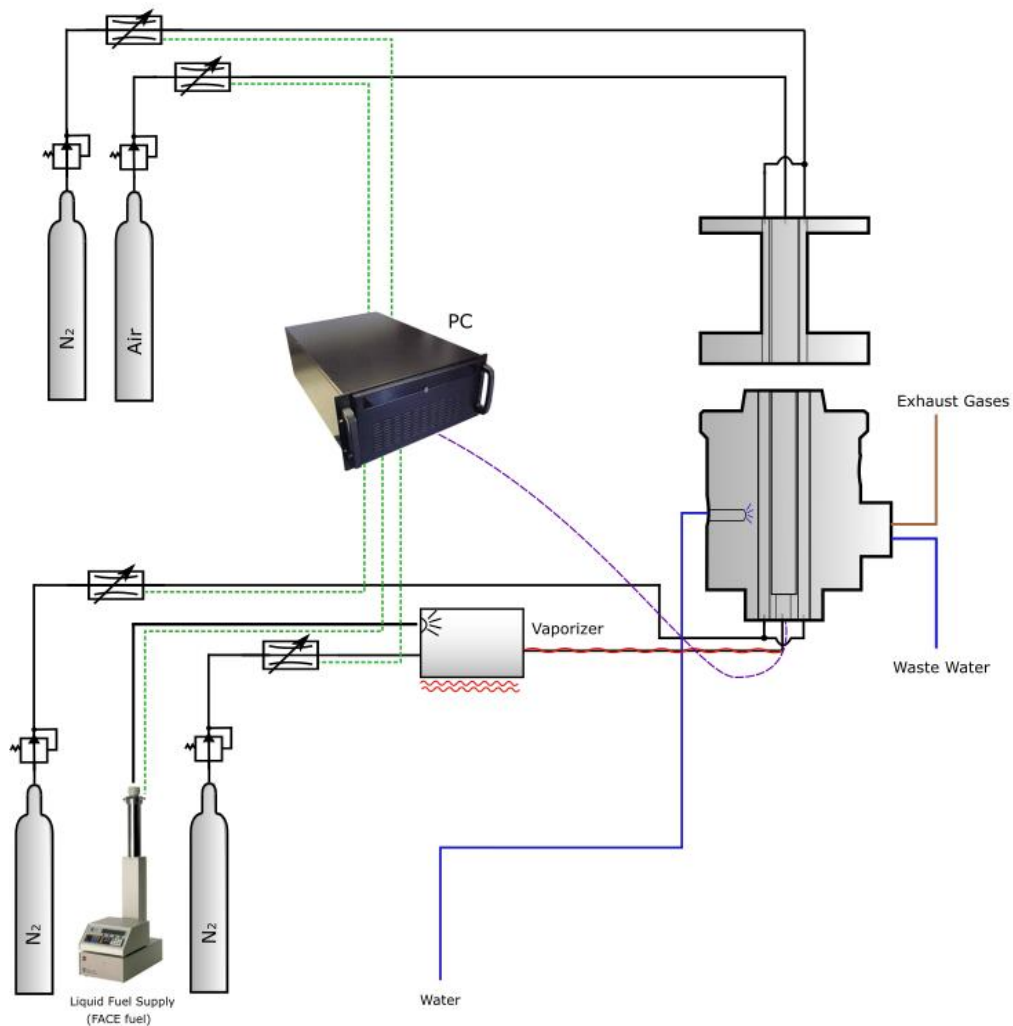


Figure 3-1: Schematic illustration of the atmospheric counterflow setup.

### 3. Experimental Setup

Figure 3-2 shows the atmospheric counterflow burner in the autoignition and extinction configuration.

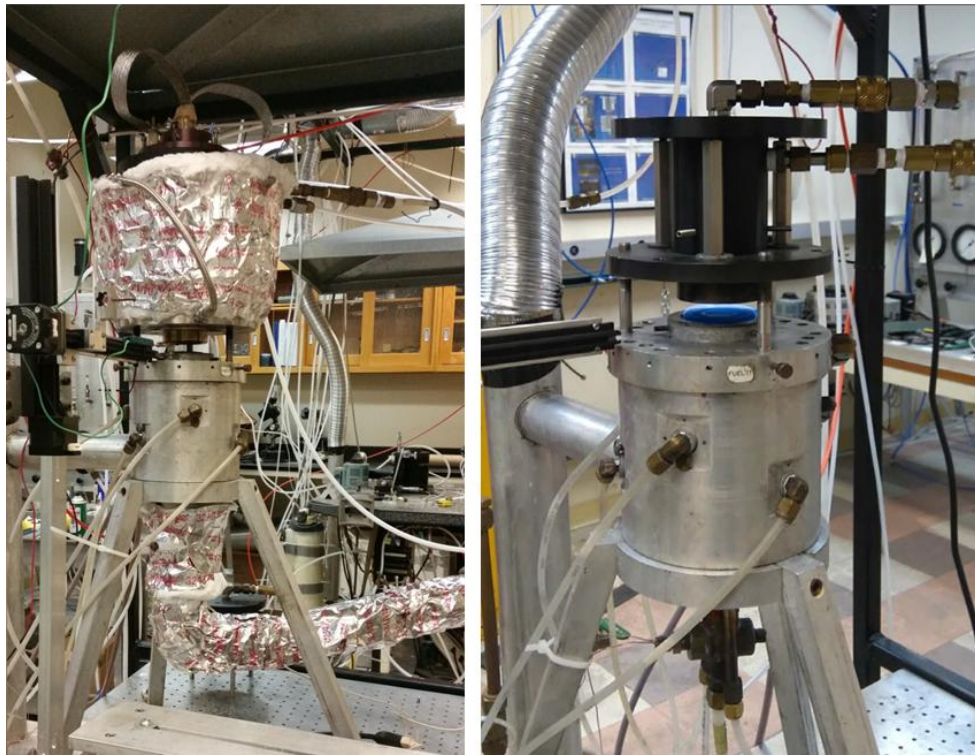


Figure 3-2: Counterflow burner in autoignition (left) and extinction (right) configuration.

The autoignition counterflow configuration is shown on the left side with the autoignition oxidizer duct on top, the fuel duct in the center and the heated fuel supply line coming from the vaporizer in the lower part of the frame. On the right side figure 3-2 shows the counterflow burner in operation with a dimethyl ether flame. The oxidizer extinction duct is the black anodized part on top. The silver grey part in the lower half of the frame is the fuel duct. The blue flame can be seen between the two ducts. The silver hose in the left part of the frame is connected to the in-house suction system and is used for evacuating the product gases. The burner is mounted on top of an optical table under a fume hood.

### 3. Experimental Setup

#### 3.1.1 Atmospheric Fuel Duct

The body of the so called “fuel duct” is made out of machined aluminum for better heat transfer. The gaseous fuel stream is directed towards the reaction zone with a stainless steel tube. At the outlet of the duct, three Inconel mesh screens create a laminar flow-field. A second concentric stainless steel tube guides the nitrogen curtain flow towards the reaction zone. Two E-type thermocouples are placed beneath the screens of the fuel duct and measure the temperature of the fuel stream right before it enters the reaction zone. One gives feedback to the LabVIEW control software to calculate the flow rates for the fuel side reactants and maintain the momentum balance. The second one gives feedback to a PID-control loop which controls the power for the fuel side reactant heaters. The product gases are cooled down using fine mist water sprays. Suction is created by the in-house central vacuum system. The water and product gases are separated and evacuated. Figure 3-3 shows a cross-sectional view of the burner bottom.

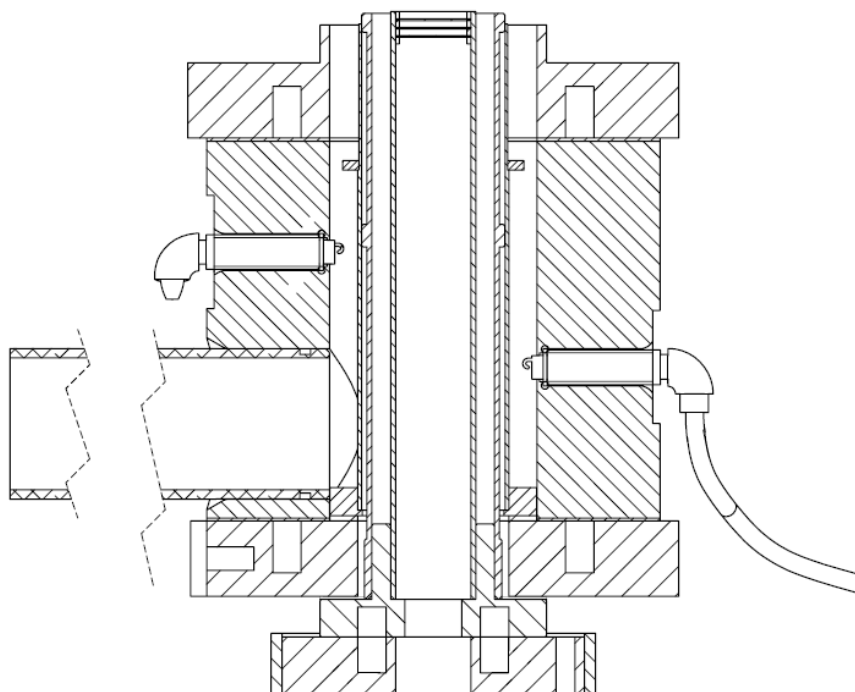


Figure 3-3: Cross-sectional view of the atmospheric fuel duct.

#### 3.1.2 Atmospheric Autoignition Oxidizer Duct

The oxidizer duct for autoignition experiments is shown in Figure 3-4.

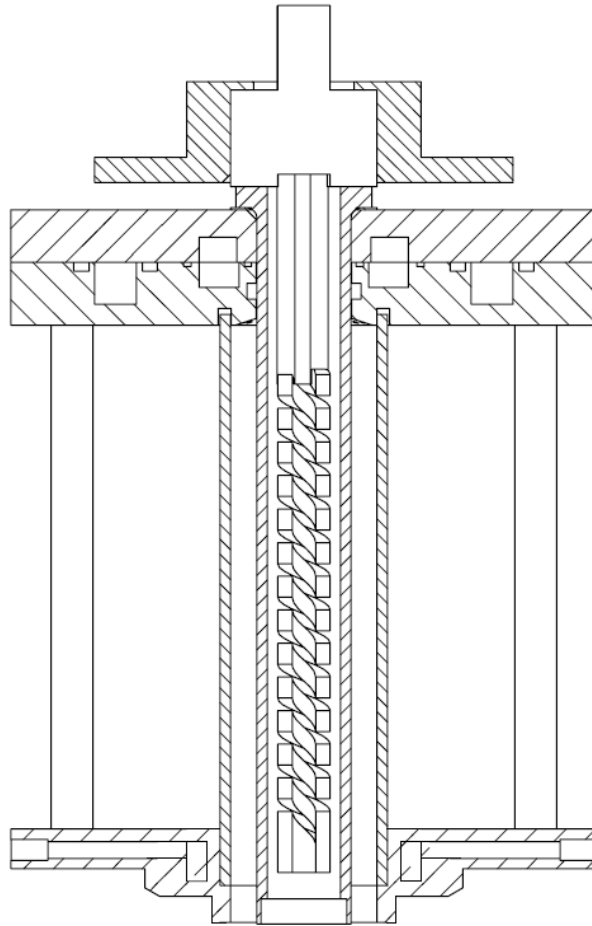


Figure 3-4: Cross-sectional view of the atmospheric oxidizer autoignition duct.

The main part of the “autoignition top” is a silicon carbide heating element with a length of 259 mm, a diameter of 19 mm and a resistive heating power of up to 2.2 kW. This heating element is capable to preheat the oxidizer up to 1400 K at the oxidizer duct outlet. The heating element is surrounded by a machined quartz tube, which guides the oxidizer towards the reaction zone. A second annular quartz tube guides the nitrogen curtain stream towards the reaction zone. Quartz is chosen for this application to deal with the high surface temperature of the heating element and to reduce thermal expansion to a minimum. Due to the high temperatures occurring inside the duct, internal water cooling is required. To reduce heat loss, the duct is wrapped

### 3. Experimental Setup

in thermal insulation. The oxidizer duct is mounted on top of the burner bottom with three adjustable set screws to precisely adjust the duct separation distance.

#### 3.1.3 Atmospheric Extinction Oxidizer Duct

The oxidizer duct for extinction experiments is shown in Figure 3-5. The duct consists of two concentric stainless steel tubes. The inner tube guides the oxidizer stream towards the reaction zone. At the outlet of the inner tube, three Inconel mesh screens are placed to establish a laminar flow-field. The screens are kept in place by four Inconel retaining rings. Between the inner and outer tube, nitrogen flows towards the reaction zone to shield it off from the surrounding atmosphere. A ceramic honeycomb close to the outlet of the nitrogen curtain establishes a uniform flow. No water cooling of the duct is necessary. Three set screws are used for mounting and adjusting the oxidizer duct on top of the fuel duct.

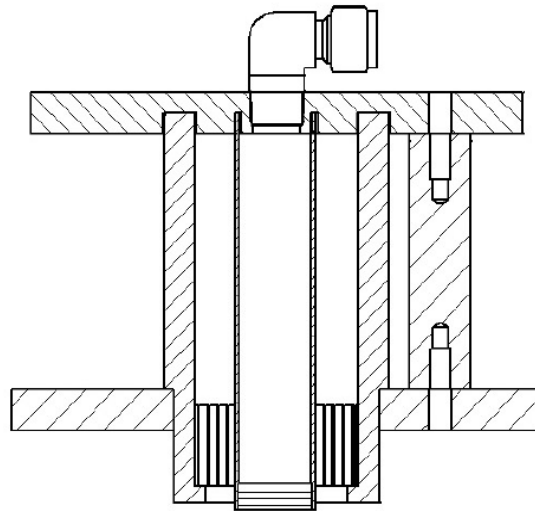


Figure 3-5: Cross-sectional view of the atmospheric oxidizer extinction duct.

### 3. Experimental Setup

#### 3.1.4 Vaporizer

The vaporizer employed for this experiment is a custom built unit and consists of a heated aluminum box into which fuel is injected through the top. The aluminum box rests on a temperature controlled heating plate and is wrapped in heating tape. The nozzle is mounted on a separate aluminum plate which is water cooled to prevent boiling of the fuel within the nozzle and tubing. A thermocouple located at the inlet of the vaporizer provides feedback to ensure proper conditions for evaporation. Another thermocouple is located at the outlet and provides feedback to a PID-control loop which controls the heating tape. The temperature of the vaporizer must be kept high enough to ensure proper evaporation of the injected fuel but low enough to prevent cracking of the fuels molecules. The flow line from the vaporizer to the bottom of the counterflow burner is heated as well to prevent condensation of the fuel. A thermocouple placed right below the fuel duct provides feedback to a PID-control loop that controls a heating tape which is wrapped around the support lines from the vaporizer to the counterflow burner. Again, precise temperature control is crucial to prevent fuel cracking or condensation. This set-up allows for a very precise control of the fuel duct temperature.

## 3.2 High Pressure Combustion Experimental Facility (HPCEF)

The High Pressure Combustion Experimental Facility is a unique experimental configuration at the University of California in San Diego, which allows for testing of combustion characteristics of gaseous and liquid fuels in a counterflow configuration up to 25 bar. Numerous experimental studies have been carried out involving this facility [65-68]. This facility was originally designed by Ulrich Niemann [16] to carry out combustion experiments in a counterflow configuration with gaseous reactants up to 25 bar. Ryan Gehmlich [69] extended the capabilities of the HPCEF to carry out combustion experiments involving liquid fuels in a counterflow configuration. Both configurations were limited to extinction experiments only. With this latest round of experi-

### 3. Experimental Setup

ments, the capabilities of the HPCF are extended to carry out autoignition experiments in a counterflow configuration for fuels with high boiling points, for which it would be difficult to avoid pyrolysis reactions in the process of vaporizing them. In this new configuration, a steady axisymmetric laminar flow of a hot oxidizer is directed towards a vaporizing surface of a liquid fuel in a pressurized nitrogen atmosphere. This chapter gives an overview over the already existing experimental apparatus and provides details for features which have been implemented for the latest experiment.

Figure 3-6 shows a schematic illustration of the overall experimental configuration.

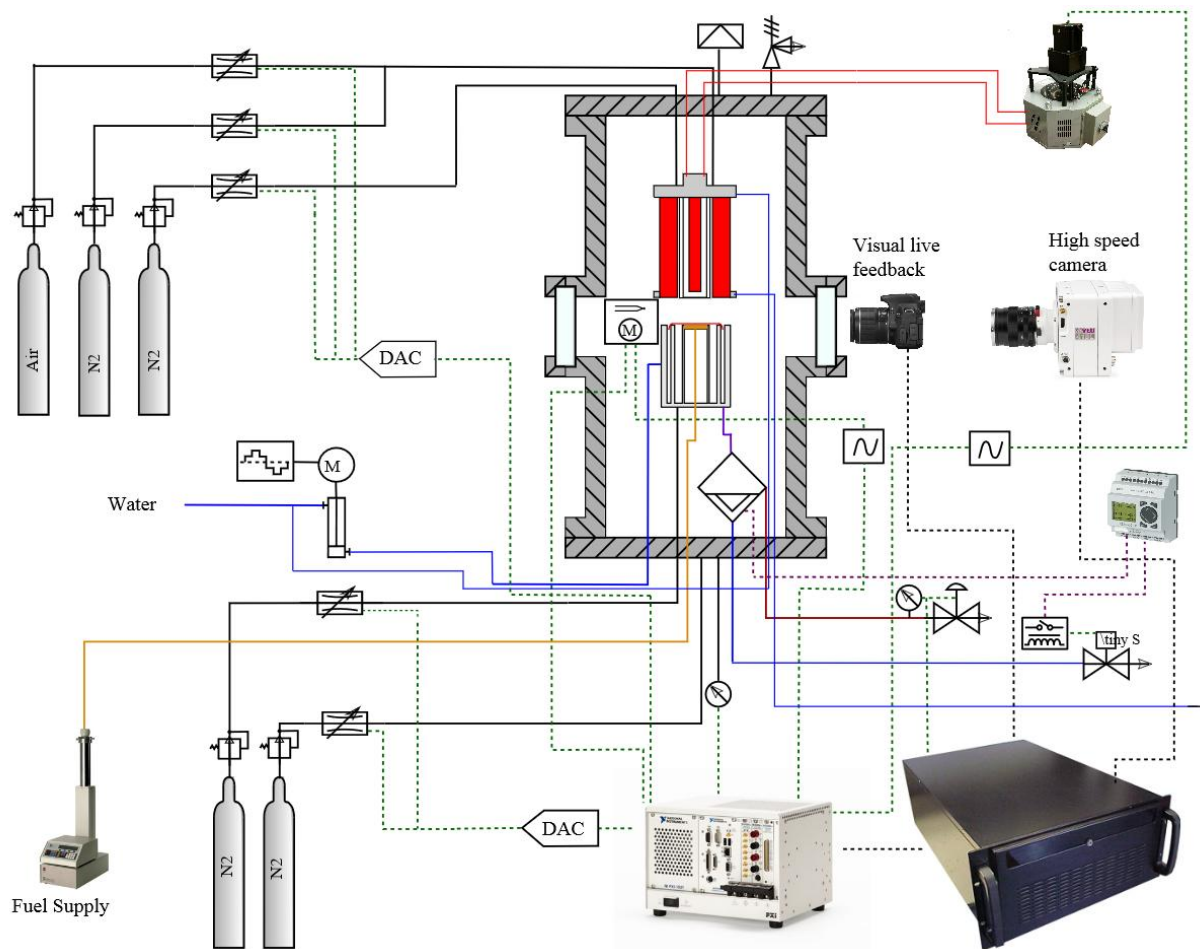


Figure 3-6: Schematic illustration of the HPCEF.



### 3. Experimental Setup

The counterflow burner in the liquid pool-autoignition configuration is placed inside a stainless steel chamber. In this configuration, the chamber is designed to carry out experiments up to 25 bar. A video camera put in front of one of the view ports provides feedback to the experimentalist. The chamber is equipped with four perpendicular view ports to observe the experiment. Gas for the experiment is supplied by twelve 232 cubic feet nitrogen gas bottles and three 220 cubic feet medical grade air gas bottles, pressurized up to 2500 psi. The mass flow controllers require an inlet pressure between 450 and 500 psi, therefore gas regulators reduce the gas pressure to 475 psi. Every mass flow controller has a pressure gage mounted right in front of the inlet in order to observe if every mass flow controller is supplied with the correct inlet pressure. This is crucial in order to verify the mass flow controllers work precisely. The oxidizer stream is mixed after the gases pass the mass flow controller setup. Once the oxidizer stream enters the HPCEF chamber, the stream is preheated by three 750 W OMEGA process heaters. The three process heaters are arranged in parallel and heat the stream up to 330°C. At the outlet of every process heater a sheathed K-type thermocouple gives feedback to a PID-controlled solid state relay which controls the power to the heater. In the next step, the oxidizer enters the “autoignition top” and is heated up to a maximum oxidizer duct outlet temperature of 1200 K. The heating elements within the oxidizer duct can be controlled through the LabVIEW counterflow control software. Due to the complexity of the experiment it is necessary to automate adjusting the setpoint of the transformer which controls the voltage to the silicon carbide heating element. In past experiments it has also been observed that the electromagnetic field of the transformer influences the accuracy of the mass flow controllers. The custom built setup uses a geared Nema 34 stepper motor mounted on top of a custom 3D printed ABS plastic rack. The shaft of the stepper motor mounts straight to the adjustment shaft of the transformer. Two limit switches prevent the stepper motor from exceeding the upper and the lower limit and therefore breaking the transformer internally. Figure 3-7 shows the transformer used to control the voltage to the main heating element with the stepper motor setup.

### 3. Experimental Setup



Figure 3-7: Remote controlled transformer to adjust the heating element voltage.

The suction is created by a back pressure valve which maintains a steady chamber pressure. All the gases that enter the chamber through various orifices, including the product gases created by the combustion process, leave the chamber through the annular suction gap in the lower part of the burner. The chamber pressure is controlled using a TESCO ER5000 PID controlled pressure regulation system. This system receives its feedback from a pressure transducer with an accuracy of  $\pm 0.7$  kPa located at the exhaust system of the pressure chamber.

The product gases are cooled using six Bete 1/8 in PJ20 water misting nozzles. A high pressure water pump, which can deliver water up to 100 bar, is installed to provide proper atomization of the cooling water. The cooling water and the product gases accumulate in a stainless steel box located at the bottom of the chamber where they are separated. The product gases are evacuated through the top of the box and the water is periodically drained through a solenoid valve which is activated by an Omega EZ515-AC-RC programmable relay using feedback of two Omega ultrasonic solid state liquid level switches. It is crucial that the water level does not exceed a certain level inside the box and drains through the product gas exhaust. A minimum wa-

### 3. Experimental Setup

ter level has to be maintained so the product gases don't evacuate through the water outlet. Both scenarios would cause unwanted pressure fluctuations.

Figure 3-8 shows the opened HPCEF chamber with the counterflow burner in the liquid pool-autoignition configuration sitting on the bottom plate of the chamber. The upper half of the frame shows the autoignition duct with the two power leads for the silicon carbide heating element on top. The autoignition oxidizer duct sits on top of the liquid pool fuel duct which is shown in the center of the frame. The water collector and separation unit can be seen in the bottom of the setup.

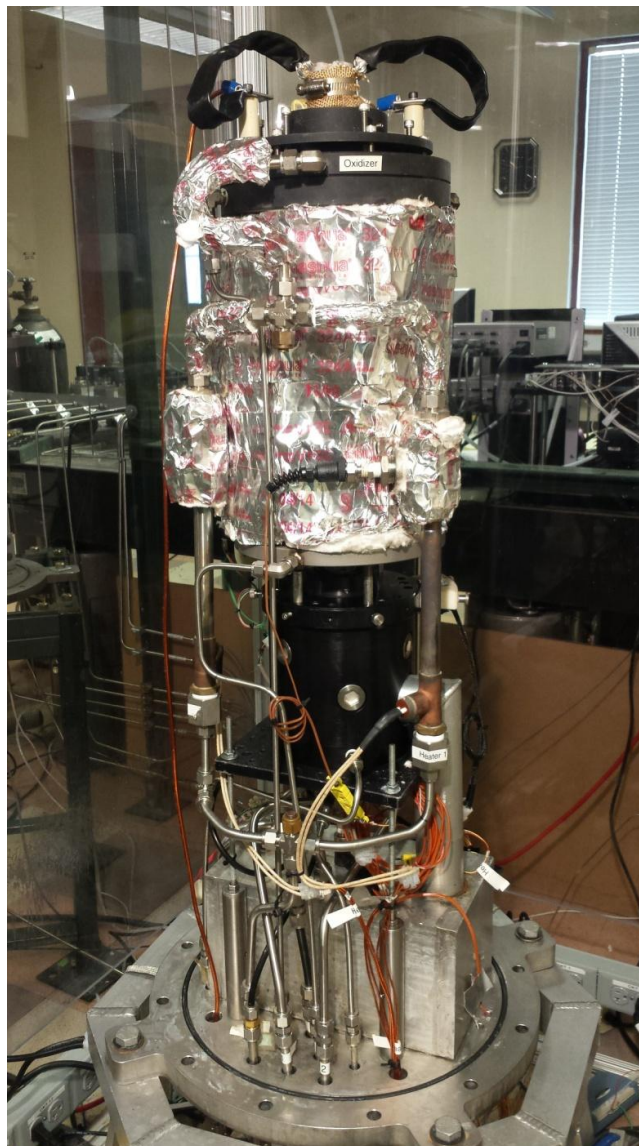


Figure 3-8: Experimental setup inside the pressure chamber.

### 3. Experimental Setup

To provide sufficient accuracy of the chamber pressure during the experiment, the pressure is monitored by three pressure transducers installed in different locations. The chamber pressure is regulated with a TESCOM PID-controlled backpressure regulation system. This system receives its feedback from a pressure transducer mounted in the exhaust of the experiment. In addition, there is a NIST calibrated OMEGA DPG-409-1K pressure gauge mounted on top of the chamber monitoring the chamber pressure. A third pressure transducer is mounted in the bottom of the chamber and provides feedback to the LabVIEW experimental software.

The liquid fuel is supplied by a high precision Teledyn Isco 1000D syringe pump with a volumetric flow accuracy of  $\pm 0.01$  ml/min.

For visual feedback of the experiment inside the chamber and to maintain a steady level of fuel inside the fuel duct, a Canon T4i Rebel with a 60 mm macro lens is used. The camera is positioned in front of a viewport. The live feedback from this camera is displayed on a separate screen next to the LabVIEW control software. Maintaining the fluid level inside the liquid pool cup is crucial. A change in the separation distance between the fluid level and the oxidizer outlet would change the effective strain rate and therefore autoignition temperature. Figure 3-9 shows a screenshot of the live video feed the experimentalist uses to maintain a steady level of liquid fuel inside the liquid pool cup.

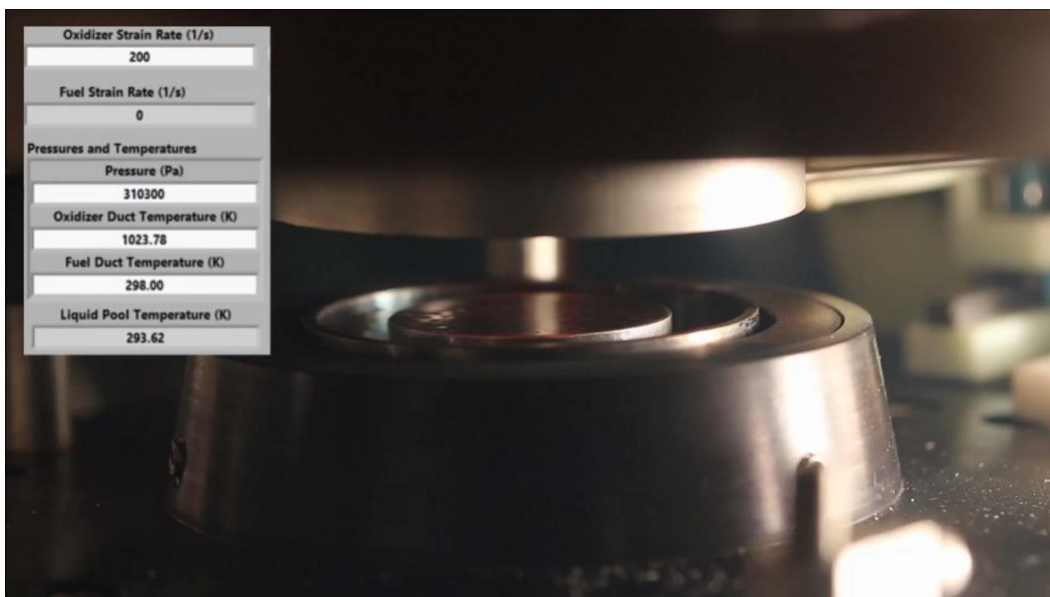


Figure 3-9: Screenshot of the live video feed of the experiments.

### 3. Experimental Setup

To observe every autoignition event and determine the exact point of ignition, initially a FASTCAM Super 10K high speed camera is used. This camera provides video footage of 512 x 480 pixels at 500 frames per second. For later experiments a Phantom VEO 410 high speed camera is used. This camera provides video footage of 5200 frames per second at a screen resolution of 1280 x 800. Every autoignition event of the experiment is recorded with the use of a high speed camera and evaluated for the exact location of autoignition within the flow-field. Only if the autoignition occurs in the center of the flow-field, the observed autoignition temperature is considered valid.

Additional detailed information about the experimental setup can be found in previous publications [18].

#### 3.2.1 Experimental Pressure Chamber

The main part of the HPCEF is a cylindrical stainless steel pressure chamber, which in its current iteration measures 108 cm from top to bottom, has an inner diameter of 35 cm and a wall thickness of 16 mm. The chamber is designed to withstand pressure up to 150 bar and has been pressure tested up to 100 bar. To fit the new high pressure counterflow burner experiment, the height of the chamber has to be extended in height with a 38 mm extension ring. To allow for visual access of the experiment, the chamber is equipped with four perpendicular view ports. Figure 3-10 shows a photograph of the stainless steel chamber detached from the bottom plate. Three of the four view ports are visible. The chamber is opened and closed by using a crane mounted on the ceiling of the room and attached to the bottom plate with twelve screws.

### 3. Experimental Setup

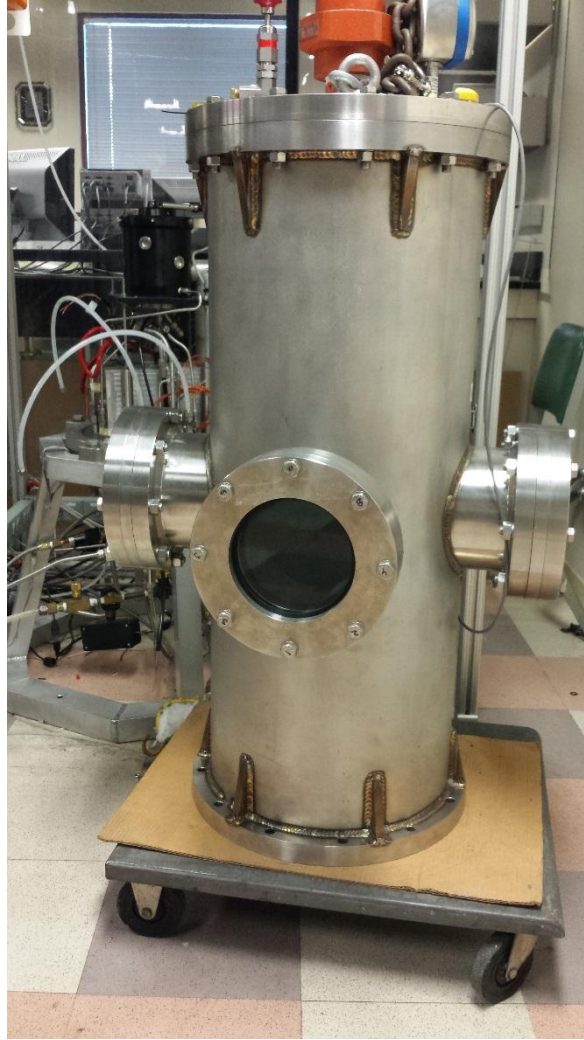


Figure 3-10: Stainless steel pressure chamber.

Due to the higher chamber temperatures of autoignition experiments and to meet the demands for future experiments carried out at higher pressures, the windows have to be updated. The new fused glass sight windows have a clear aperture of 78.5 mm and are tested for pressures up to 345 bar at a maximum temperature of 673 K. The windows are mounted at the four flanges on the cylindrical body of the chamber using custom made adapter plates and are sealed using O-rings. Figure 3-11 shows the view port with the glass window and the adapter plate.



### 3. Experimental Setup



Figure 3-11: View port with the glass insert and the adapter plate.

The bottom of the chamber is a 25 mm thick stainless steel plate and contains several high pressure throughputs for electrical wiring, gas and water streams. To meet the requirements for the latest experiment, the stainless steel plate of the chamber has to be modified to feed through power and thermocouple wires for the several heating elements necessary for the new high pressure autoignition experiment. The chamber sits on an aluminum rack for better access to conduct maintenance.

### **Safety Features**

The major safety concern of experiments carried out with the High Pressure Combustion Experimental Facility is exceeding the maximum design pressure of the stainless steel chamber either caused by an excess of gas flow into the chamber or an explosion inside the chamber. Several safety measures have been implemented into the experimental setup to prevent this from happening. The gases used for this experiment come in gas bottles pressurized up to 170 bar. A malfunction of a mass flow controller could therefore lead to a dangerous pressure increase inside the chamber. To prevent this, all gas supply lines for the experiment are equipped with pressure regulators set to 34 bar, which is the required supply pressure for the mass flow con-

### 3. Experimental Setup

trollers. Several pressure gauges on the gas supply lines are installed and monitored to ensure a safe system pressure. Another safety feature is a Swagelok SS-4R3-MO proportional spring loaded relief valve, that is mounted on top of the chamber, which will slowly release gas once the chamber is reaching a critical pressure. Another safety feature to prevent overpressurization of the chamber is an Oseco burst disc, also mounted on top of the chamber. This device is set to burst at 36,5 bar and would release all the gases in the chamber at once. This feature is installed in case one or more delivery gas pressure regulators fail or an explosion inside the chamber occurs. The final measure is transparent high-impact polycarbonate surrounding the chamber to protect room occupants from the hazard of shattered glass pieces in case one or more of the view port windows burst. Figure 3-12 shows the upper part of the high pressure chamber with the chamber extension plate, burst disc adapter, high precision pressure gauge and relief valve.



Figure 3-12: Upper part of the pressure chamber with the safety devices.



#### 3.2.2 High Pressure Autoignition Oxidizer Duct

This chapter describes the latest duct for autoignition experiments inside the High Pressure Combustion Experimental Facility, referred to as the "autoignition top". The design is based on a previous autoignition duct for the atmospheric counterflow burner setup and has been improved and adapted to meet the requirements of higher flow rates and pressures for autoignition experiments at elevated pressures. Figure 3-13 shows a CAD-model cross-sectional view of the "autoignition top".

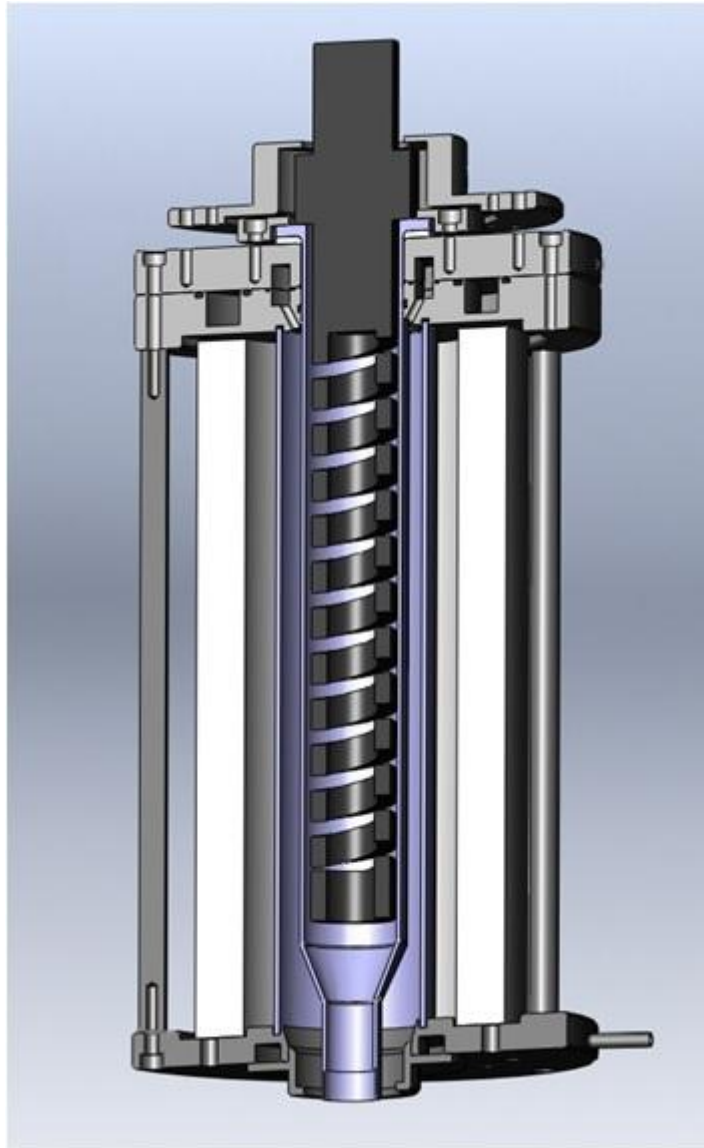


Figure 3-13: Cross-sectional view of the autoignition duct.

### 3. Experimental Setup

The main part of the "autoignition top" is a 380 mm long silicon carbide heating element with a diameter of 38 mm. At full power the heating element can reach a surface temperature of 1900 K and draws 4400 W. The oxidizer stream is guided towards the reaction zone and separated from the nitrogen curtain through a quartz tube. This quartz tube is a custom made piece, specifically designed for this setup. Quartz is chosen due to its good high temperature resistance and low thermal expansion. The oxidizer stream enters the quartz tube through a small circular opening on top. At the outlet of the oxidizer duct three Inconel 600 mesh screens with a wire diameter of 51  $\mu\text{m}$  and an open area of 36 % are placed to achieve a laminar axisymmetric plug flow. The screens are kept in place by using four Inconel retaining rings. Due to the significant higher thermal expansion of Inconel compared to quartz, the rings have a 1 mm gap cut out to prevent the quartz from cracking when they expand under experimental conditions. The retaining rings recess the screens by 1 mm and reduce the effective oxidizer duct diameter to 23 mm. A second quartz tube is used to guide and separate the nitrogen curtain from the surroundings. This quartz tube is also custom made for this application. The frame of the "autoignition top" consists of two major parts. The upper part consists out of four pieces made out of machined and anodized aluminum. Aluminum is chosen because of its superior heat conductivity and machinability compared to stainless steel. This part of the frame contains the inlet ports for the oxidizer stream and the nitrogen curtain. The port for the oxidizer stream is lined with Macor ceramic to reduce the heat transfer in this area to a minimum. The oxidizer stream port guides the stream straight to the main silicon carbide heating element through a circular opening in the quartz tube. An O-ring is used to provide a seal between the quartz tube and the aluminum frame. The nitrogen stream inside the frame is directed to 12 openings which are arranged annular around the inner quartz tube. Due to the high temperatures within this assembly, it is necessary to actively cool it with water. The cooling water enters the "autoignition top" in the upper part of the frame and then flows through a stainless steel braided hose into the lower part of the frame. The channels for the gases and the cooling water within the assembly are separated by O-rings. In order to prevent cracking of the quartz tube and seal off the oxidizer stream, a sheet of graphite gasket is put between the quartz and the aluminum frame. To align the quartz tube and keep it in its place, a circular aluminum part, referred to as "quartzlocker",

### 3. Experimental Setup

is mounted on top of the quartz tube. It is mounted using six screws that allow for a precise adjustment of the oxidizer duct outlet. To provide protection of the quartz tube and sealing, the lower part of the "quartzlocker" is lined with graphite gasket as well. It is crucial that the silicon carbide heating element never touches the inner face of the oxidizer quartz tube. The top part in the assembly referred to as "Cap", fixates the silicon carbide heating element using six set screws. A separate assembly has been designed that allows the silicon carbide to be aligned within the "Cap". Two porcelain standoff insulators are mounted on top of the assembly to fixate the leads of the silicon carbide heating element. Figure 3-14 shows a photograph of the fully assembled "autoignition top".



Figure 3-14: The "autoignition top" for elevated pressures.

### 3. Experimental Setup

The lower part of the frame consists of two parts of machined stainless steel welded together and is cooled by water internally. The "autoignition top" is mounted on the lower part of the burner using three threaded 3/8 in diameter rods. Therefore, the lower part contains 12 threaded holes to provide flexibility on the way the "autoignition top" is mounted on the fuel duct of the burner. The threads allow for a precise adjustment of the duct separation distance. In order to prevent heat loss and increase the temperature of the nitrogen curtain, two semi-cylindrical ceramic heating elements with 1100 W heating power each surround the oxidizer and nitrogen curtain duct. Additionally, thermal insulation is wrapped around the two semi-cylindrical heating elements to reduce heat loss.

#### 3.2.3 Liquid Pool Duct

The liquid pool burner assembly for elevated pressures has been designed and built by Ryan Gehmlich [69] and is shown in Figure 3-15. The fuel enters the apparatus through the bottom and is directed into the liquid pool cup. A J-type thermocouple is located at the bottom of the liquid pool cup and measures the temperature of the liquid fuel. A water spray is constantly cooling the bottom of the brass liquid pool cup to maintain constant temperatures. Inside the liquid pool cup, a needle is mounted which is used as an indicator to help visually level the fluid inside the cup. A screen is placed inside the cup to reduce turbulences within the liquid volume. If overflowing of the fuel cup occurs, the fuel runs down the nitrogen curtain duct and is then collected in a separate container. The product gases are sucked down into the burner through an annular duct surrounding the nitrogen curtain duct, cooled by fine water mist sprays and then collected in the water separator unit at the bottom of the chamber. The aluminum body of the liquid pool duct is actively cooled by water internally.

### 3. Experimental Setup

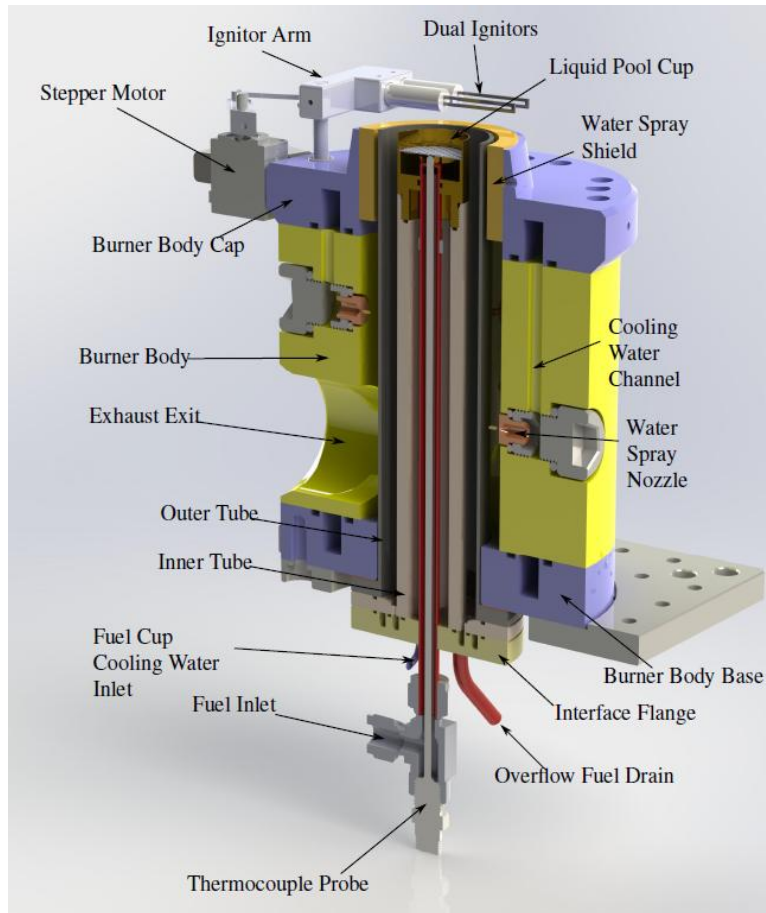


Figure 3-15: Cross sectional view of the liquid pool duct.

Figure 3-16 shows the two opposing ducts of the counterflow burner with the oxidizer duct on top, the fuel duct at the bottom and the R-type thermocouple coming in from the left hand side of the frame. The separation distance between the outlet of the oxidizer duct and the top of the liquid pool cup is set to 12 mm in this experiment. The bead of the thermocouple for measuring the oxidizer duct temperature is put as close as possible to the outlet of the oxidizer duct.

### 3. Experimental Setup

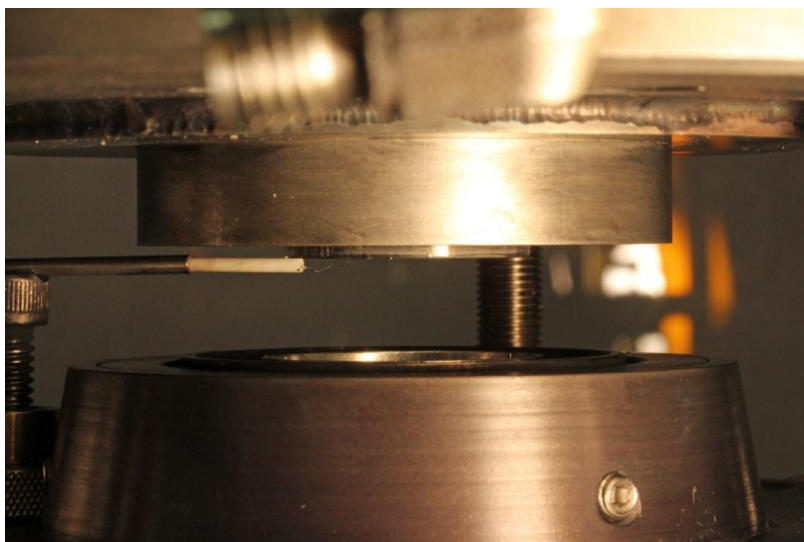


Figure 3-16: Close up view of the liquid pool experiment.

#### 3.2.4 HPCEF Control Station

The HPCEF control station consists of two computer screens, the mass flow controller “Power Pods” in the center and the mass flow controller setup, which cannot be seen in this frame. Figure 3-17 shows the HPCEF control station.



Figure 3-17: HPCEF Control Station.

### 3. Experimental Setup

The two “Power Pods” supply power and convert the digital signal from the computer to an analog signal for each mass flow controller. They are also equipped with a digital display to give the operator feedback if the mass flow controllers have received the latest set point.

The computer screen on the right side provides the operator with a live video feedback from the inside of the HPCEF pressure chamber. The screen on the left displays the counterflow control software. The majority of the functions of the experiment are controlled using a custom made counterflow control software. Data acquisition and control of the experiment is handled through a National Instruments PXI instrumentation platform. In case of an emergency, the operator can shut off all gas streams manually at the control station. Every mass flow controller is equipped with a shut off valve.

### 3.3 Counterflow Control Software

Due to the complexity of the counterflow experiment, automation of many functions is necessary. The counterflow control software is a custom made LabVIEW (Laboratory Virtual Instrumentation Engineering Workbench) program. The software for the High Pressure Combustion Experimental Facility is based on the software for the atmospheric counterflow setup and has been extended to carry out experiments at elevated pressures. Figure 3-18 shows the main screen of the counterflow control software in the configuration for conducting experiments with the High Pressure Experimental Combustion Facility.

### 3. Experimental Setup

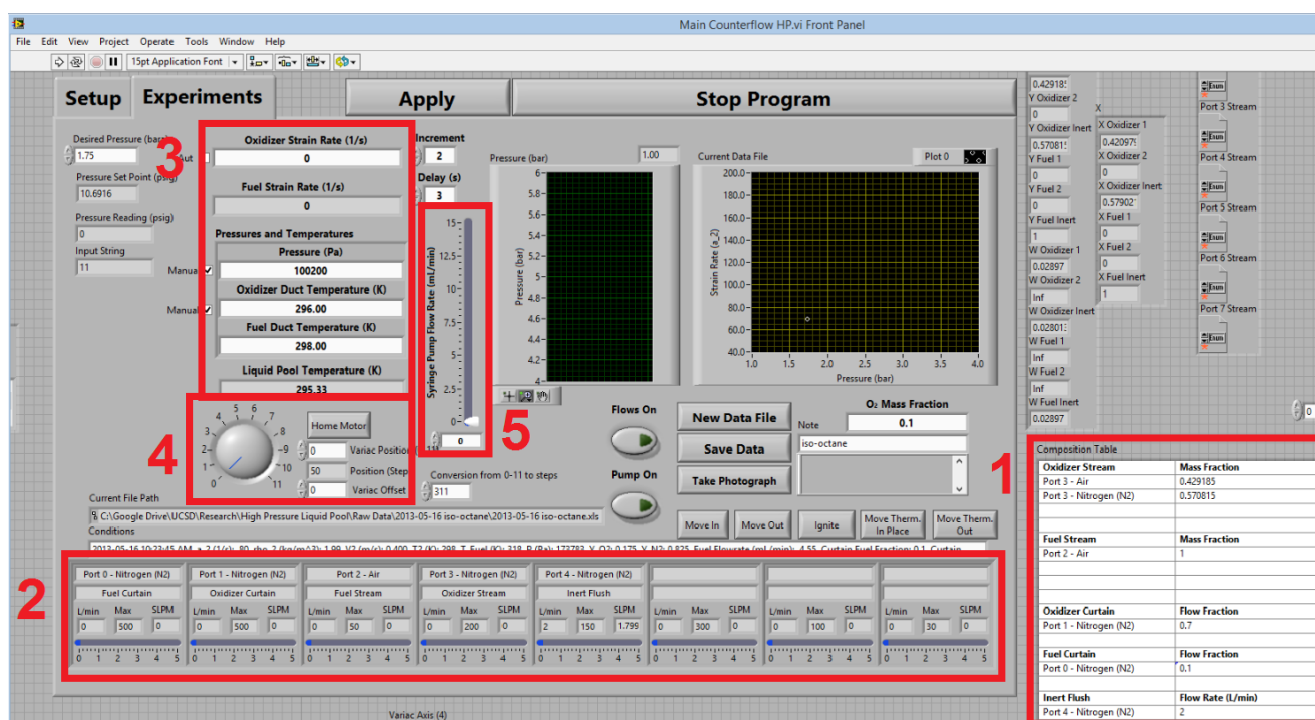


Figure 3-18: Main screen of the counterflow control software.

The most important features are described here briefly:

1. On the lower right side of the screen, the operator can set the desired fuel and oxidizer stream mass fractions, the nitrogen curtain flow rate and an additional stream referred to as "Inert Flush".
2. Here, the counterflow software displays the current setpoints for each mass flow controller in standard liters per minute and liters per minute for the conditions within the flow-field. To verify the mass flow controllers have received their assigned setpoint, these values are regularly compared to the values at the display on the mass flow controller power supply.
3. The oxidizer stream strain rate is set here, the fuel stream strain rate is calculated employing a momentum balance and is set automatically, the reactant temperatures and ambient pressure can be observed.
4. This knob sets the desired set point for the transformer regulating the voltage to the silicon carbide heating element for autoignition experiments.



### 3. Experimental Setup

5. Here the flow rate of liquid fuel for experiments involving the liquid pool configuration is set.

Additionally, the software receives the following inputs from the operator:

- The current counterflow configuration. The counterflow can be equipped with several different fuel and oxidizer ducts depending on the subject of research. The counterflow software has the geometries for all burner configurations stored. The geometries of interest are duct separation distance, fuel and oxidizer duct diameters and the area of fuel and oxidizer side nitrogen curtain outlets. This is crucial for calculating the setpoints for each mass flow controller, which is described in detail later in the text.
- The constituents of the reactant streams. The counterflow control software has the physical and chemical properties for many substances stored.
- The latest value for calibration for every mass flow controller.
- The desired chamber pressure for experiments involving elevated pressures.

The counterflow control software receives input from multiple temperature and pressure sensors throughout the counterflow setup. The most crucial are:

- The temperature of the reactant streams measured at the fuel and oxidizer duct outlets.
- Ambient pressure for the location where the counterflow burner is located.

With these inputs the software calculates the required setpoint for each mass flow controller to achieve the desired conditions within the flow-field of the counterflow burner. The software recalculates the set points every second using the latest acquired data from various sensors throughout the experiment.

The counterflow control software calculates the setpoints for the mass flow controllers as follows. Assuming the fuel mass fraction in the fuel stream and the oxygen mass fraction in the oxidizer stream have already been determined, the nitrogen mass fractions for both reactant streams can be calculated with the following equations. Index 1 refers to the fuel side of the flow-field and index 2 refers to the oxidizer side of the flow-field.

### 3. Experimental Setup

$$Y_{N_2,1} = 1 - Y_{F,1} \quad (13)$$

$$Y_{N_2,2} = 1 - Y_{O_2,2} \quad (14)$$

The mole fractions for fuel and oxidizer stream are determined by equations (15) and (16).  $W_i$  [g/mole] is the molecular weight of the regarding element.

$$X_{i,1} = \frac{\frac{Y_{i,1}}{W_{i,1}}}{\sum_{F,N_2} \frac{Y_{i,1}}{W_{i,1}}} \quad (15)$$

$$X_{i,2} = \frac{\frac{Y_{i,2}}{W_{i,2}}}{\sum_{O_2,N_2} \frac{Y_{i,2}}{W_{i,2}}} \quad (16)$$

By employing the ideal gas equation, the density  $\rho_i$  [kg/m<sup>3</sup>] of the fuel and oxidizer stream can be calculated with equations (17) and (18).

$$\rho_1 = \frac{p \sum_{i=N_2,F} X_{i,1} W_{i,1}}{RT_1} \quad (17)$$

$$\rho_2 = \frac{p \sum_{i=N_2,O_2} X_{i,2} W_{i,2}}{RT_2} \quad (18)$$

$T_1$  and  $T_2$  [K] refer to the fuel and oxidizer stream temperatures at the duct outlets. The ambient pressure is denoted as  $p$  [Pa].  $R = 8.314$  [J/moleK] is the ideal gas constant.

The velocity for the oxidizer stream at the oxidizer duct outlet can be determined by the set strain rate. The velocity for the fuel stream at the fuel duct outlet can be determined by employing the momentum balance (2).

### 3. Experimental Setup

$$V_1 = \frac{V_2}{\sqrt{\frac{\rho_1}{\rho_2}}} \quad (19)$$

Knowing the reactant stream velocities, the volume flux for every species in the reactant stream can be calculated with the following equations.

$$\dot{V}_{F,1} = X_{F,1} V_1 A_1 \quad (20)$$

$$\dot{V}_{N_2,1} = X_{N_2,1} V_1 A_1 \quad (21)$$

$$\dot{V}_{O_2,2} = X_{O_2,2} V_2 A_2 \quad (22)$$

$$\dot{V}_{N_2,2} = X_{N_2,2} V_2 A_2 \quad (23)$$

The volume flux of the nitrogen curtains for both ducts are calculated with the following equations.  $C_1$  and  $C_2$  are the factors for setting the nitrogen curtain flow velocities relative to the reactant streams.

$$\dot{V}_{c,1} = C_1 V_1 A_1 \quad (24)$$

$$\dot{V}_{c,2} = C_2 V_2 A_2 \quad (25)$$

The values of the volume fluxes are converted to stand liters per minute [SLM], which is the unit the mass flow controllers require.

$$\dot{V}_{SLM;i,j} = \dot{V}_{i,j} \frac{273,15K}{T_{i,j}} \quad (26)$$

## 3.4 Flow Control

For accurate reactant flow control, Teledyne Hastings HFC-303 and HFC-302 mass flow controllers are employed. The HPCEF setup is equipped with eight Teledyne Hastings HFC-303 mass flow controllers with flow ranges from 30 to 500 SL. To achieve maximum accuracy of the mass flow controllers, they need to be calibrated near the flow range and pressure they will be used in the experiment. Therefore either a Ritter TG5ER wet test meter with a flow range of 0.167 L/min to 33.3 L/min or a Ritter TG50 wet test meter with a flow range from 1.67 L/min to 300 L/min is used. To allow for calibration of the mass flow controllers under pressure, an adjustable back pressure valve is used to create the desired pressure at the outlet. Before every calibration, the water level of the wet test meter has to be checked and if necessary adjusted. The mass flow controllers of the reacting streams are calibrated to a maximum deviation of 0,5 % for the flow rang they are used in the experiment.

Figure 3-19 shows the mass flow control setup with Teledyne Hastings HFC-303 mass flow controllers in the high pressure laboratory. As seen in the photograph, every mass flow controller gas supply line is equipped with a separate pressure gauge to ensure the mass flow controllers are operated within the correct pressure range to provide maximum accuracy.



Figure 3-19: HPCEF mass flow controller setup.

## 3.5 Gas Supply

For experiments carried out within the HPCEF, all gases come in gas bottles pressurized up 170 bar. The oxidizer used is medical grade air. For all other inert gas streams high purity nitrogen is used. Additionally to the pressure gauges mounted in front of every mass flow controller, every supply line is equipped with a pressure gauge and a regulator at the bottle to ensure the correct gas pressures.

For experiments carried out employing the atmospheric counterflow setup, the oxidizer used is pressurized air from the in-house air system. All other inert gases and fuels also come in gas bottles pressurized up to 170 bar.

Figure 3-20 shows a part of the gas supply for the High Pressure Combustion Experimental Facility. Up to four gas bottles are grouped together to one manifold.



Figure 3-20: Part of the gas supply used for the HPCEF.

## 3.6 Measurement of Autoignition Temperature

The oxidizer temperature is measured using an R-type thermocouple located at the oxidizer duct outlet. It is crucial, that the influence of the thermocouple on the flow-field is as small as possible. The thermocouple used in these experiments are custom made bare wire R-type (Pt 13% Rh/Pt) thermocouples. The bare thermocouple wire is fed through a two hole ceramic tube insulator for protection. Only the bare thermocouple wire with the wire junction penetrates the flow-field. It is observed, that the wire diameter has a crucial influence on the location of autoignition within the flow-field and therefore might cause premature autoignition. With the help of the visual feedback of a high speed camera, a wire diameter of 0,127 mm or less eliminates the influence on the flow-field. A smaller diameter thermocouple also is more responsive to temperature changes, requires less correction for radiative heat loss and is therefore more accurate. To adjust the position of the thermocouple within the flow-field, it is mounted on a custom made stepper motor driven xy-stage that can be controlled remotely via the counterflow control software. Figure 3-21 shows a picture of a custom made R-type thermocouple as used in the experiments.

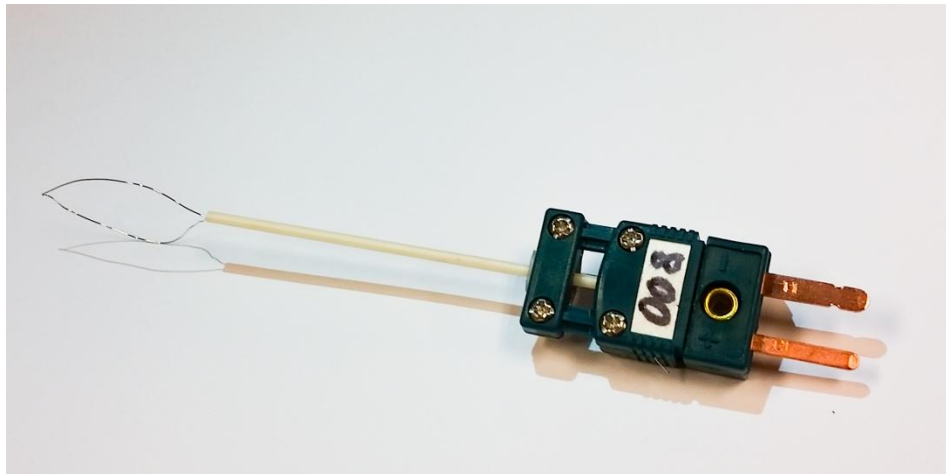


Figure 3-21: Thermocouple used to measure oxidizer duct temperature.

#### 3.6.1 Temperature Correction

A thermocouple consists of two wires of different materials forming a junction. A temperature depending voltage is induced as a result of the thermoelectric effect or Seebeck effect. The measured voltage is an indicator for the magnitude of the change in temperature. The measured temperature of a thermocouple is not actually the temperature of the surrounding medium, it is the temperature of the thermocouple junction. Therefore the measured value for temperature has to be corrected to obtain the real gas temperature.

The real gas temperature is obtained by employing an energy balance for the thermocouple wire junction [70]. The junction is heated by convection of the surrounding hot gas and receives energy through radiation from the silicon carbide heating element above. Conduction through the thin thermocouple wires is considered to be neglectable and is therefore ignored. The temperature of the Inconel mesh screens at the oxidizer duct is assumed to be the same temperature as the thermocouple junction. The radiating surface of the thermocouple wire junction is therefore divided by two.  $q_{Convection}$  denotes the heat flux due to convection and  $q_{Radiation}$  denotes the heat flux due to radiation.  $A_{jun}$  refers to the surface area of the thermocouple junction,  $T_{gas}$  is the gas temperature,  $T_{sur}$  is the temperature of the surrounding surfaces,  $T_{jun}$  is the temperature of the thermocouple junction,  $\sigma$  is the Stefan-Boltzmann constant ( $5,67 \cdot 10^{-8} \text{ W/m}^2\text{K}^4$ ),  $\epsilon$  is the emissivity of the thermocouple wire junction and  $h$  is the convective heat transfer coefficient. The value for emissivity is obtained by the thermocouple wire manufacturer. Catalysis effects on the thermocouple wires are neglected. The thermocouple wire junction is presumed to be spherical. The diameter of that sphere is measured under a microscope for every thermocouple used to measure oxidizer temperatures. Since the difference between real gas temperature and measured gas temperature increases with the thermocouple diameter, it is desirable to use the thinnest thermocouple wire available.

### 3. Experimental Setup

$$q_{Convection} = q_{Radiation} \quad (27)$$

$$h * \frac{A_{Jun}}{2} * (T_g - T_{Sur}) = \frac{A_{Jun}}{2} * \varepsilon * \sigma * (T_{Jun}^4 - T_{Sur}^4) \quad (28)$$

The convective heat transfer coefficient  $h$  is defined by

$$h = \frac{Nu * k_{gas}}{D_{Jun}} \quad (29)$$

where  $D_{Jun}$  is the diameter of the thermocouple wire junction and  $k_{gas}$  is the thermal conductivity of the surrounding gases. The Nusselt number  $Nu$  is calculated by the following equation which is applicable for forced convection over a sphere.

$$Nu = 2 + 0,6 * Re^{\frac{1}{2}} * Pr^{\frac{1}{3}} \quad (30)$$

$Re$  is the Reynolds number and  $Pr$  is the Prandtl number. The Reynolds number is defined as

$$Re = \frac{\rho_{gas} V_{gas} D_{Jun}}{\mu_{gas}} \quad (31)$$

where  $\rho_{gas}$  is the density of the gas,  $V_{gas}$  is the velocity of the gas at the thermocouple and  $\mu_{gas}$  is the viscosity of the gas. The gas velocity  $V_{gas}$  is calculated by the counterflow control software. The density of the gas is calculated by

$$\rho_{gas} = \frac{p}{RT_{gas}} * MW_{gas} \quad (32)$$

where  $p$  is the pressure,  $MW_{gas}$  is the molecular weight of the gas and  $R$  is the ideal gas constant. The Prandtl number is calculated by the following equation



$$Pr = \frac{c_p * \mu_{gas}}{k_{gas}} \quad (33)$$

where  $c_p$  is the gas heat capacity.

## 3.7 Experimental Procedure

To ensure an accurate experimental investigation, it is crucial to strictly enforce the experimental procedure for every data point to obtain comparable experimental results. The most relevant steps of the experimental procedures for the atmospheric counterflow and HPCEF are explained in this chapter.

### 3.7.1 Atmospheric Counterflow Procedure

Since this study consists of experimental investigations of autoignition and extinction characteristics in a counterflow configuration, there are two different procedures to follow. In both cases, the mass flow controllers for the reacting streams are calibrated for every data point to a maximum deviation of 0,5 %. A Ritter TGR5 drum type wet test meter is used for calibration and is inspected before every performed calibration to ensure accurate flow control. In case of experiments involving dimethyl ether it is observed that, in order to support a certain dimethyl ether mass flow, the bottle needs a certain gas pressure. This is particularly crucial for data points with higher dimethyl ether mass fractions. To provide sufficient accuracy for the fuel stream, the dimethyl ether channel is calibrated for every single measured data point. If experimental investigations involving liquid fuels are carried out, the vaporizer is employed. The vaporizer fuel supply line from the vaporizer to the burner bottom duct is preheated. The temperature to which it is preheated depends on the boiling point temperature of the fuel investigated and is

### 3. Experimental Setup

monitored regularly to prevent condensation or cracking of the fuels molecules. The heated fuel delivery system is routinely checked for condensation by reducing the fuel mass fraction to zero. The flame has to extinguish immediately. The vaporizer can also be opened and inspected visually. All cooling circuits are enabled. The desired reactant mass fractions and oxidizer strain rate are set and the flow-field is established. The gap between the oxidizer and the fuel duct is measured before and after the experiment with a micrometer to prevent a deviation of the experimental data due to thermal expansion.

#### Autoignition procedure:

The desired oxidizer strain rate is set in the counterflow control software and is automatically maintained. The temperature of the oxidizer stream is gradually increased in small increments by increasing the power to the silicon carbide heating element, allowing sufficient time for the system to reach steady-state conditions until autoignition takes place. When autoignition occurs, the data is recorded, the power to the heating element is reduced and the flame is extinguished by increasing the nitrogen mass fraction in the oxidizer stream. After the temperature has significantly dropped, the experiment is repeated to verify the data point. The recorded autoignition temperatures are corrected for radiative heat loss.

#### Extinction procedure:

To obtain accurate data, the counterflow burner has to be conditioned first. This is done by having a flame burn until the apparatus reaches a steady operating temperature. For every data point, the flame is ignited at an oxidizer strain rate considerably lower than the expected oxidizer extinction strain rate. The flame is ignited by using a propane torch. The factors for the relative oxidizer and fuel side nitrogen curtain velocities are both set to 0,5. The oxidizer strain rate is then increased in small increments by  $1 \text{ s}^{-1}$  every 5 seconds to ensure steady state conditions are reached until extinction occurs. The oxidizer strain rate is then lowered significantly, the flame is ignited and the experiment is repeated again. If the data point is repeatable several times, it is considered a valid data point.

### 3. Experimental Setup

Figure 3-22 shows a DME flame in the atmospheric counterflow burner at  $\xi_{st}=0,4$  and  $a_2=480\text{ s}^{-1}$ .



Figure 3-22: DME flame in the atmospheric counterflow burner.

#### 3.7.2 HPCEF Procedure

Before every experiment, the mass flow controllers for the reacting streams are calibrated to a maximum deviation of 0,5%. The desired chamber pressure and inert atmosphere is achieved by introducing nitrogen into the experimental pressure chamber. The flow-field is established by setting the desired oxidizer strain rate and oxidizer oxygen mass fraction in the HPCEF control software. In addition, a constant stream of about 50 slpm of nitrogen is introduced through the bottom of the chamber in order to maintain the nitrogen atmosphere inside the chamber and provide sufficient mass flow for the suction system. The liquid pool cup is filled with fuel and a steady fluid level is maintained with the help of the feedback from the live video feed. The flow rate of the syringe pump is adjusted constantly to match the rate of evaporation of the fuel. Figure 3-23 shows a detailed photograph of the liquid pool cup with the needle used for visual reference to maintain a steady level of fuel.

### 3. Experimental Setup



Figure 3-23: Detail of the liquid pool cup.

The three different water cooling circuits for the cooling of the autoignition duct, liquid pool cup and product gases are activated. The three process heaters are set to preheat the oxidizer to 330°C before it reaches the "autoignition top". The ceramic cylindrical furnace heater inside the "autoignition top" is activated. The power to the main heat silicon carbide heating element inside the "autoignition top" is increased in small increments until autoignition occurs. Slow temperature increase is necessary in order to decrease the risk of breaking the heating element or the quartz tube due to stress caused by thermal expansion.

Once autoignition occurs, the trigger of the high speed video camera is activated to capture the autoignition event. The camera is set to record the previous six seconds before the trigger is activated. The recorded video footage is immediately evaluated. Only if the ignition occurs within the center of the flow-field, the data point is considered valid. The recorded autoignition temperatures is corrected for radiative heat loss after the experiment. To extinguish the flame, the oxidizer oxygen mass fraction is reduced to 0.06 %. The power to the main silicon carbide heating element is reduced to decrease the oxidizer temperature. The remaining fuel left inside the liquid pool cup is drained and replaced with fresh fuel for the next data point. Once the oxidizer temperature has significantly dropped, the oxidizer oxygen mass fraction is set back 0.15 % and the experiment is repeated several times to verify the data point. Once all data points are taken, the chamber is opened immediately to measure the separation distance between

### 3. Experimental Setup

oxidizer duct and the liquid pool surface under operating temperatures. This is done in order to verify that the separation distance has not changed due to thermal expansion.

Figure 3-24 shows a series of high speed pictures of an autoignition flame at 4 bar which is typically used for evaluating the autoignition event. The fuel in this case is Jet A. The dark images are a result of the high frame rate the camera is set to. The area of the flow-field is actually illuminated with a bright light, which is necessary to maintain a steady liquid fuel level inside the liquid pool cup.

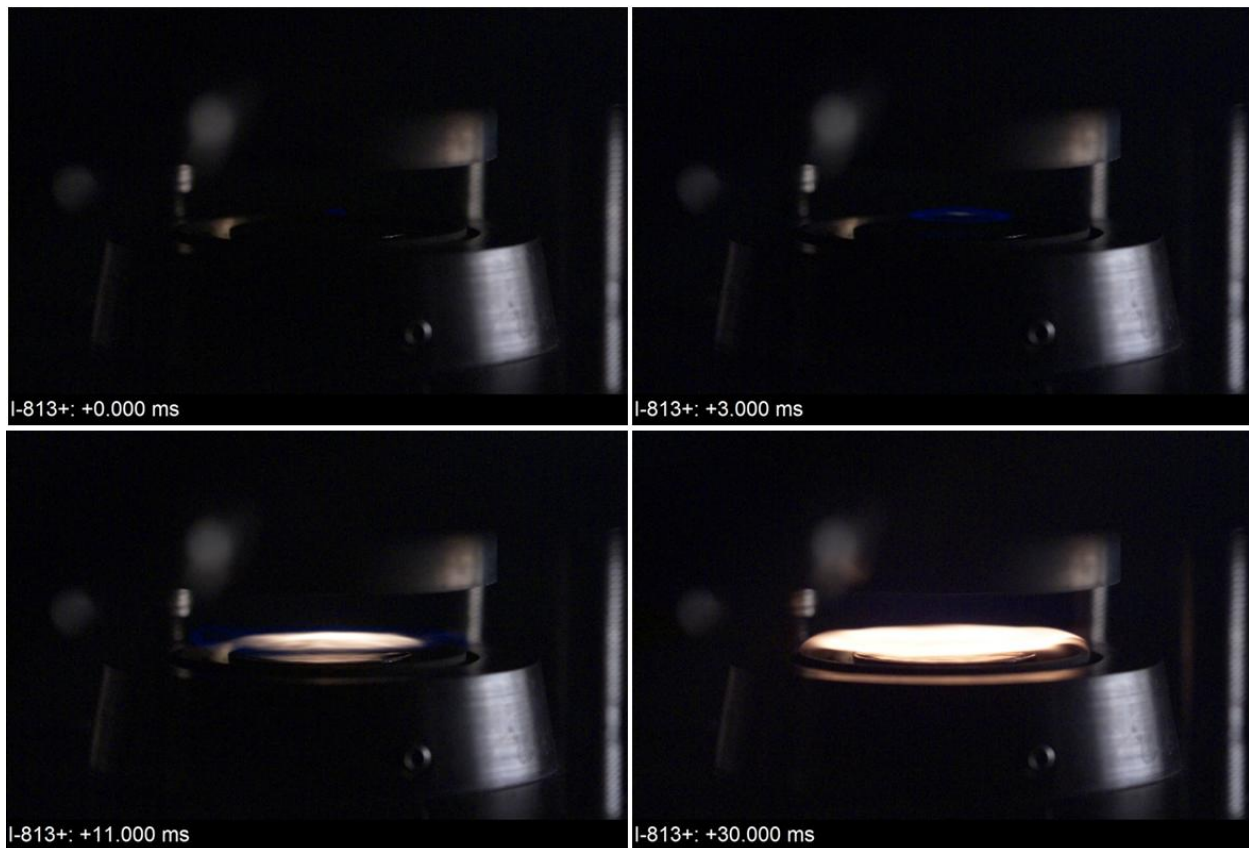


Figure 3-24: Autoignition event of Jet-A at 4 bar captured in slow motion at 1000 frames per second.

The footage is shot at a frame rate of 1000 frames per second. The frames show a close up view of the liquid pool cup in the middle, the concentric fuel side nitrogen curtain outlet and the surrounding product gas suction gap. In the lower left corner of every frame the time passed after the autoignition event has started is printed. The thermocouple is not visible in this view. The

### *3. Experimental Setup*

first picture at 0 ms shows the onset of autoignition with a small blue flame in the center of the liquid pool cup. This is therefore considered a valid data point. The second and third picture are taken 3 ms and 11 ms after autoignition and show the flame steadily propagating towards the suction gap. The fourth picture at 30 ms after autoignition shows the fully formed yellow glowing flame.

## 4 Numerical Computations

The experimental investigations are carried out in conjunction with numerical computations in order to verify and update chemical kinetic mechanisms. The computations for the different fuels and experimental configurations are performed in collaboration with several research groups around the globe and are described in more detail in this chapter.

### 4.1 Jet Fuel Surrogates

The numerical computations for the study on jet fuels are performed in collaboration with the Creck modeling group at the Polytechnic University of Milan.

The kinetic modelling for the three pure hydrocarbons, n-heptan, n-decane and n-dodecane is carried out by first constructing a skeletal chemical-kinetic mechanism from the POLIMI-1412 detailed chemical kinetic mechanism [71]. The detailed mechanism describes the pyrolysis and combustion of hydrocarbons up to C<sub>16</sub> and oxygenated fuels [72]. It uses a lumped approach for the description of the primary propagation reactions from high molecular weight species to lower molecular weight species. The reactions of these low molecular weight species are then described using a detailed chemical kinetic mechanism. The approach of employing a lumped chemical kinetic mechanism has been discussed by Ranzi *et al* [73]. Mechanism reduction has been performed using the DoctorSMOKE+ + code software [74]. The skeletal mechanisms have been verified by comparing ignition delay times predictions in adiabatic constant pressure batch reactors with those of a detailed scheme over a temperature range from 500 to 1700 K and pressures up to 40 bar. Since the topic of interest in this study are the predictions of critical conditions of autoignition in non-premixed flows, the skeletal mechanisms are tested for a wide range of equivalence ratios  $\phi$ . The three skeletal mechanisms are made up of about 3000 reactions among 117 species for n-heptane, 122 for n-decane and 136 for n-dodecane. To ensure

#### 4. Numerical Computations

the reduced mechanism retains the predictive accuracy of the POLIMI mechanism, Figure 4-1, 4-2 and 4-3 compare predictions of ignition-delay times obtained using the skeletal mechanism with the corresponding values of shock-tube experiments [75-81] for n-heptane, n-decane and n-dodecane. The symbols represent experimental data points and the lines represent the predictions obtained using the skeletal mechanism. The experimental data and the predictions agree well for the investigated pressure and temperature range. This confirms the validity of the reduced mechanism.

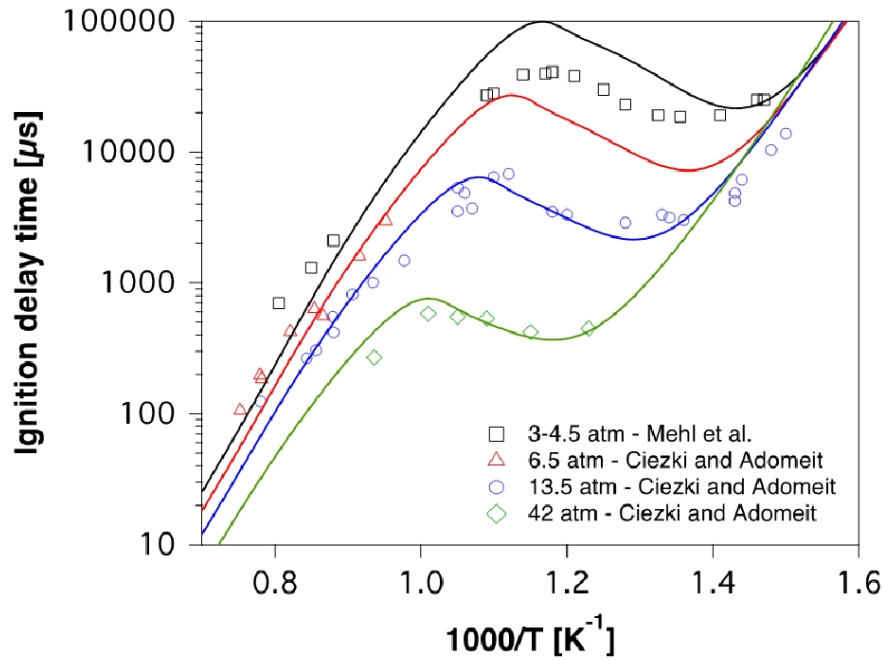


Figure 4-1: Comparison of ignition-delay time predictions to experimental data for n-heptane.



#### 4. Numerical Computations

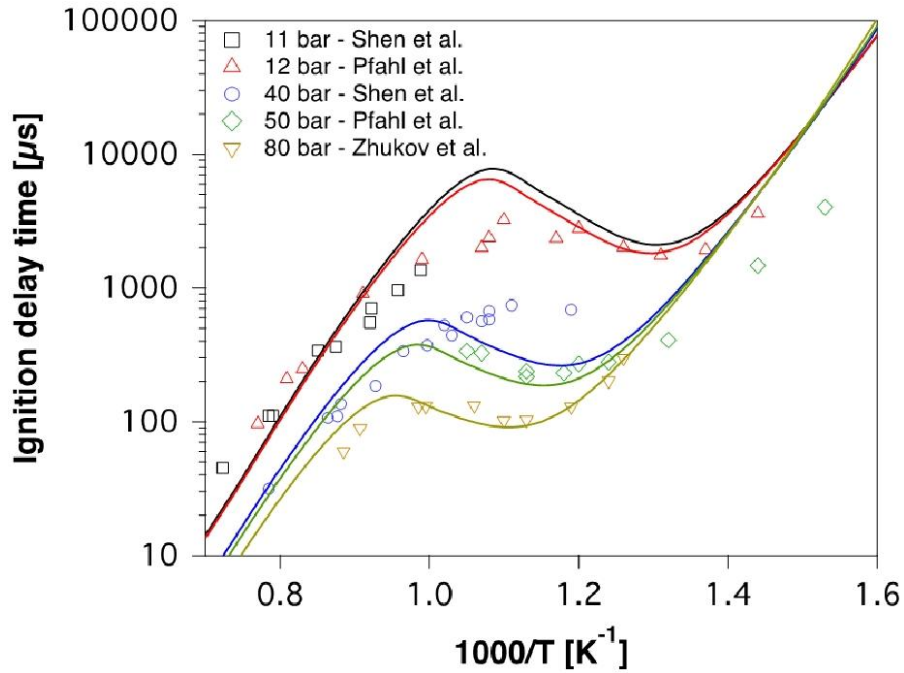


Figure 4-2: Comparison of ignition-delay time predictions to experimental data for n-decane.

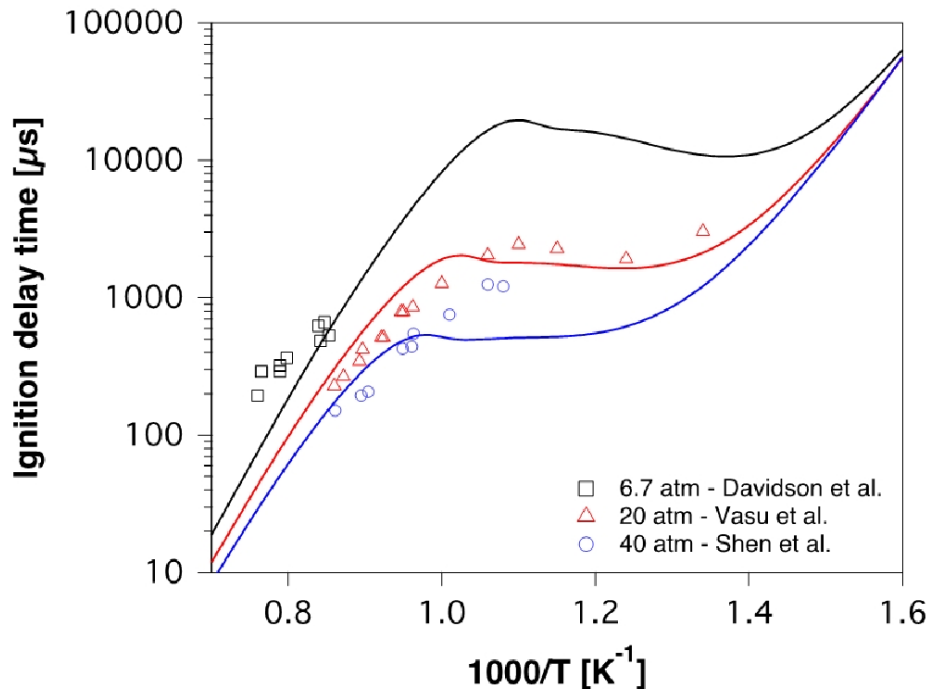


Figure 4-3: Comparison of ignition-delay time predictions to experimental data for n-dodecane.

The kinetic modelling for the three jet fuel surrogates is carried out using a skeletal mechanism made up of kinetic steps of the POLIMI detailed kinetic mechanism [73], which describes partial

#### 4. Numerical Computations

oxidation, pyrolysis and combustion of kerosene and aviation fuels. This skeletal mechanism consists of 231 species and has been employed to predict combustion of several proposed kerosene surrogate mixtures. Kerosene surrogates typically include n-alkanes, iso-alkanes, methylcyclohexane, aromatics (from toluene up to C<sub>9</sub> aromatics), decalin and tetralin. The kinetic steps for these hydrocarbons are included in the kinetic mechanism and have been verified [20]. Kinetic steps of methylcyclohexane have been updated [82] considering recent experimental studies of ignition delay times in rapid compression machines at high pressure and low intermediate temperature [83].

The computations are performed using the OpenSMOKE+ + code [84]. The structure of the reactive flow-field is calculated by solving the unsteady conservation equation of mass, momentum, energy and species balance equation [85,86]. Boundary conditions are applied at the exit of the oxidizer duct and the gas side of the liquid-gas interface. At the oxidizer boundary the oxidizer stream velocity  $V_2$  and the mass flux is specified. The radial component of the oxidizer velocity at the oxidizer boundary is presumed to be equal to zero. At the liquid-gas interface mixed boundary conditions are applied for the species balance equations and the energy conservation equation [24]. The temperature at the liquid-gas interface is obtained using Raoult's Law [87]. The heat of vaporization and vapor pressure for these fuels are calculated using empirical coefficients [88]. Numerical computations are performed for pressures between 3 and 6 bar with an oxygen mass fraction  $Y_{O_2} = 0.15$  and a constant oxidizer strain rate of  $a_2 = 138 \text{ s}^{-1}$ . The temperature of the oxidizer stream is increased in increments of 10 K/s until autoignition occurs and a hot flame is established. The point of autoignition,  $T_2 = T_{ig}$ , is defined when an abrupt transition from a weakly reactive region to a flame takes place. More details on the carried out numerical simulations can be found elsewhere [68].

## 4.2 FACE Fuels

Numerical simulations are carried out in collaboration with the Combustion and Pyrolysis (CPC) group at the King Abdullah University of Science and Technology in Saudi Arabia. For the simu-

#### 4. Numerical Computations

lations a reduced version of the FACE gasoline surrogates model by Sarathy *et al.* [36] with 343 species is employed. The mechanism is reduced using the direct relation graph with expert knowledge method (DRG-X) [82]. The DRG-X method assumes that some species during the combustion process are not strongly coupled to others, so they can be removed without influencing the model. The mechanism is reduced by specifying a certain error tolerance for heat release for every surrogate component.

Ignition simulations are carried out using the OPPDIF solver in CHEMKIN PRO. For autoignition simulation a temperature profile is first established with cold mixtures at both fuel and oxidizer side. Then the temperature of the oxidizer stream is gradually increased until autoignition occurs. The temperature of the fuel stream and composition of the reactant streams is kept constant throughout the simulation. The simulations are performed considering thermal diffusion (Soret effect), mixture average transport and convergence parameters of GRAD and CURV = 0.1. For extinction simulations the extinction solver in CHEMKIN PRO is employed. The solver employs the arc length continuation method to generate the S-curve. First, a stable flame is established for conditions close to extinction using the OPPDIF code. These conditions are employed in the extinction solver. A 2-point extinction method with 1000 steps is employed and convergence parameters of GRAD and CURV = 0.2 are used to limit the maximum gradients and curvatures between grid and points. Table 4-1 shows the compositions for the multi-component FACE fuel surrogate blends used for the numerical simulations.

	FACE A	FACE C	FACE G	FACE F	FACE I
2-Methyl butane	12	5	9.5	9.8	10
2-Methyl hexane	10.3	4.7	9.8	7	28
Cyclopentane	0	0	15.3	15.8	0
1,2,4-Trimethylbenzene	0	0	21.1	8.4	0
1-Hexene	0	0	8.1	8.4	0
2,2,4-Trimethylpentane	60	54.6	18	43.7	35
Toluene	0	4.8	10.6	0	4
n-Butane	7.7	18.4	7.6	6.9	0
n-Heptane	10	12.5	0	0	12
Cyclohexane	0	0	0	0	5

Table 4-1: Surrogate blend compositions in mole percentage [36].

### 4.3 Dimethyl Ether

A computational study is carried out in collaboration with colleagues from the Indian Institute of Technology Madras. The mechanism employed is the San Diego mechanism [90], which has recently been updated to include the chemical kinetics of oxidation of dimethyl ether [91]. The computations are conducted using the FlameMaster software version 3.3.10 [92]. At the boundaries, the mass fluxes of fuel and oxidizer are specified with the same values used in the experiments. Plug-flow boundary conditions are applied. A stable flame is established at low values for the injection velocities  $V_1$  and  $V_2$  for fuel and oxidizer, which are then gradually increased until extinction occurs. A momentum balance between fuel and oxidizer stream is maintained to keep the stagnation plane approximately equidistant to the boundaries.

## 5 Results and Discussion

### 5.1 Jet Fuels and Surrogates

Experiments are carried out to elucidate the autoignition characteristics of high molecular weight hydrocarbon fuels at elevated pressures for three different types of hydrocarbon fuels, pure straight chained alkanes, jet fuels and jet fuel surrogates. All experiments are conducted at pressures of 3, 4, 5 and 6 bar, oxidizer oxygen mass fractions of  $Y_{O_2} = 0,15$  and oxidizer strain rate of  $a_2 = 138 \text{ s}^{-1}$ . The chosen oxidizer oxygen mass fraction is a compromise between soot formation and autoignition temperature. A lower oxidizer oxygen mass fraction reduces soot formation and therefore prevents clogging of the suction system of the experimental apparatus. A lower oxygen mass fraction of the oxidizer stream also means higher autoignition temperatures. The chosen oxidizer oxygen mass fraction  $Y_{O_2}$  provides a good compromise between soot formation and achievable autoignition temperatures. A lower oxidizer oxygen mass fraction also decreases the risk of an explosion due to accumulation of oxygen and gaseous fuel inside the pressure chamber.

#### 5.1.1 Pure Fuels

Figure 5-1 shows the experimental results for the three pure hydrocarbons n-heptane, n-decane and n-dodecane compared with the carried out numerical computations. The oxidizer temperature at autoignition  $T_{ig}$  is shown as a function of the chamber pressure  $p$ . The computational results also include a prediction made for n-heptane carried out employing the San Diego mechanism.

The experimental and computational results show a decrease of autoignition temperature  $T_{ig}$  in the range of 150 to 200 K for an increase in pressure  $p$  from 3 to 6 bar. This is observed for all

three of the considered fuels. For a given chamber pressure  $p$ , the autoignition temperature  $T_{ig}$  for n-dodecane is the lowest followed by n-decane and n-heptane. This result is consistent with the result of the carried out computational investigation which indicates that the influence of low-temperature chemistry increases with increasing pressure and that of Grana *et al.* [23], who observed a similar order of reactivities for these fuels at atmospheric pressure and air as the oxidizer. Figure 5-1 shows that the results of the experimental investigations agree well with the predictions of the numerical computations. The red line shows predictions for n-heptane when low-temperature chemistry is not considered from the mechanism. This temperature difference is a quantitative measure for the influence of low-temperature chemistry on critical conditions of autoignition of n-heptane. Similar behavior can be expected for the other fuels.

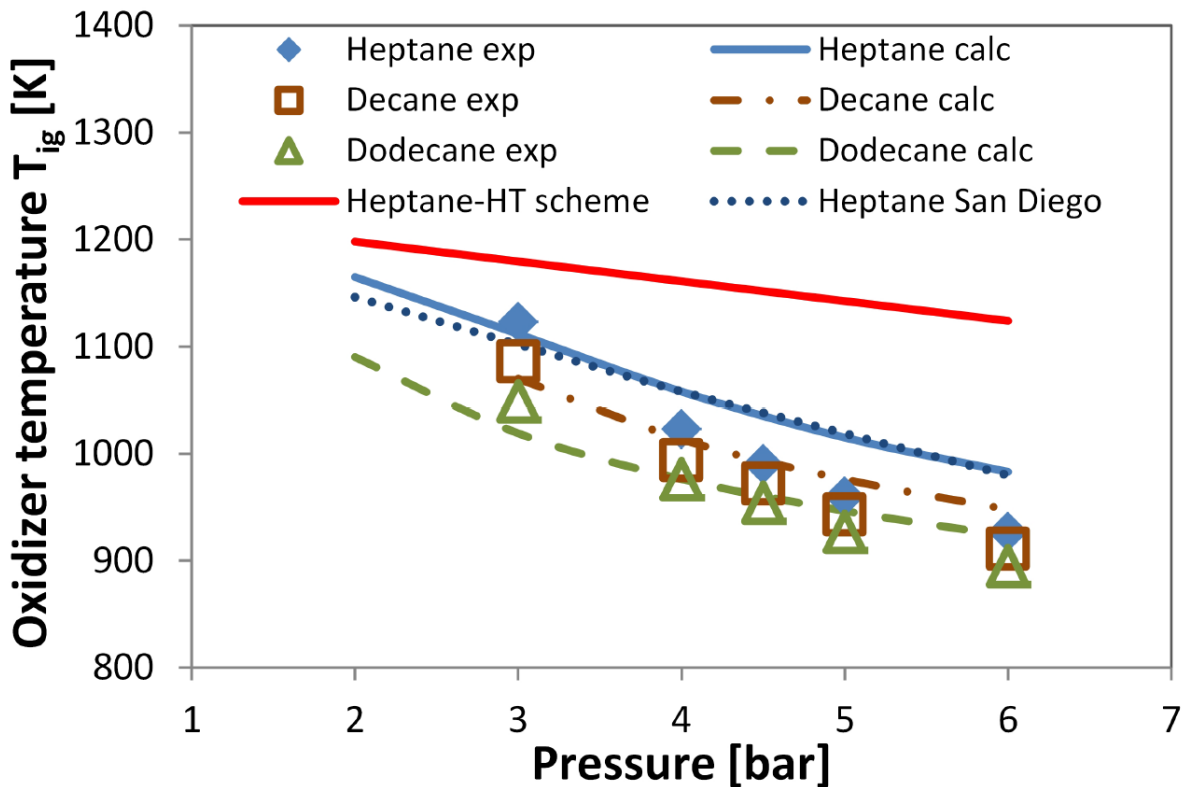


Figure 5-1: Comparison of experimental results and simulations for the three pure fuels.

Figure 5-2 shows the temperature increment  $\Delta T$  and the temperature at the liquid gas interface  $T_s$  as a function of  $T_2$  for n-heptane and n-dodecane. The quantity  $\Delta T$  describes the temperature difference between the maximum temperature in the mixing layer and the oxidizer tempera-

ture  $T_2$ . For both fuels a weakly reactive region around 700 K can be observed which is marked by a temperature increase between 50 and 100 K. By further increasing  $T_2$ , the temperature

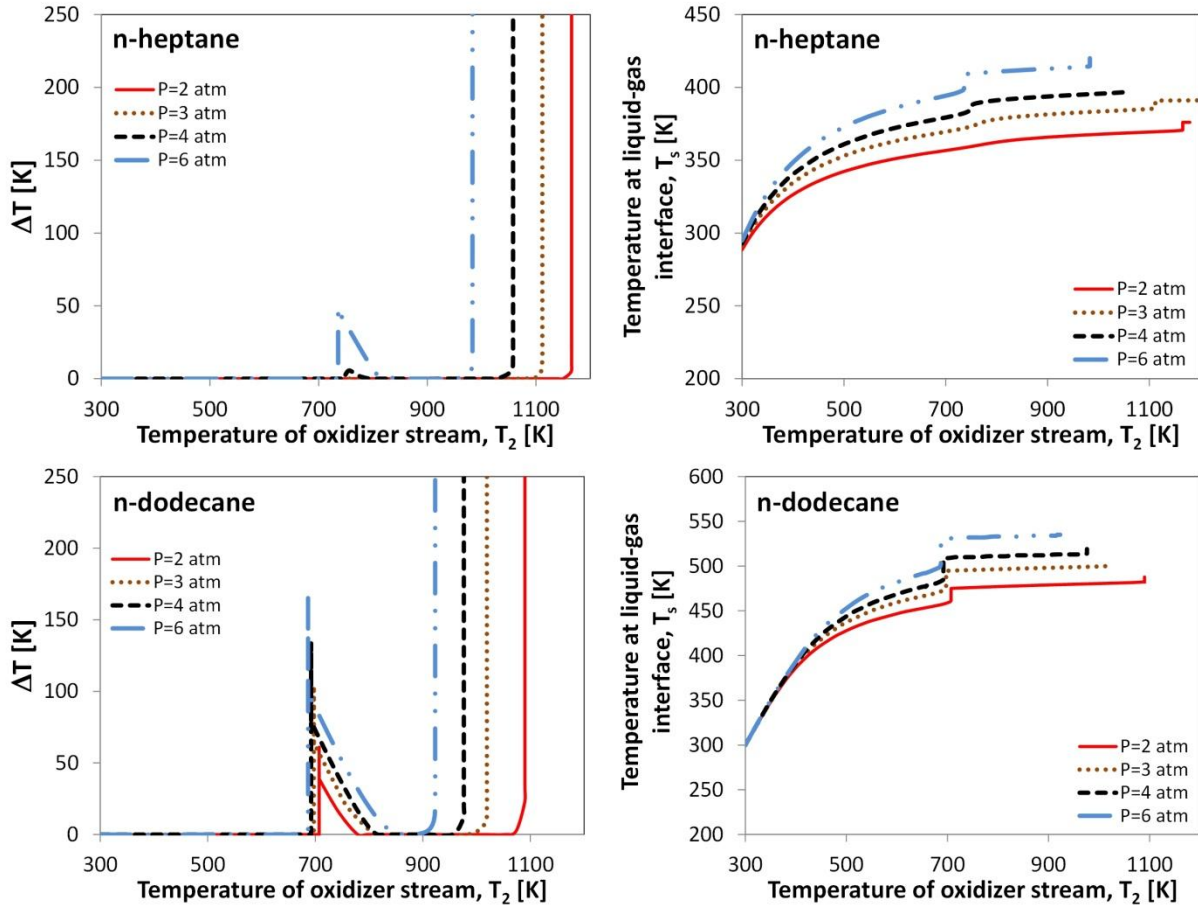


Figure 5-2:  $\Delta T$  and  $T_s$  as a function of  $T_2$  for n-heptane and n-dodecane.

then decreases again, followed by a rapid rise in temperature, referred to as hot-ignition. This behavior is indicative of low-temperature chemistry and two-stage ignition. The computations show that the temperature difference  $\Delta T$  increases with increasing pressure and therefore reduces the autoignition temperature  $T_{ig}$  with increasing pressure. The computational results clearly show the existence of a negative temperature coefficient (NTC) region between the first weakly reactive region around 700 K and the rapid rise of  $\Delta T$ . The negative temperature coefficient regime is a unique phenomenon in combustion of hydrocarbons. It describes the phenomenon where the global rate of the reaction decreases with increasing temperature. The low-temperature chemistry in the POLIMI mechanism has been recently revised and analyzed in

detail for alkanes [73, 93-95] and provides reliable predictions of ignition delay times. Figure 5-2 also shows an increase of the temperature at the liquid-gas interface  $T_s$  with an increase in pressure due to a rise in partial pressure. For a given  $T_2$ , the surface temperature of a pool of n-dodecane is higher than the surface temperature of a pool of n-heptane. For a given pressure and temperature, more n-heptane is evaporating than n-dodecane because n-heptane has a higher vapor pressure. The higher evaporation temperature of n-dodecane has a significant impact on lowering the autoignition temperature in comparison to n-heptane for a given  $p$  and  $T_2$ . Previous experimental and computational studies on autoignition of n-heptane, n-decane and n-dodecane in a counterflow configuration and isolated fuel droplets have observed cool flames, NTC behavior and two-stage ignition [96,97]. The detailed results are listed in Appendix B.

### 5.1.2 Jet Fuels and Surrogates

Figure 5-3 shows the experimental results for the three jet fuels JP-8, JP-5 and Jet A compared with the three jet fuel surrogates Aachen Surrogate, Princeton Surrogate and Surrogate C. For a given chamber pressure  $p$ , the autoignition temperature  $T_{ig}$  for JP-8 is the lowest of the jet fuels followed by JP-5 and Jet A. The only deviation from this trend is observed at 6 bar, where the measured autoignition temperature for JP-5 is higher than the one from Jet A. The measured autoignition temperatures for the three jet fuels are closely grouped together which was to be expected, since the two military grade jet fuels JP-5 and JP-8 are similar to the commercial aviation fuel Jet A. For an increase in chamber pressure  $p$ , the autoignition temperatures  $T_{ig}$  of the three jet fuels are increasingly deviating. The experimental results also show a decrease of autoignition temperature  $T_{ig}$  in the range of 150 to 200 K, for an increase in pressure  $p$  from 3 to 6 bar.

For a given chamber pressure  $p$ , the autoignition temperature  $T_{ig}$  for the Princeton surrogate is the highest of the three surrogates followed by the Surrogate C and the Aachen Surrogate. The obtained autoignition temperatures for the Aachen Surrogate are consistently 30 to 40 K lower



than the autoignition temperatures of JP-8. This surrogate reproduces the autoignition trend of a jet fuel very well across the evaluated pressure range but, compared to the other tested surrogates, shows a bigger deviation at 3 bar. The Princeton Surrogate shows good agreement for the autoignition temperature at 3 bar compared with the three tested jet fuels but also shows a growing deviation with rising pressure. The measured autoignition temperatures for the Princeton Surrogate are higher across the entire pressure range. Surrogate C reproduces autoignition characteristics of jet fuels best compared to the other tested surrogates. At 3 bar, the measured autoignition temperature is only 2 K higher than the autoignition temperature of Jet A and 11 K higher than the autoignition temperature of JP-8.

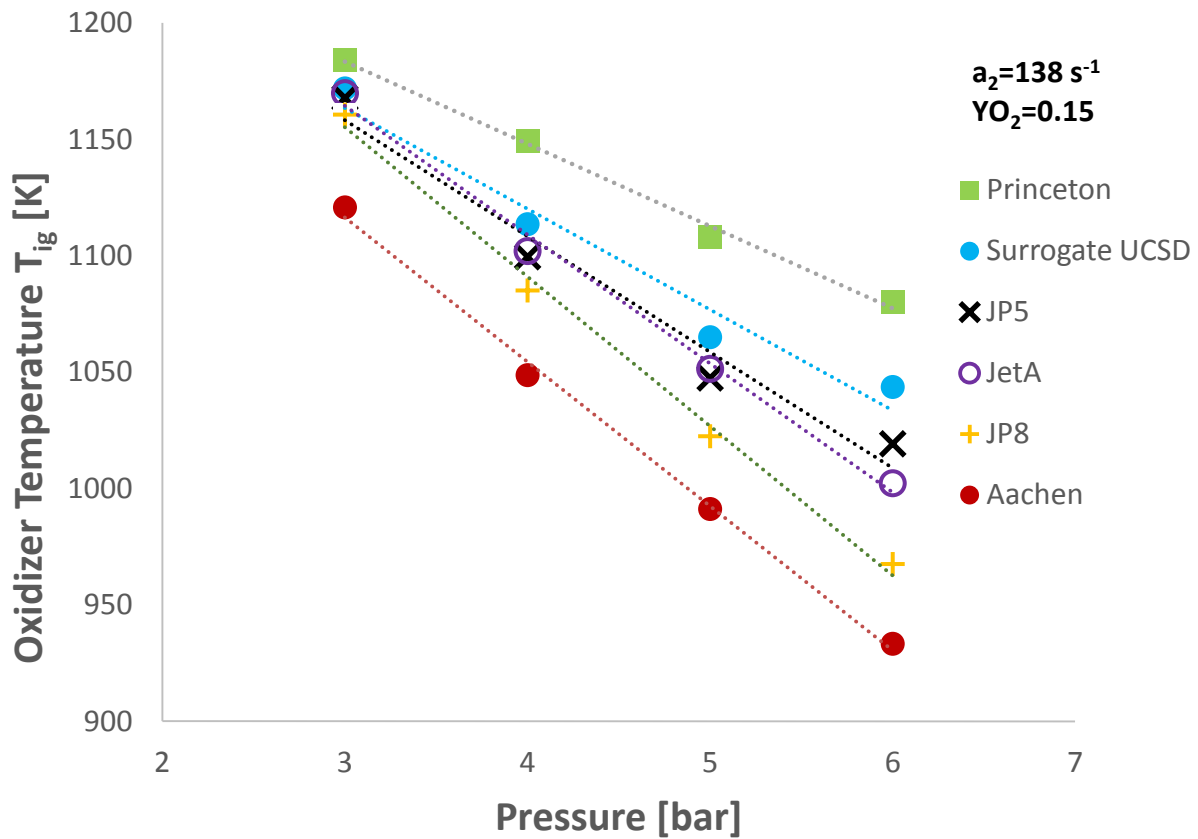


Figure 5-3: Experimental results of autoignition experiments for jet fuels and surrogates.

Figure 5-4 shows the values for the temperature increment  $\Delta T$  and temperature at the liquid gas interface  $T_s$  as a function of the oxidizer temperature  $T_2$ . The Aachen Surrogate shows a weakly reactive region around 700 K of oxidizer duct temperature. By further increasing  $T_2$ , the

temperature difference decreases until  $\Delta T$  rapidly increases around 950 K. The temperature rise in the weakly reactive region is an indicator for low-temperature chemistry followed by a temperature decrease, known as the NTC-region. At last, hot-ignition occurs marked by a large increase in  $\Delta T$ . Figure 5-4 also shows an increase of  $T_s$  with increasing  $T_2$ . The values for  $T_s$  are less than their respective normal boiling points for the given conditions. The boiling points for the Aachen Surrogate, Surrogate C and Princeton Surrogate at a pressure of 1 bar are 446 K, 411 K and 411 K respectively and at a pressure of 6 bar are 532 K, 501 K and 502 K.

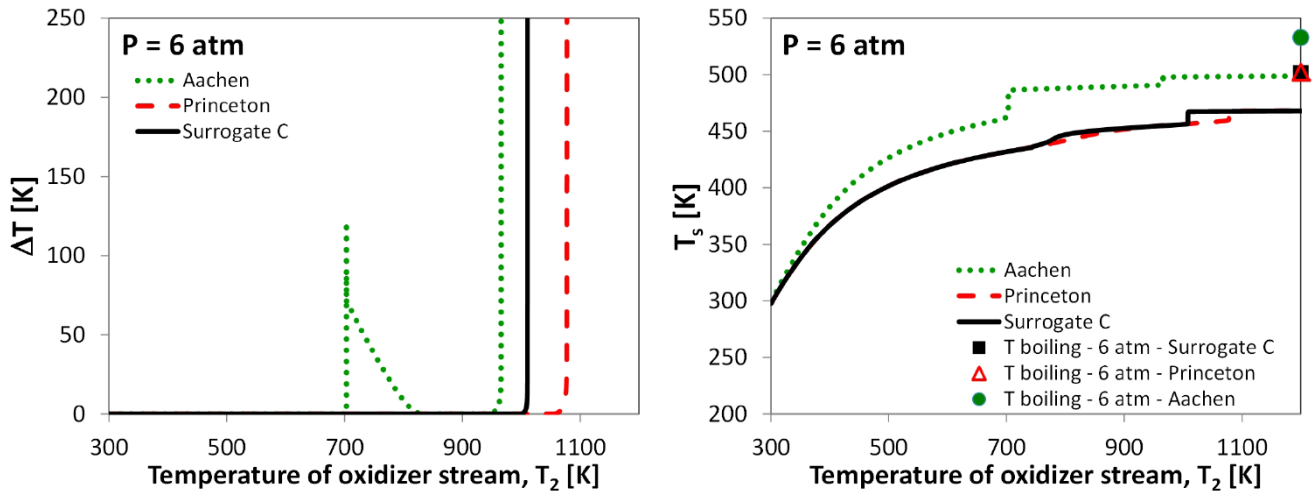


Figure 5-4:  $\Delta T$  and  $T_s$  as a function of  $T_2$  for the jet fuel surrogates.

Figure 5-5 shows the mole fractions for hydrogen peroxide ( $H_2O_2$ ),  $X_{H_2O_2}$  and keto hydroperoxide ( $KET$ ),  $X_{KET}$ . It can be observed that for all surrogates  $H_2O_2$  and  $KET$  are formed at the onset of low-temperature ignition. At the onset of hot-ignition their concentrations become negligible. Therefore, hot-ignition is preceded by low-temperature ignition. Computations are also carried out for Surrogate C with the kinetic steps characterizing low-temperature chemistry for methylcyclohexane removed. The computations show that as a result very little  $H_2O_2$  is formed. This indicates that low-temperature ignition for Surrogate C is caused by methylcyclohexane. The computations show that the exothermic reaction zone, which leads to autoignition is located on the oxidizer side of the stagnation plane. The fuel diffuses through the stagnation plane and  $H_2O_2$ , peroxides and keto-hydroperoxides are formed in a region where low-temperature reactions take place. These species diffuse further upstream towards the oxidizer boundary where they promote hot-ignition.

## 5. Results and Discussion

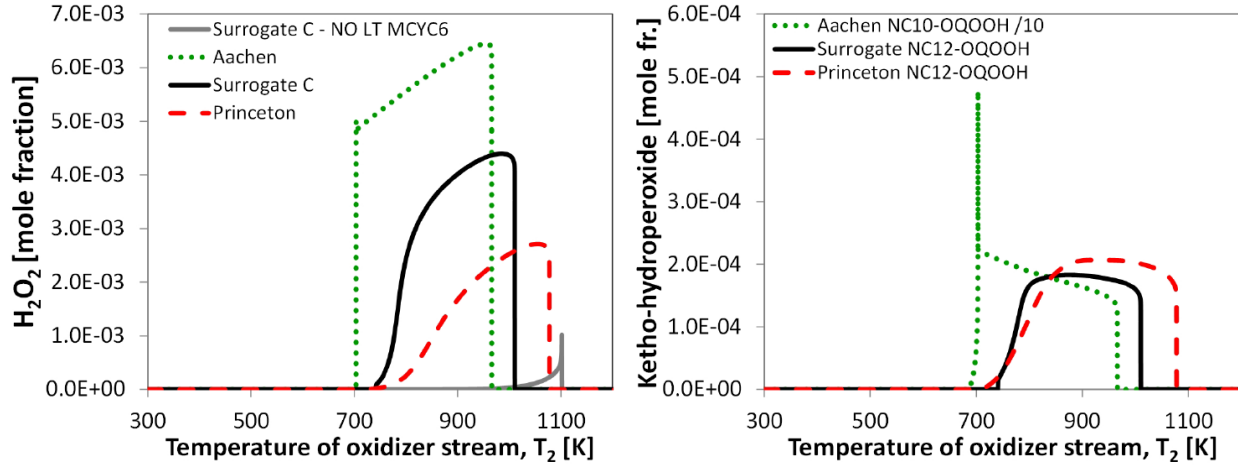


Figure 5-5: Mole-fractions of  $H_2O_2$  and  $KET$  as a function of  $T_2$ .

Figure 5-6 shows a comparison of the experimental and computational results for the three tested jet fuel surrogates. For a given chamber pressure  $p$ , the Princeton Surrogate has the highest autoignition temperature  $T_{ig}$  followed by the Surrogate C and the Aachen Surrogate. The agreement between the experimental and computational results is very good. The order of reactivity of the fuels can be explained by considering the volatility and the low-temperature reactivity of the surrogate components. Previous studies have shown that autoignition of high molecular weight hydrocarbon fuels is influenced by low-temperature chemistry at low strain rates and molecular transport for higher strain rates [24]. The influence of low-temperature chemistry increases with increasing pressure. The present study is carried out at relatively low strain rates, therefore autoignition can be expected to be influenced by low-temperature chemistry. The Aachen Surrogate has the lowest autoignition temperatures observed because the value of  $T_s$  is the highest of the surrogates tested. Therefore, large amounts of n-decane, which is known to have a significant low-temperature reactivity, evaporate and lead to ignition. Surrogate C and the Princeton Surrogate have similar volatilities but the constituents have different low-temperature reactivities. The lower reactivity of the Princeton Surrogate is due to 2,2,4-trimethylpentane (instead of methylcyclohexane) and larger amount of aromatics. Figure 5-6 also shows a prediction for Surrogate C with reactions that characterize low-temperature chemistry of methylcyclohexane removed. It can be observed, that autoignition temperatures are significantly higher compared to autoignition temperatures with low-temperatures reactivi-

ty of methycyclohexane considered. With increasing pressure  $p$ , the difference between predicted values of  $T_{ig}$  with and without low-temperature chemistry increases. This indicates the influence of low-temperature reactivity of methycyclohexane on autoignition.

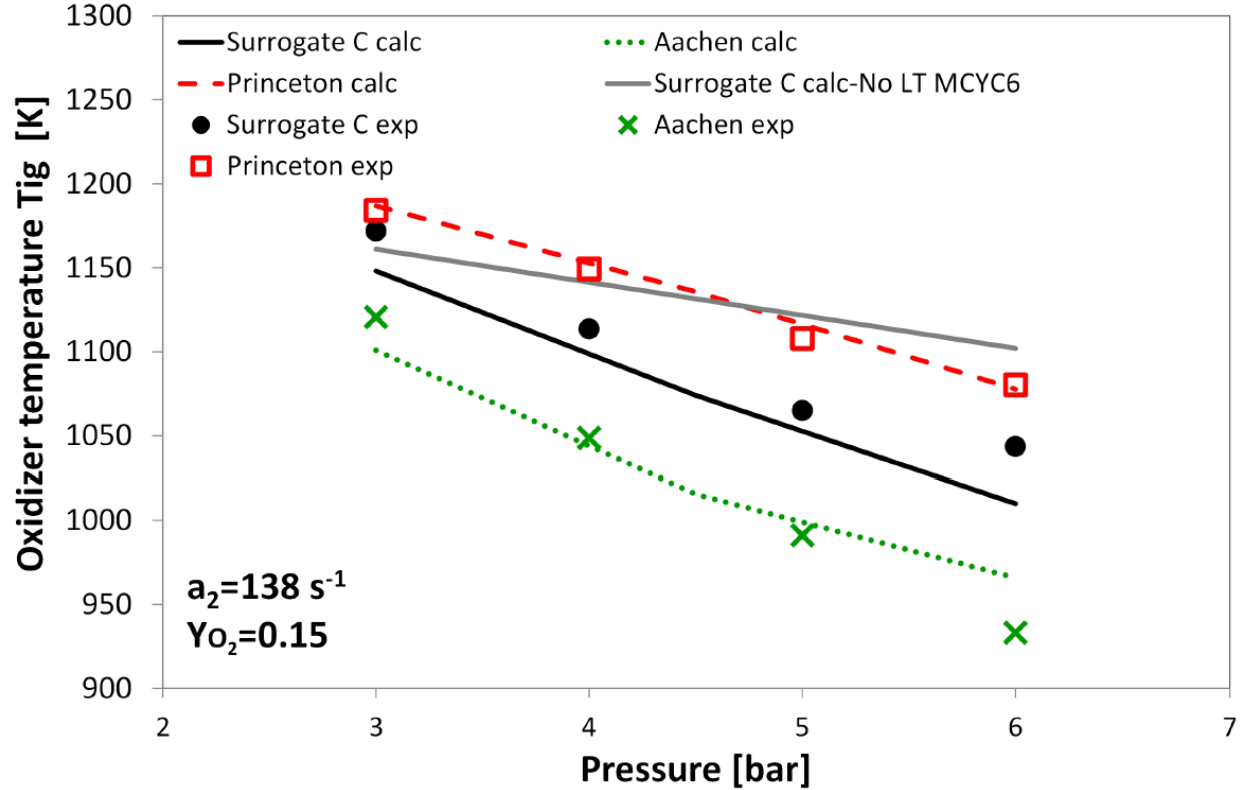


Figure 5-6: Experimental and computational results for the jet fuel surrogates.

The conducted experimental and computational investigations described here show that low-temperature chemistry plays a dominant role in promoting autoignition of the condensed hydrocarbon fuels tested here. Due to limitations in the experimental setup, the investigation was limited to low values of the oxidizer strain rate  $a_2$  and low oxidizer oxygen mass fraction  $Y_{O_2}$ . It has been observed, that the physical properties and specifically vapor pressure influence the autoignition temperatures. For future experiments, it would be of interest to measure the influence of low-temperature chemistry on critical conditions of autoignition at higher values of oxidizer strain rate and higher values of oxidizer oxygen mass fraction. The maximum chamber pressure for this experiment was 6 bar. It would be of interest to carry out experiments on critical conditions of autoignition at higher pressures. The detailed results are listed in Appendix B.

## 5.2 FACE Fuels

Figure 5-7 shows the obtained experimental data of the strain rate at extinction  $a_2$  as a function of the fuel mass fraction  $Y_{F,1}$ . The results show that the extinction strain rates  $a_2$  increase with an increase in fuel mass fraction  $Y_{F,1}$  and that all of the fuels are closely grouped together except for FACE I, which extinguishes about 10 to 15  $\text{s}^{-1}$  above the other tested fuels. A clear order in terms of extinction behavior across the tested range for all of the FACE gasoline fuels cannot be observed since there are some overlaps in the obtained experimental data. The detailed results are listed in Appendix C.

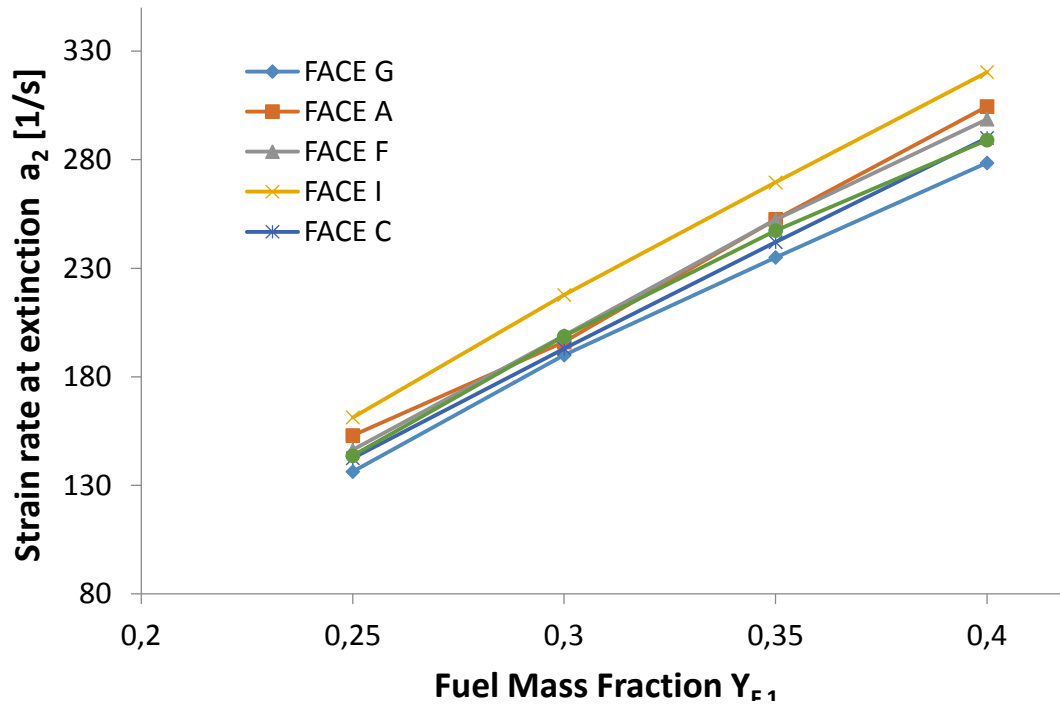


Figure 5-7: Experimental results of the extinction experiments for all FACE gasoline fuels.

Table 5-8 shows a comparison between the carried out numerical simulations and the experimental data for the critical limits at extinction for every FACE gasoline fuel.

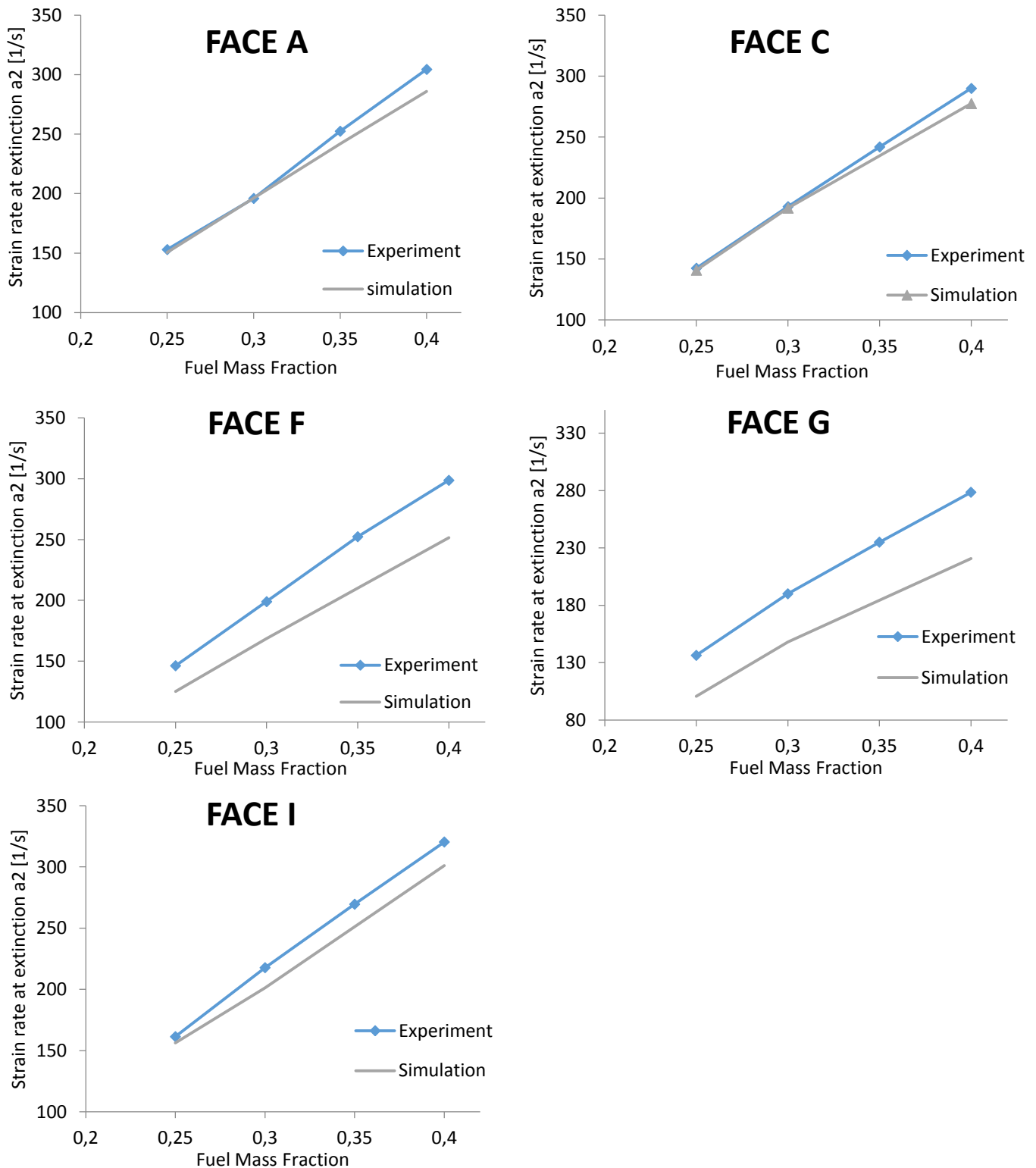


Figure 5-8: Experimental data vs. numerical simulations for extinction experiments.

The results show that the agreement between the numerical simulations and the experimental data is very good for FACE A and FACE C while the simulations for FACE F, FACE I and FACE G predict lower extinction strain rates than the experimental measurements.

Figure 5-9 shows the results of the carried out autoignition experiments with the oxidizer temperature at autoignition  $T_{ig}$  as a function of the oxidizer strain rate  $a_2$ . The results show an increase in autoignition temperature  $T_{ig}$  with an increase in oxidizer strain rate  $a_2$ .

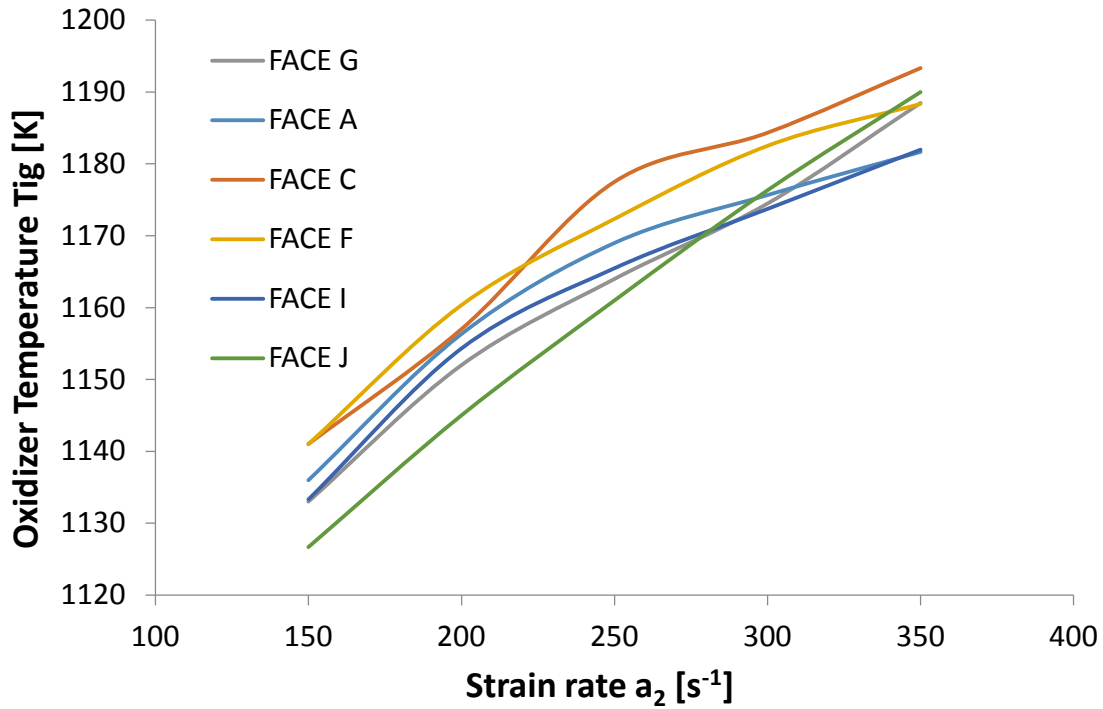


Figure 5-9: Experimental results of the autoignition experiments for all the FACE gasoline fuels.

Figure 5-10 shows a comparison between the carried out numerical simulations and the experimental data for the critical limits at autoignition for every FACE gasoline fuel. The results show that the agreement between the numerical simulations and the experimental data is good for all fuels tested. The detailed results are listed in Appendix C.

## 5. Results and Discussion

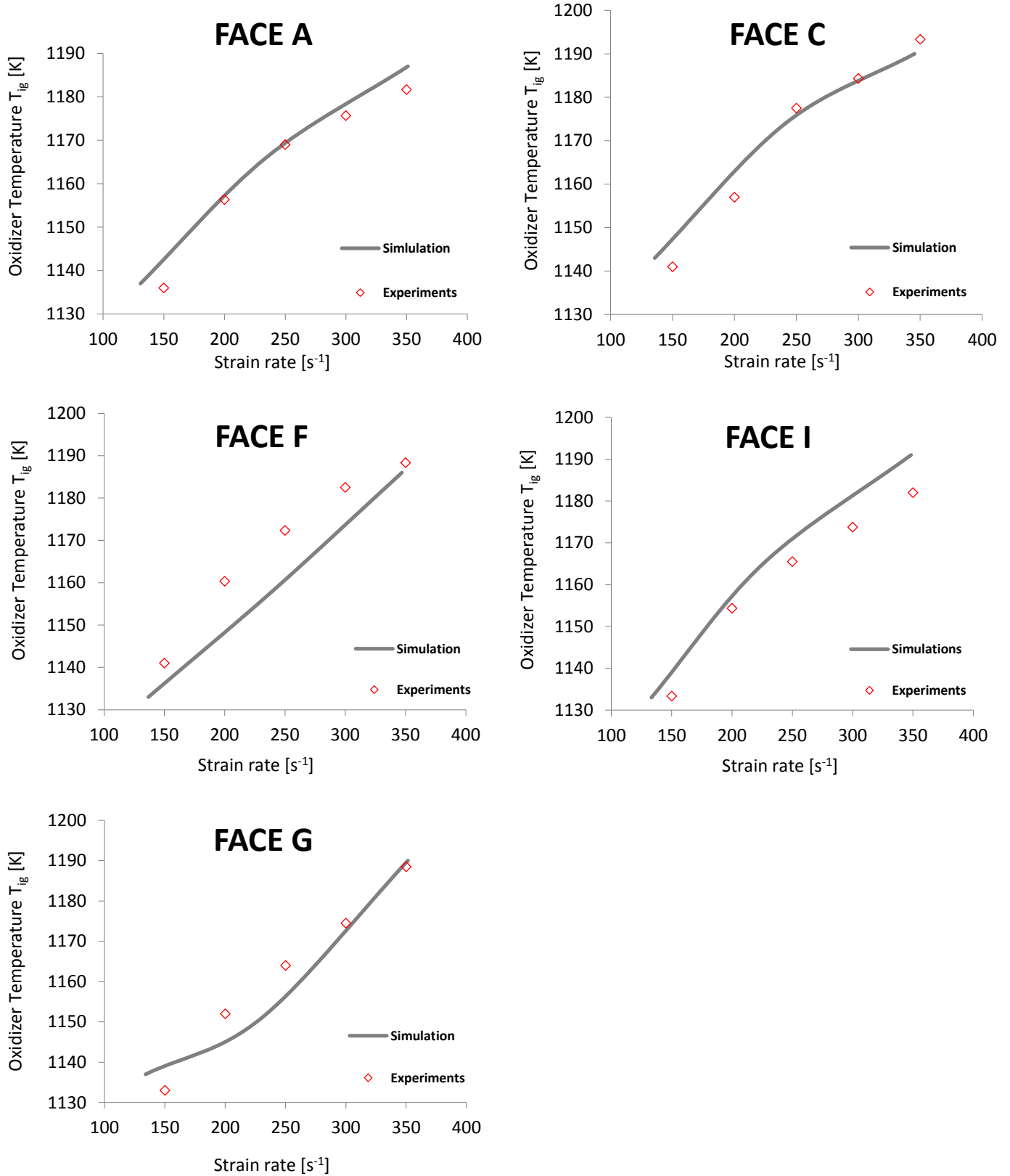


Figure 5-10: Experimental data vs. numerical simulations for autoignition experiments.



### 5.3 Dimethyl Ether

Figure 5-11 shows the experimental results for the strain rate at extinction  $a_2$  as a function of the stoichiometric mixture fraction  $\xi_{st}$  for several adiabatic flame temperatures. The blue line represents experimental data of experiments carried out for an adiabatic flame temperature  $T_{st} = 2000$  K. Starting out from the lowest stoichiometric mixture fraction, the extinction strain rate first decreases with an increase in stoichiometric mixture fraction  $\xi_{st}$  and then strongly increases. The same tendency can be observed for measurements taken at different adiabatic flame temperatures  $T_{st}$ . Due to a lack of available DME, measurements taken at  $T_{st} = 1950$  K, 1975 K, 2025 K and 2050 K are limited to only three measurements for different stoichiometric mixture fractions. The results show that the strain rate at extinction  $a_2$  increases with an increase in adiabatic flame temperature  $T_{st}$ .

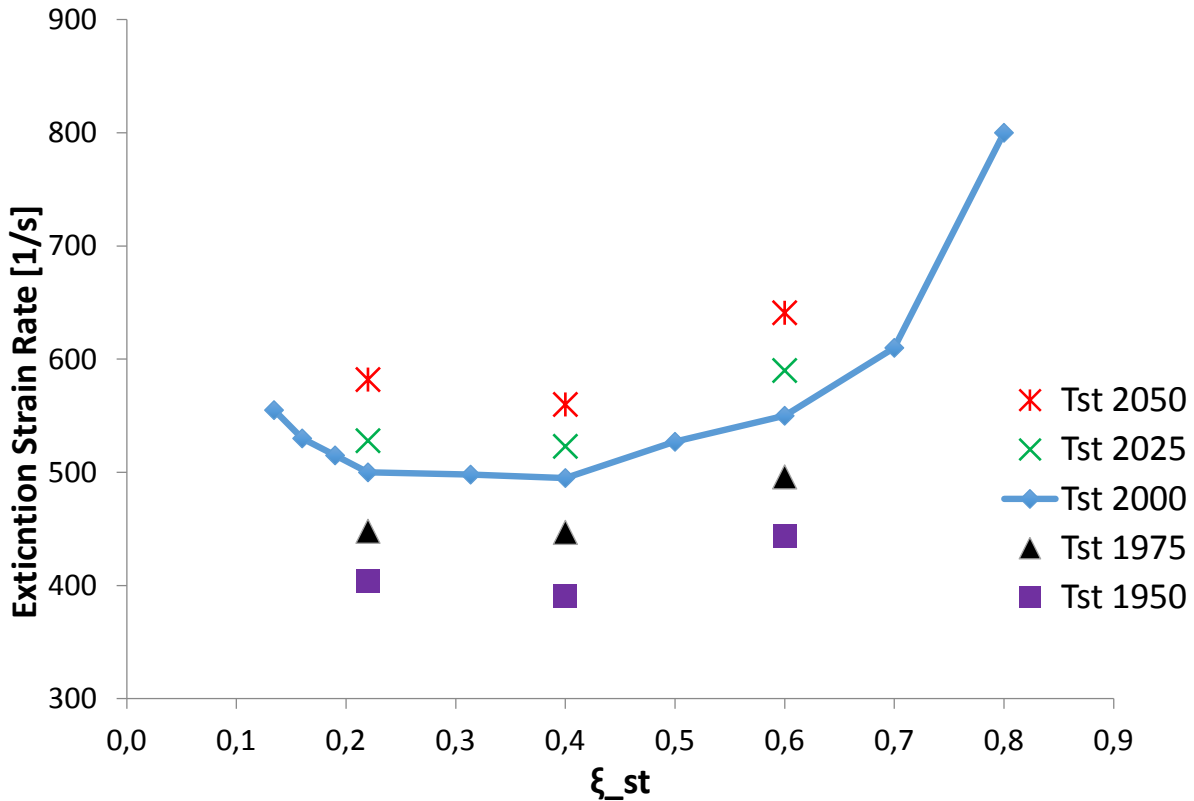


Figure 5-11: Experimental results for DME extinction experiments at different adiabatic flame temperatures.

Figure 5-12 compares experimental results of critical conditions at extinction for  $T_{st} = 2000$  K with predictions obtained using different kinetic mechanisms [43, 90, 98]. The predictions carried out using the San Diego mechanism [90] and that of Zhao et. al. [98] show good agreement with the experimental data for values of  $\xi_{st}$  less than 0.4 but significant deviations for higher values of  $\xi_{st}$ . Previous experimental studies by Song et. al [99] and Hashimoto et. al. [100] also show that the strain rate at extinction first decreases and then increases with an increase in  $\xi_{st}$ . Combustion of DME is influenced by low-temperature chemistry [101-105]. In order to eluci-

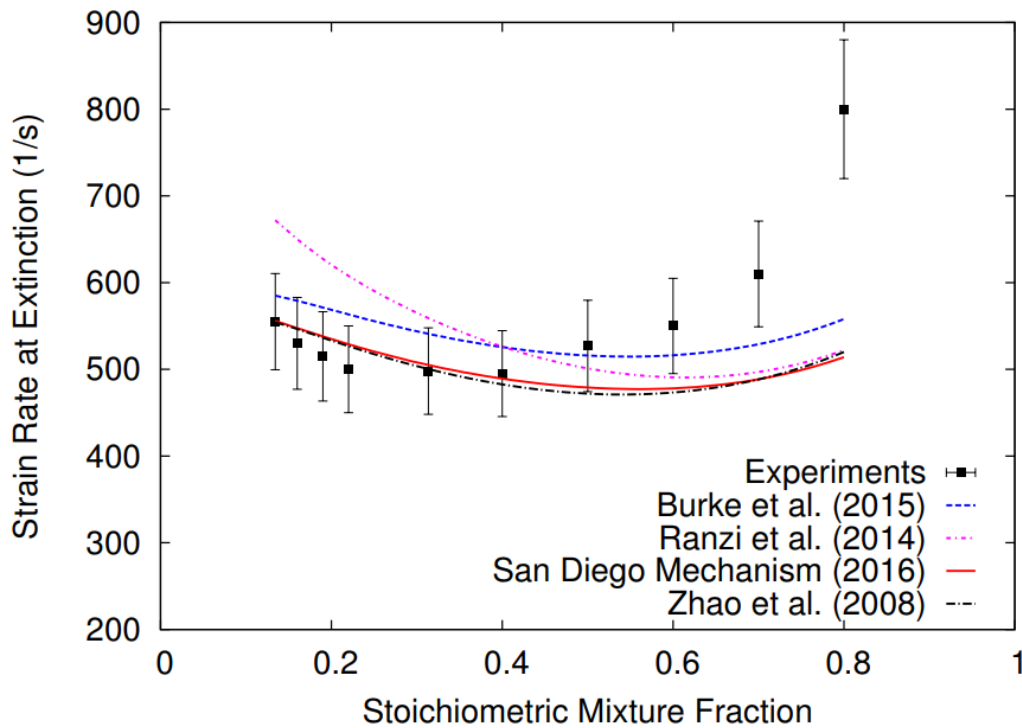


Figure 5-12: Comparison of experimental results and predictions with various mechanisms.

date the influence of low-temperature chemistry on critical conditions at extinction of DME, computations are carried out employing the San Diego mechanism [90] without kinetic steps which characterize low-temperature chemistry. Figure 5-13 shows the predictions with and without the influence of low-temperature chemistry compared to the experimental results. The results show no influence of low-temperature chemistry on critical conditions at extinction. Therefore the differences between the predictions and experimental results cannot be attributed to the kinetic description of low-temperature chemistry in the mechanism.

## 5. Results and Discussion

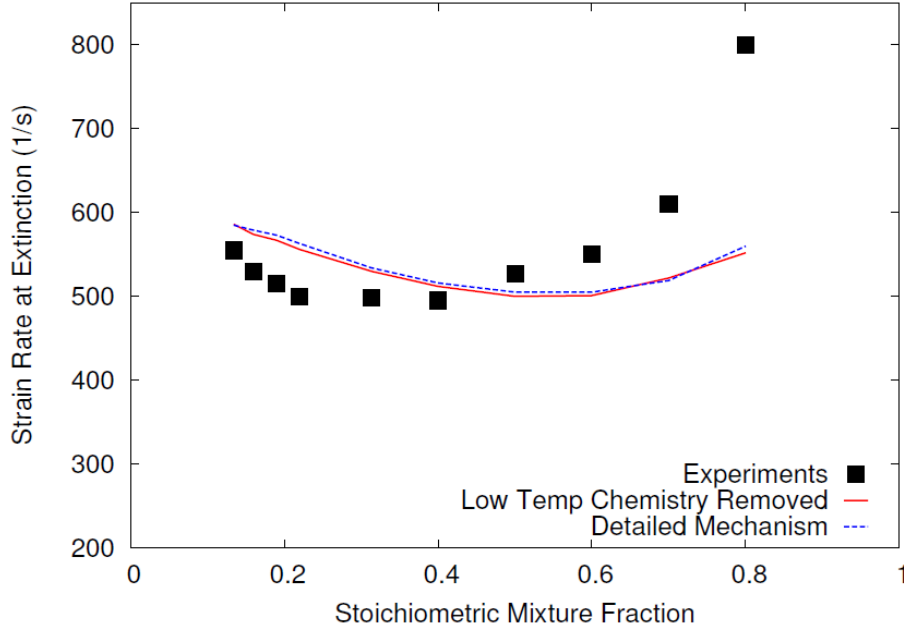


Figure 5-13: Comparison of experimental results with predictions of the San Diego mechanism with and without low-temperature chemistry.

Figure 5-14 compares predicted values of the scalar dissipation rate  $\chi_{st}$  using the San Diego mechanism with values obtained from measurements. The scalar dissipation rate considers the influence of diffusion and convection normal to the surface of stoichiometric mixture [106]. A relation between extinction strain rate  $a_q$  and  $\chi_{st,q}$  has been derived by Kim and Williams [107]

$$\chi_{st,q} = \frac{a_q}{2\pi} \frac{3[(T_{st}/T_u)^{1/2} + 1]^2}{2(T_{st}/T_u)^{1/2} + 1} \exp\{-2[erfc^{-1}(2\xi_{st})]^2\} \quad (34)$$

In this equation  $erfc^{-1}$  refers to the inverse of the complementary error function. Equation (34) is used to calculate  $\chi_{st,q}$  from calculated and measured values of  $a_q$ . For values of  $\xi_{st} > 0.5$ ,  $\chi_{st,q}$  is calculated by replacing  $\xi_{st}$  with  $(1 - \xi_{st})$  in equation (34). Both, the predictions and experimental measurements show an increase of  $\chi_{st,q}$  with  $\xi_{st}$  increasing until it reaches a maximum around  $\xi_{st} = 0.5$  and then decreases. The experimental measurements and predictions show good agreement up to  $\xi_{st} = 0.4$  and a rising deviation above.

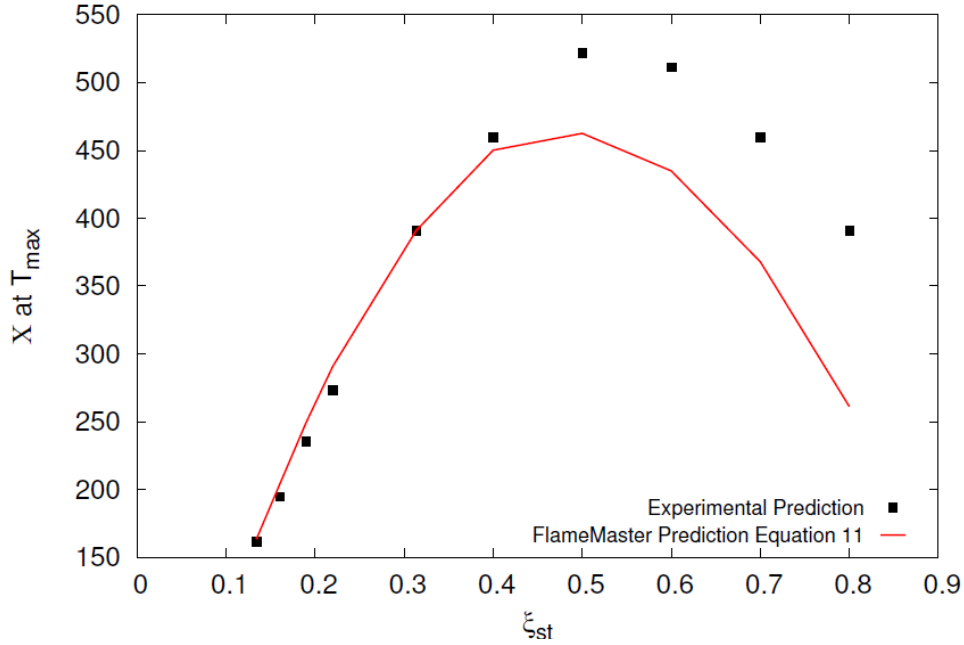


Figure 5-14: The scalar dissipation rate at extinction  $\chi_{st,q}$  as a function of the stoichiometric mixture fraction  $\xi_{st}$ .

Additional computations using the San Diego mechanism [90] are carried out to elucidate the influence of  $\xi_{st}$  on the flame structure. The computations are performed at fixed values of  $T_{st} = 2000$  K and  $a_2 = 400$  s<sup>-1</sup>. Figure 5-15 shows the profiles of temperature, mass fractions of dimethyl ether (CH<sub>3</sub>OCH<sub>3</sub>), oxygen (O<sub>2</sub>), hydrogen (H<sub>2</sub>), carbon monoxide (CO), carbon dioxide (CO<sub>2</sub>) and water vapor (H<sub>2</sub>O) for  $\xi_{st} = 0.19$  and Figure 5-16 shows the same profiles for  $\xi_{st} = 0.6$ . It can be observed, that dimethyl ether is completely consumed in the reaction zone and that the profiles of H<sub>2</sub> and CO show maxima at these locations. These intermediate species are then consumed in the oxidation layer to form CO<sub>2</sub> and water vapor. This means the asymptotic structure of dimethyl ether flames is similar to the structure of many hydrocarbon and alcohol flames [108]. The mass fraction of oxygen  $Y_{O_2,st}$  at  $\xi_{st}$  is used as an indicator for the oxygen leakage from the reaction zone [108,109]. Comparing the O<sub>2</sub> profiles of Figure 5-15 and 5-16 shows an increase in O<sub>2</sub> leakage with increasing  $\xi_{st}$ . One way to improve predictions of the extinction strain rate  $a_q$  could be to increase the rate of consumption of O<sub>2</sub> molecules or O atoms by increasing the rate parameters of reactions that consume these species or by adding new pathways. This would reduce the leakage of oxygen and increase strain rate and scalar dissipation rate at extinction. The detailed results are listed in Appendix D.

## 5. Results and Discussion

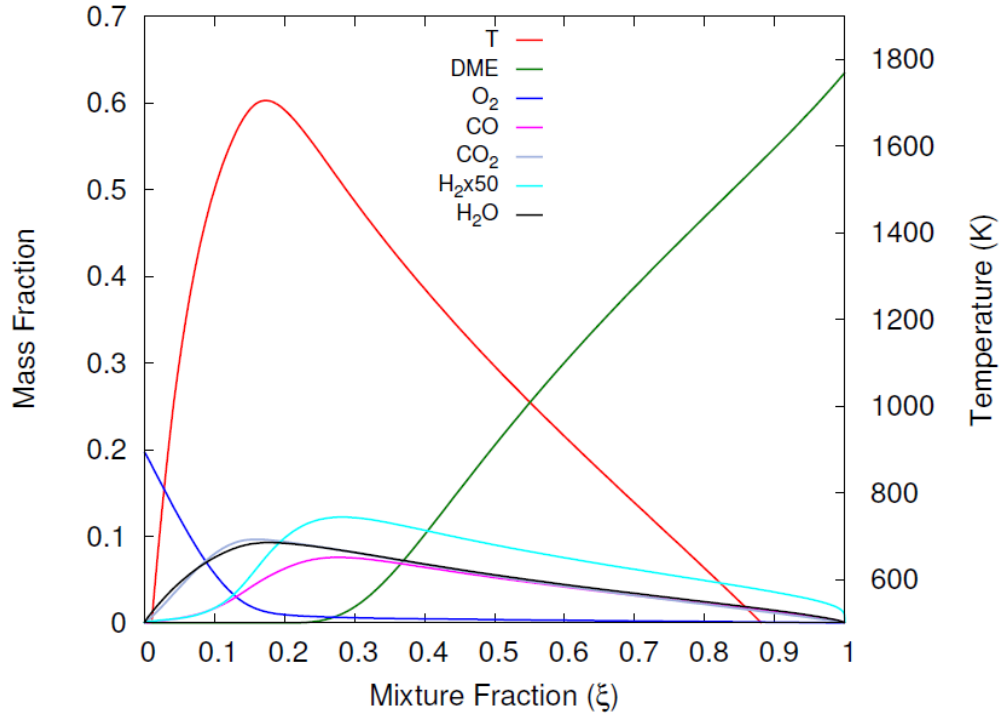


Figure 5-15: Profiles of  $T$  and mass fractions of CH<sub>3</sub>OCH<sub>3</sub>, O<sub>2</sub>, H<sub>2</sub>, CO, CO<sub>2</sub>, and H<sub>2</sub>O calculated using the San Diego mechanism for  $\xi_{st} = 0.19$ ,  $a_2 = 400$ ,  $T_{st} = 2000$  K.

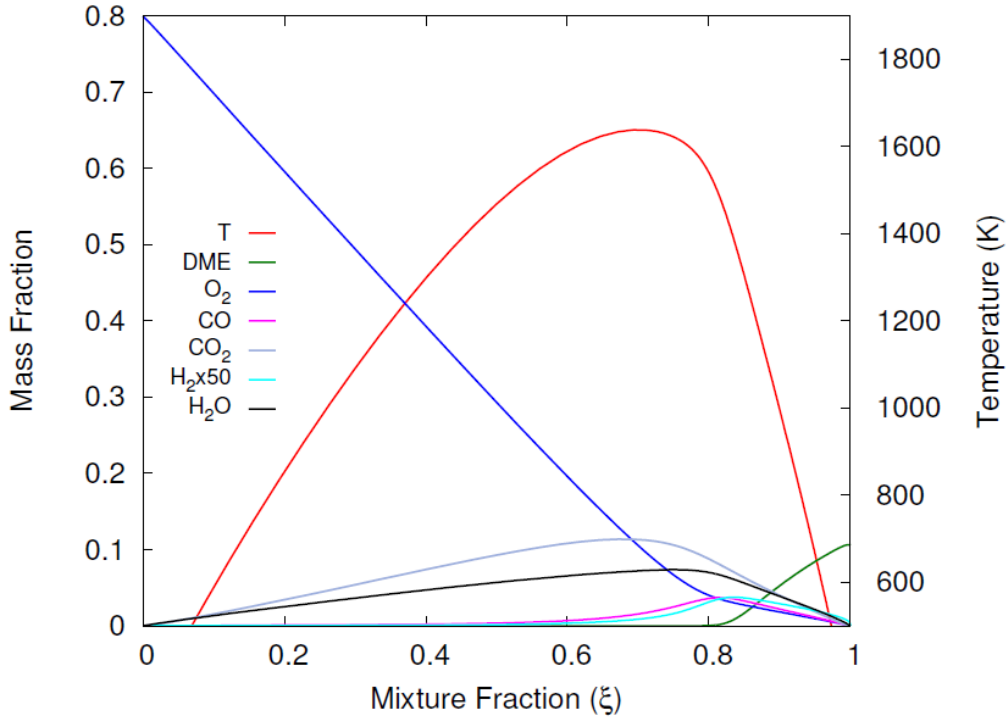


Figure 5-16: Profiles of  $T$  and mass fractions of CH<sub>3</sub>OCH<sub>3</sub>, O<sub>2</sub>, H<sub>2</sub>, CO, CO<sub>2</sub>, and H<sub>2</sub>O calculated using the San Diego mechanism for  $\xi_{st} = 0.6$ ,  $a_2 = 400$ ,  $T_{st} = 2000$  K.

## 6 Conclusion and Outlook

The work presented in this thesis is aimed to help understand combustion phenomena of hydrocarbon fuels. Due to stricter emissions regulations in many countries and the global effort to reduce the effects of the anthropogenic climate change, research in combustion phenomena is as important as ever. The counterflow burner configuration proofed to be a reliable and effective way to conduct research on one-dimensional diffusion flames at atmospheric and elevated pressures and further research projects should be carried out. Specifically research on diffusion flames at elevated pressures beyond 6 bar, which turned out to be the limit for the experiments carried out in this thesis, is of particular interest to develop cleaner and more efficient future combustion devices. The experiments in this thesis are limited to autoignition experiments of high molecular weight liquid hydrocarbon fuels at elevated pressures. Future experiments should also involve low molecular weight gaseous fuels and higher experimental pressures, like they occur in practical combustion devices. This requires a further upgrade of the High Pressure Combustion Experimental Facility at UC San Diego. In order to make experiments involving a counterflow burner in a higher pressure environment feasible, the laboratory needs to be equipped with a new gas delivery system. The current setup requires a considerable amount of time to replace empty gas bottles and therefore only allows for very short experiments at higher pressures which is not enough time to obtain valid experimental data. It has been observed that thermal expansion can cause an increase in separation distance between oxidizer and fuel duct for autoignition experiments within the HPCEF. An additional coolant pump in the coolant circuit could reduce thermal expansion of the autoignition duct. Additionally, it would be interesting to study radical and species formation prior to autoignition to better understand the decomposition process of fuels, since they are the known cause for toxic pollution. The HPCEF is designed to allow the use of optical measurement equipment and therefore would only require minor modifications.

## References

- [1] J. Warnatz, U. Maas, R.W. Dibble, *Combustion, 4th Edition*, 2006, ISBN-10 3-540-25992-9
- [2] Paris Agreement, United Nations Treaty Collection, 2016
- [3] International Energy Agency, Key world energy statistics, 2016
- [4] F.E. Fendell. Ignition and extinction in combustion of initially unmixed reactants. *Journal of Fluid Mechanics*, 21(2):291–303, March 1965.
- [5] A. Liñán. The asymptotic structure of counterflow diffusion flames for large activation energies. *Acta Astronautica*, 1(7-8):1007–1039, July 1974.
- [6] K. Seshadri and F. A. Williams. Laminar flow between parallel plates with injection of a reactant at high reynolds number. *International Journal of Heat and Mass Transfer*, 21(2):251–253, February 1978.
- [7] T. P. Pandya and F. J. Weinberg. The structure of flat, counter-flow diffusion flames. *Proceedings of the Royal Society of London A: Mathematical, Physical and Engineering Sciences*, 279(1379):544–561, 1964.
- [8] K. Seshadri, S. Humer, and R. Seiser, *Activation-energy asymptotic theory of autoignition of condensed hydrocarbon fuels in non-premixed flows with comparison to experiment*, *Combust. Theory Model.* 12 (2008), pp. 831–855.
- [9] S. Dooley, S.H. Won, J. Heyne, T.I. Farouk, Y. Ju, F.L. Dryer, K. Kumar, X. Hui, C.J. Sung, H. Wang, M.A. Oehlschlaeger, V. Iyer, S. Iyer, T.A. Litzinger, R.J. Santoro, T. Malewicki, and K. Brezinsky, *The experimental evaluation of a methodology for surrogate fuel formulation to emulate gas phase combustion kinetic phenomena*, *Combust. Flame* 159 (2012), pp. 1444–1466.
- [10] T. Malewicki, S. Gudiyella, and K. Brezinsky, *Experimental and modeling study on the oxidation of Jet A and the n-dodecane/iso-octane/n-propylbenzene/1,3,5-trimethylbenzene surrogate fuel*, *Combust. Flame* 160 (2013), pp. 17–30. Available at <http://dx.doi.org/10.1016/j.combustflame.2012.09.013>.
- [11] Y. Zhu, S. Li, D.F. Davidson, and R.K. Hanson, *Ignition delay times of conventional and alternative fuels behind reflected shock waves*, *Proc. Combust. Inst.* 35 (2015), pp. 241–248. Available at <http://dx.doi.org/10.1016/j.proci.2014.05.034>.

## References

- [12] K. Kumar and C.J. Sung, *An experimental study of the autoignition characteristics of conventional jet fuel/oxidizer mixtures: Jet-A and JP-8*, Combust. Flame 157 (2010), pp. 676–685.
- [13] N. Peters, G. Paczko, R. Seiser, and K. Seshadri, *Temperature cross-over and non-thermal runaway at two-stage ignition of n-heptane*, Combust. Flame 128 (2002), pp. 38–59.
- [14] K. Narayanaswamy, P. Pepiot, and H. Pitsch, *A chemical mechanism for low to high temperature oxidation of n-dodecane as a component of transportation fuel surrogates*, Combust. Flame 161 (2014), pp. 866–884.
- [15] L. Figura and A. Gomez, *Structure of incipiently sooting ethylene–nitrogen counterflow diffusion flames at high pressures*, Combust. Flame 161 (2014), pp. 1587–1603.
- [16] U. Niemann, K. Seshadri, and F.A. Williams, *Effect of pressure on structure and extinction of near-limit hydrogen counterflow diffusion flames*, Proc. Combust. Inst. 34 (2013), pp. 881–886.
- [17] U. Niemann, K. Seshadri, and F.A. Williams, *Methane, ethane, and ethylene laminar counterflow diffusion flames at elevated pressures: Experimental and computational investigations up to 2.0 MPa*, Combust. Flame 161 (2014), pp. 138–146.
- [18] R. Gehmlich, A. Kuo, and K. Seshadri, *Experimental investigations of the influence of pressure on critical extinction conditions of laminar non-premixed flames burning condensed hydrocarbon fuels, jet fuels, and surrogates*, Proc. Combust. Inst. 35 (2014), pp. 937–943.
- [19] A. Smallbone, W. Liu, C. Law, X. You, and H. Wang, *Experimental and modeling study of laminar flame speed and non-premixed counterflow ignition of n-heptane*, Proc. Combust. Inst. 32 (2009), pp. 1245–1252.
- [20] G. Jomaas, X. Zheng, D. Zhu, and C. Law, *Experimental determination of counterflow ignition temperatures and laminar flame speeds of C2–C3 hydrocarbons at atmospheric and elevated pressures*, Proc. Combust. Inst. 30 (2005), pp. 193–200.
- [21] S. Honnet, K. Seshadri, U. Niemann, and N. Peters, *A surrogate for kerosene*, Proc. Combust. Inst. 32 (2008), pp. 485–492.
- [22] S. Humer, R. Seiser, and K. Seshadri, *Experimental investigation of combustion of jet fuels and their surrogates in laminar non-premixed flows*, J. Propulsion & Power 27 (2011), pp. 847–855.
- [23] R. Seiser, H. Pitsch, K. Seshadri, W. Pitz, and H. Gurran, *Extinction and autoignition of n-heptane in counterflow configuration*, Proc. Combust. Inst. 28 (2000), pp. 2029–2037.



## References

- [24] R. Grana, K. Seshadri, A. Cuoci, U. Niemann, T. Faravelli, and E. Ranzi, *Kinetic modelling of extinction and autoignition of condensed hydrocarbon fuels in non-premixed flows with comparison to experiment*, Combust. Flame 159 (2012), pp. 130–141.
- [25] W. Liu, J.A. Koch, and C.K. Law, *Non-premixed ignition of C7–C16 normal alkanes in stagnating liquid pool*, Combust. Flame 158 (2011), pp. 2145–2148.
- [26] K. Kumar, C. Sung, *An experimental study of the autoignition characteristics of conventional jet fuel/oxidizer mixtures: Jet-A and JP-8*, Combustion and Flame, 157, 2010, Pages 676-685D.
- [27] Valco, K. Min, A. Oldani, T. Edwards, T. Lee, *Low temperature autoignition of conventional jet fuels and surrogate jet fuels with targeted properties in a rapid compression machine*, Proceedings of the Combustion Institute 36, 2017, Pages 3687-3694
- [28] K. Seshadri and F.A. Williams, *Laminar flow between parallel plates with injection of a reactant at high Reynolds number*, Int. J. Heat Mass Trans. 21 (1978), pp. 251–253.
- [29] P. Govindaraju, Q. Wang, M. Ihme, *Multicomponent Droplet Evaporation Using Group Contribution Methods*, Stanford University 9th US National Combustion Meeting, 2015
- [30] *Aviation Fuels-Technical Review*, Chevron, 2007
- [31] *Face Gasolines and Blends with Ethanol: Detailed Characterization of Physical and Chemical Properties*, Report No. AVFL-24, 2014
- [32] Sarathy, S. M.; Kukkadapu, G.; Mehl, M.; Wang, W.; Javed, T.; Park, S.; Oehlschlaeger, M. A.; Farooq, A.; Pitz, W. J.; Sung, C.-J., *Ignition of alkane-rich FACE gasoline fuels and their surrogate mixtures*, Proc. Combustion Institute, 2015, 35 (1), pages 249–257.
- [33] Wallington TJ, Kaiser EW, Farrell JT. *Automotive fuels and internal combustion engines: a chemical perspective*, Chem Soc Rev 2006, 35(4), pages 335–47.
- [34] Pitz WJ, Cernansky NP, Dryer FL, Egolfopoulos FN, Farrell JT, Friend DG, et al. *Development of an experimental database and chemical kinetic models for surrogate gasoline fuels*. SAE 2007-01-0175.
- [35] T. Javed, E. Nasir, E. Es-Sebbar, A. Farooq, *A comparative study of the oxidation characteristics of two gasoline fuels and an n-heptane/iso-octane surrogate mixture*, Fuel, 2015, 140, pages 201–208.
- [36] B. Chen, C. Togbé, H. Selim, P. Dagaut, and M. Sarathy, *Quantities of Interest in Jet Stirred Reactor Oxidation of a High-Octane Gasoline*, Energy Fuels, 2017, 31 (5), pages 5543–5553
- [37] Sarathy, S. M.; Kukkadapu, G.; Mehl, M.; Javed, T.; Ahmed, A.; Naser, N.; Tekawade, A.;

## References

- Kosiba, G.; AlAbbad, M.; Singh, E.; Park, S.; Rashidi, M. Al; Chung, S. H.; Roberts, W. L.; Oehlschlaeger, M. A.; Sung, C.-J.; Farooq, A., *Compositional effects on the ignition of FACE gasolines*, Combustion and Flame, 2016, 169, pages 171–193.
- [38] E. Ranzi, *A Wide-Range Kinetic Modeling Study of Oxidation and Combustion of Transportation Fuels and Surrogate Mixtures*, Energy and Fuels, 2006, 20 (3), pages 1024–1032
- [39] Dooley, S.; Won, S. H.; Heyne, J.; Farouk, T. I.; Ju, Y.; Dryer, F. L.; Kumar, K.; Hui, X.; Sung, C.-J.; Wang, H.; Oehlschlaeger, M. A.; Iyer, V.; Iyer, S.; Litzinger, T. A.; Santoro, R. J.; Malewicki, T.; Brezinsky, K., *The experimental evaluation of a methodology for surrogate fuel formulation to emulate gas phase combustion kinetic phenomena*, Combustion and Flame, 2012, 159 (4), pages 1444–1466.
- [40] Andac, M. G.; Egolfopoulos, F. N., *Diffusion and kinetics effects on the ignition of pre-mixed and non-premixed flames*, Proceedings of the Combustion Institute, 2007, 31 (1), pages 1165–1172
- [41] T. Bieleveld, A. Frassoldati, A. Cuoci, T. Faravelli, E. Ranzi, U. Niemann, et al., *Experimental and kinetic modeling study of combustion of gasoline, its surrogates and components in laminar non-premixed flows*, Proceedings of the Combustion Institute, 32, 2009, pages 493-500
- [42] Semelsberger, T. A., Borup, R. L., and Greene, H. L. 2006. *Dimethyl ether (DME) as an alternative fuel*. Journal of Power Sources 156, 2, pages 497–511.
- [43] U. Burke, K. Somers, P. O'Toole, C. Zinner, N. Marquet, G. Bourque, E. Petersen, W. Metcalfe, Z. Serinyel, H. Curran, *An ignition delay and kinetic modeling study of methane, dimethyl ether, and their mixtures at high pressures*, Combustion and Flame 162, 2015, pages 315-330
- [44] C.A. Daly, J.M. Simmie, J. Wurnel, N. Djeballi, C. Paillard, Combust. Flame 125 (2001) 1329–1340.
- [45] W. Ying, L. Genbao, Z. Wei, Z. Longbao, Fuel Process. Technol. 89 (2008) 1272–1280.
- [46] W. Ying, Z. Longbao, Energy Fuels 21 (2007) 1454–1458.
- [47] S.C. Sorensen, ASME transactions, J. Eng. Gas Turbines Power 123 (2001) 652–658.
- [48] P. Kapus, H. Ofner, Development of Fuel Injection Equipment and Combustion System for DI Diesels Operated on Dimethyl Ether, SAE Technical Paper 950062, 1995.
- [49] M. Yao, Z. Zheng, Z. Chen, B. Zhang, SAE 2004-01-2993, 2004.
- [50] H. Yamada, M. Yoshii, A. Tezaki, Proc. Combust. Inst. 30 (2005) 2773–2780.

## References

- [51] M. Konno, Z. Chen, K. Miki, SAE 2003-01-1826, 2003.
- [52] Changwei Ji, Lei Shi, Shuofeng Wang, Xiaoyu Cong, Teng Su, Menghui Yu, Investigation on performance of a spark-ignition engine fueled with dimethyl ether and gasoline mixtures under idle and stoichiometric conditions
- [53] Su Han Park, Chang Sik Lee, Applicability of dimethyl ether (DME) in a compression ignition engine as an alternative fuel
- [54] Y. Wang, P. Veloo, F. Egolfopoulos, T. Tsotsis, *A comparative study on the extinction characteristics of non-premixed dimethyl ether and ethanol flames*, Proceedings of the Combustion Institute 33, 2011, pages 1003-1010
- [55] Philipp Mairhofer, *Structure and Extinction of Flames Mixtures of Biofuels and Hydrocarbon Fuels*, Master thesis, Vienna University of Technology, 2016
- [56] S. Humer, A. Frassoldati, S. Granata, T. Faravelli, E. Ranzi, R. Seiser, and K. Seshadri. Experimental and kinetic modeling study of combustion of JP-8, its surrogates and reference components in laminar nonpremixed flows. Proceedings of the Combustion Institute, 31(1):393–400, January 2007.
- [57] K Seshadri, T Lu, O Herbinet, S Humer, U Niemann, WPitz, R Seiser, and C Law. Experimental and kinetic modeling study of extinction and ignition of methyl decanoate in laminar non-premixed flows. Proceedings of the Combustion Institute, 32(1):1067–1074, 2009.
- [58] R. Grana, A. Frassoldati, T. Faravelli, U. Niemann, E. Ranzi, R. Seiser, R. Cattolica, and K. Seshadri. An experimental and kinetic modeling study of combustion of isomers of butanol. Combustion and Flame, 157(11):2137–2154, June 2010
- [59] A. Frassoldati, A. Cuoci, T. Faravelli, U. Niemann, E. Ranzi, R. Seiser, and K. Seshadri. An experimental and kinetic modeling study of n-propanol and isopropanol combustion. Combustion and Flame, 157(1):2–16, January 2010.
- [60] K. Seshadri, A. Frassoldati, A. Cuoci, T. Faravelli, U. Niemann, P. Weydert, and E. Ranzi. Experimental and kinetic modeling study of combustion of JP-8, its surrogates and components in laminar premixed flows. Combustion Theory and Modelling, 15(4):569–583, August 2011.
- [61] R. Seiser, U. Niemann, and K. Seshadri. Experimental study of combustion of ndecane and JP-10 in non-premixed flows. Proceedings of the Combustion Institute, 33(1):1045–1052, 2011.
- [62] U. Niemann, R. Seiser, and K. Seshadri. Ignition and extinction of low molecular weight esters in nonpremixed flows. Combustion Theory and Modelling, 14(6): 875–891, November 2010.

## References

- [63] S. Mani, U. Niemann, C. Yeung, R.K. Gehmlich, C.K. Westbrook, M. Plomer, Z. Luo, M. Mehl, W.J. Pitz, K. Seshadri, M.J. Thomson, and T. Lu. A counterflow diffusion flame study of branched octane isomers. *Proceedings of the Combustion Institute*, 34(1):1015–1023, January 2013.
- [64] P. Mairhofer, G. Mairinger, K. Seshadri, X. Bai, R. Seiser, E. Pucher, *Rate-ratio asymptotic analysis of the influence of stoichiometric mixture fraction on structure and extinction of laminar, nonpremixed methane flames with comparison to experiments*, *Proceedings of the Combustion Institute*, Volume 36, Issue 1, 2017, Pages 1495-1503
- [65] R. Gehmlich, A. Kuo, K. Seshadri, *Experimental investigations of the influence of pressure on the critical conditions of laminar nonpremixed flames burning condensed hydrocarbon fuels, jet fuels and surrogates*, *Proceedings of the Combustion Institute*, Volume 35, Issue 1, 2015, Pages 937-943.
- [66] U. Niemann, K. Seshadri, F.A. Williams, *Effect of pressure on structure and extinction of near-limit hydrogen counterflow diffusion flames*, *Proceedings of the Combustion Institute*, 34, 2013, Pages 881-886.
- [67] U. Niemann, K. Seshadri, F.A. Williams, *Methane, ethane and ethylene laminar counterflow diffusion flames at elevated pressures: Experimental and computational studies up to 2 MPa*, *Combustion and Flame*, Volume 161, Issue 1, January 2014, Pages 138-146.
- [68] G. Mairinger, A. Frassoldati, R. Gehmlich, U. Niemann, A. Stagni, E. Ranzi, K. Seshadri, *Autoignition of condensed hydrocarbon fuels in non-premixed flows at elevated pressures*, *Combustion Theory and Modelling*, Vol. 20, No. 6, 2016, Pages 995-1009.
- [69] R. Gehmlich, *Experimental Studies on Nonpremixed Combustion at Atmospheric and Elevated Pressures*, *PhD thesis*, University of California; San Diego, 2013.
- [70] C.R. Shaddix. Correcting thermocouple measurements for radiation loss: a critical review. In *Proceedings of the National Heat Transfer Conference*, pages 1–10, Albuquerque, New Mexico, 1999.
- [71] E. Ranzi, A. Frassoldati, R. Grana, A. Cuoci, T. Faravelli, A. Kelley, and C. Law, *Hierarchical and comparative kinetic modeling of laminar flame speeds of hydrocarbon and oxygenated fuels*, *Prog. Energy Combust. Sci.* 38 (2012), pp. 468–501.
- [72] <http://creckmodeling.chem.polimi.it>.
- [73] E. Ranzi, A. Frassoldati, A. Stagni, M. Pelucchi, A. Cuoci, and T. Faravelli, *Reduced kinetic schemes of complex reaction systems: Fossil and biomass-derived transportation fuels*, *Int. J. Chem. Kinetics* 46 (2014), pp. 512–542.

## References

- [74] A. Stagni, A. Frassoldati, A. Cuoci, T. Faravelli, and E. Ranzi, *Skeletal mechanism reduction through species-targeted sensitivity analysis*, Combust. Flame 163 (2016), pp. 382–393.
- [75] M. Mehl, W.J. Pitz, C.K. Westbrook, and H.J. Curran, *Kinetic modeling of gasoline surrogate components and mixtures under engine conditions*, Proc. Combust. Inst. 33 (2011), pp. 193–200.
- [76] H.K. Ciezki and G. Adomeit, *Shock-tube investigation of self-ignition of n-heptane-air mixtures under engine relevant conditions*, Combust. Flame 93 (1993), pp. 421–433.
- [77] H.S. Shen, J. Steinberg, J. Vanderover, and M.A. Oehlschlaeger, *A shock tube study of the ignition of n-heptane, n-decane, n-dodecane, and n-tetradecane at elevated pressures*, Energy & Fuels 23 (2009), pp. 2482–2489. Available at <http://dx.doi.org/10.1021/ef8011036>.
- [78] U. Pfahl, K. Fieweger, and G. Adomeit, *Self-ignition of diesel-relevant hydrocarbon-air mixtures under engine conditions*, Symp. (Int.) Combust. 26 (1996), pp. 781–789. Available at [http://dx.doi.org/10.1016/S0082-0784\(96\)80287-6](http://dx.doi.org/10.1016/S0082-0784(96)80287-6).
- [79] V.P. Zhukov, V.A. Sechenov, and A.Y. Starikovskii, *Autoignition of n-decane at high pressure*, Combust. Flame 153 (2008), pp. 130–136.
- [80] S. Vasu, D. Davidson, Z. Hong, V. Vasudevan, and R. Hanson, *n-dodecane oxidation at high pressures: Measurements of ignition delay times and OH concentration time-histories*, Proc. Combust. Inst. 32 (2009), pp. 173–180.
- [81] D.F. Davidson, D.R. Haylett, and R.K. Hanson, *Development of an aerosol shock tube for kinetic studies of low-vapor-pressure fuels*, Combust. Flame 155 (2008), pp. 108–117. Available at <http://dx.doi.org/10.1016/j.combustflame.2008.01.006>.
- [82] A. Agosta, N. P. Cernansky, D. L. Miller, T. Faravelli, E. Ranzi, *Experimental Thermal and Fluid Science* 28 (2004) 701–708.
- [83] B. W. Weber, W. J. Pitz, M. Mehl, E. J. Silke, A. C. Davis, C.-J. Sung, *Combustion and Flame* 161 (2014) 1972 - 1983.
- [84] A. Cuoci, A. Frassoldati, T. Faravelli, and E. Ranzi, *OpenSMOKE++: An objectoriented framework for the numerical modeling of reactive systems with detailed kinetic mechanisms*, Comput. Phys. Comm. 192 (2015), pp. 237–264. Available at <http://dx.doi.org/10.1016/j.cpc.2015.02.014>.
- [85] A. Cuoci, A. Frassoldati, T. Faravelli, and E. Ranzi, *Frequency response of counterflow diffusion flames to strain rate harmonic oscillations*, Combust. Sci. Technol. 180 (2008), pp. 767–784.

## References

- [86] K. Seshadri, A. Frassoldati, A. Cuoci, T. Faravelli, U. Niemann, P. Weydert, and E. Ranzi, *Experimental and kinetic modeling study of combustion of JP-8, its surrogates and components in laminar premixed flows*, Combust. Theory Model. 15 (2011), pp. 569–583. Available at <http://dx.doi.org/10.1080/13647830.2011.552635>.
- [87] J. M. Smith, H. C. V. Ness, M. M. Abbott, Introduction to Chemical Engineering Thermodynamics, Mc Graw Hill, 7th edition, 1996.
- [88] D. W. Green, R. H. Perry, Perry's Chemical Engineers' Handbook, McGraw Hill, 8 edition, 2008.
- [89] Luo, Z.; Som, S.; Sarathy, S. M.; Plomer, M.; Pitz, W. J.; Longman, D. E.; Lu, T. *Combust. Theory Model.* 2014, 18 (2), 187–203.
- [90] The San Diego Mechanism, <http://combustion.ucsd.edu/>, 2009.
- [91] J. Prince, Chemical kinetics of oxidation of dme, private communication, 2015.
- [92] H. Pitsch, M. Bollig, FlameMaster v3.3.10: A computer code for homogeneous combustion and one-dimensional laminar flame calculations, 1998.
- [93] E. Ranzi, C. Cavallotti, A. Cuoci, A. Frassoldati, M. Pelucchi, and T. Faravelli, *New reaction classes in the kinetic modeling of low temperature oxidation of n-alkanes*, Combust. Flame 162, (2015), pp. 1679–1691.
- [94] M. Pelucchi, M. Bissoli, C. Cavallotti, A. Cuoci, T. Faravelli, A. Frassoldati, E. Ranzi, and A. Stagni, *Improved kinetic model of the low-temperature oxidation of n-heptane*, Energy & Fuels 28 (2014), pp. 7178–7193, <http://dx.doi.org/10.1021/ef501483f>.
- [95] A. Frassoldati, G. D'Errico, T. Lucchini, A. Stagni, A. Cuoci, T. Faravelli, A. Onorati, and E. Ranzi, *Reduced kinetic mechanisms of diesel fuel surrogate for engine CFD simulations*, Combust. Flame 162 (2015), pp. 3391–4007.
- [96] A. Cuoci, A. Frassoldati, T. Faravelli, E. Ranzi, Proceedings of the Combustion Institute 35 (2015) 1621-1627.
- [97] A. Frassoldati, G. D'Errico, T. Lucchini, A. Stagni, A. Cuoci, T. Faravelli, A. Onorati, E. Ranzi, Combustion and Flame 162 (2015) 3391-4007.
- [98] Z. Zhao, M. Chaos, A. Kazakov, F. L. Dryer, International Journal of Chemical Kinetics 40 (2008) 1-18.
- [99] H. Song, P. Wang, R. S. Boles, D. Matinyan, H. Praphanphap, J. Piotrowicz, P. D. Ronney, Proceedings of the Combustion Institute 36 (2017) 1403-1409.

## References

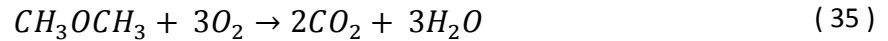
- [100] J. Hashimoto, J. Hosono, K. Shimizu, R. Urakawa, K. Tanoue, Proceedings of the Combustion Institute 36 (2017) 1439 { 1446.
- [101] J. Beeckmann, L. Cai, A. Berens, N. Peters, H. Pitsch, Proceedings of the Combustion Institute 35 (2015) 275-281.
- [102] S. Deng, D. Han, C. K. Law, Combustion and Flame 176 (2017) 143 - 150.
- [103] C. K. Law, P. Zhao, Combustion and Flame 159 (2012) 1044 - 1054.
- [104] S. Deng, P. Zhao, D. Zhu, C. K. Law, Combustion and Flame 161 (2014) 1993 - 1997
- [105] Z. Wang, X. Zhang, L. Xing, L. Zhang, F. Herrmann, K. Moshhammer, F. Qi, K. Kohse-Hinghaus, Combustion and Flame 162 (2015) 1113 - 1125.
- [106] Pitsch, H. 2014. *Laminar Diffusion Flames*. CEFRC Summer School, Princeton. RWTH Aachen University
- [107] J. S. Kim, F. A. Williams, SIAM Journal on Applied Mathematics 53 (1993) 1551-1566.
- [108] K. Seshadri, Symposium (International) on Combustion 26 (1996) 831- 846.
- [109] K. Seshadri, X. S. Bai, Proceedings of the Combustion Institute 31(2006) 1181-1188.

## Appendix

### Appendix A

The following formulation describes the process of determining the fuel and oxidizer stream composition in order to maintain a fixed stoichiometric mixture fraction  $\xi_{st}$  and adiabatic flame temperature  $T_{st}$ . The asymptotic formulation for calculating the mass fractions for DME and oxygen were derived by Prof. Seshadri.

The overall chemical reaction between dimethyl ether ( $\text{CH}_3\text{OCH}_3$ ) and oxygen ( $\text{O}_2$ ) is



The reactions rate is denoted as  $\omega_{DME}$  with the unit  $1/(\text{m}^3 \text{ s})$ .

Consider two opposing streams flowing towards a stagnation plane. One stream is referred to as the fuel stream and is directed from the fuel boundary towards the stagnation plane. It consists of  $\text{CH}_3\text{OCH}_3$  and  $\text{N}_2$ . The mass fraction of dimethyl ether in the fuel stream is denoted as  $Y_{DME,1}$ . Subscript 1 represents the condition at the fuel side boundary. The other stream is referred to as the oxidizer stream and is directed from the oxidizer side towards the stagnation plane. The stream consists of  $\text{O}_2$  and  $\text{N}_2$ . The mass fraction of oxygen in the oxidizer stream is denoted as  $Y_{\text{O}_2,2}$ . Subscript 2 represents the condition at the oxidizer side boundary.

The species balance equations are



## Appendix

$$\rho a \hat{x} \frac{dY_{DME}}{d\hat{x}} + \rho D_{DME} \frac{d^2 Y_{DME}}{d\hat{x}^2} = W_{DME} \omega_{DME} \quad (36)$$

$$\rho a \hat{x} \frac{dO_2}{d\hat{x}} + \rho D_{O_2} \frac{d^2 Y_{O_2}}{d\hat{x}^2} = 3W_{O_2} \omega_{DME}$$

Here  $D_{DME}$  and  $D_{O_2}$  respectively are the coefficient of diffusion for  $CH_3OCH_3$  and  $O_2$ . The energy conservation equation is

$$\rho c_p a \frac{dT}{d\hat{x}} + \lambda \frac{d^2 T}{d\hat{x}^2} + \sum_{i=1}^n \rho D_i c_{p,i} \frac{dY_i}{d\hat{x}} \frac{dT}{d\hat{x}} = -Q_{DME} \omega_{DME} \quad (37)$$

Here  $\lambda$  is the coefficient of thermal conductivity,  $c_p$  is the heat capacity of the mixture,  $c_{p,i}$  is the heat capacity of species  $i$ ,  $D_i$  is the coefficient of diffusion of species  $i$ , and  $Q_{dme}$  is the heat released per mole of  $CH_3OCH_3$  consumed.

Define the independent variable

$$x = \hat{x} \left( \frac{\rho c_p a}{\lambda} \right)^{1/2} \quad (38)$$

For convenience, the following definitions are introduced

$$X_i = Y_i W_{N_2} / W_i$$

$$\tau = (T - T_{ref}) / \Delta T_{ref} \quad (39)$$

$$M_{DME} = W_{N_2} \omega_{DME} / (\rho a)$$

$$G_{DME} = Q_{DME} / (W_{N_2} c_p \Delta T_{ref})$$

$W_i$  denotes the molecular weight of species  $i$ ,  $W_{N_2}$  is the molecular weight of nitrogen,  $T_{ref}$  is a reference temperature and  $\Delta T_{ref}$  is a reference temperature difference.

## Appendix

Introducing equation (38) and (39) into equation (36), the following equations are obtained,

$$x \frac{dX_{DME}}{dx} + \frac{1}{Le_{DME}} \frac{d^2 X_{DME}}{dx^2} = M_{DME} \quad (40)$$

$$x \frac{dX_{O_2}}{dx} + \frac{1}{Le_{O_2}} \frac{d^2 X_{O_2}}{dx^2} = 3M_{DME}$$

Introducing equation (38) and (39) into equation (37), the following equations are obtained,

$$x \frac{d\tau}{dx} + \frac{d^2 \tau}{dx^2} + \sum_{i=1}^n \frac{1}{Le_i} \frac{W_i}{W_{N_2}} \frac{c_{p,i}}{c_p} \frac{dX_i}{dx} \frac{d\tau}{dx} = -G_{DME} M_{DME} \quad (41)$$

The conserved scalar quantities  $\xi$  and  $\xi_{DME}$  are defined by the following equations

$$x \frac{d\xi}{dx} + \frac{d^2 \xi}{dx^2} = 0 \quad (42)$$

$$x \frac{d\xi_{DME}}{dx} + \frac{1}{Le_{DME}} \frac{d^2 \xi_{DME}}{dx^2} = 0$$

Equation (42) is constrained to satisfy the conditions

$$\xi = \xi_{DME} = 0; \quad x = \infty \quad (43)$$

$$\xi = \xi_{DME} = 1; \quad x = -\infty$$

Integration of equation (42) together with equation (43) gives

## Appendix

$$\xi = \frac{1}{2} \operatorname{erfc} \left( x \sqrt{\frac{1}{2}} \right) \quad (44)$$

$$\xi_{DME} = \frac{1}{2} \operatorname{erfc} \left( x \sqrt{\frac{Le_{DME}}{2}} \right)$$

Differentiation of equation (44) gives

$$\frac{d\xi}{dx} = - \left( \sqrt{\frac{1}{2\pi}} \right) \exp \left( -\frac{x^2}{2} \right) \quad (45)$$

$$\frac{d\xi_{DME}}{dx} = - \left( \sqrt{\frac{Le_{DME}}{2\pi}} \right) \exp \left( -\frac{x^2 Le_{DME}}{2} \right)$$

It follows from equation (45)

$$\frac{d\xi_{DME}}{dx} = (\sqrt{Le_{DME}}) \frac{d\xi}{dx} \left\{ \exp \left[ \frac{x^2 (1 - Le_{DME})}{2} \right] \right\} \quad (46)$$

### Coupling Relations at $x_{st}$

The flame sheet is located at  $x = x_{st}$ . At the location of the flame sheet,  $\xi = \xi_{st}$  and  $\xi_{DME} = \xi_{DME,st}$ .

At  $x_{st}$ ,  $\text{CH}_3\text{OCH}_3$  and  $\text{O}_2$  are completely consumed. At  $x_{st}$ , the gradients are

## Appendix

$$\begin{aligned}
 \frac{1}{Le_{DME}} \frac{dX_{DME}}{dx} + \frac{1}{Le_{DME}} \frac{dX_{DME}}{\xi_{DME}} \frac{d\xi_{DME}}{dx} &= \frac{1}{Le_{DME}} \frac{X_{DME,1}}{1 - \xi_{DME,st}} \frac{d\xi_{DME}}{dx} \\
 \frac{dX_{CO_2}}{dx} &= \frac{dX_{CO_2}}{d\xi} \frac{d\xi}{dx} = \frac{X_{CO_2,st}}{1 - \xi_{st}} \frac{d\xi}{dx} \\
 \frac{dX_{H_2O}}{dx} &= \frac{dX_{H_2O}}{d\xi} \frac{d\xi}{dx} = \frac{X_{H_2O,st}}{1 - \xi_{st}} \frac{d\xi}{dx} \\
 \frac{d\tau}{dx} &= \frac{d\tau}{d\xi} \frac{d\xi}{dx} = \frac{\tau_{st}}{1 - \xi_{st}} \frac{d\xi}{dx}
 \end{aligned} \tag{47}$$

At  $x_{st+}$  the gradients are

$$\begin{aligned}
 \frac{dX_{O_2}}{dx} &= \frac{dX_{O_2}}{d\xi} \frac{d\xi}{dx} = -\frac{X_{O_2,2}}{\xi_{st}} \frac{d\xi}{dx} \\
 \frac{dX_{CO_2}}{dx} &= \frac{dX_{CO_2}}{d\xi} \frac{d\xi}{dx} = \frac{X_{CO_2,st}}{\xi_{st}} \frac{d\xi}{dx} \\
 \frac{dX_{H_2O}}{dx} &= \frac{dX_{H_2O}}{d\xi} \frac{d\xi}{dx} = \frac{X_{H_2O,st}}{\xi_{st}} \frac{d\xi}{dx} \\
 \frac{d\tau}{dx} &= \frac{d\tau}{d\xi} \frac{d\xi}{dx} = \frac{\tau_{st}}{\xi_{st}} \frac{d\xi}{dx}
 \end{aligned} \tag{48}$$

The gradients at  $\xi_{st+}$  are

## Appendix

$$\frac{1}{Le_{DME}} \frac{dX_{DME}}{d\xi} = \frac{1}{\sqrt{Le_{DME}}} \frac{X_{DME,1}}{1 - \xi_{DME,st}} \left\{ \exp \left[ \frac{x^2(1 - Le_{DME})}{2} \right] \right\} = m$$

$$\frac{dX_{CO_2}}{d\xi} = - \frac{X_{CO_2,st}}{1 - \xi_{st}}$$

$$\frac{dX_{H_2O}}{d\xi} = - \frac{X_{H_2O,st}}{1 - \xi_{st}}$$

$$\frac{d\tau}{d\xi} = - \frac{\tau}{1 - \xi_{st}} = -p$$
( 49 )

At  $\xi_{st}$ - the gradients are

$$\frac{dX_{O_2}}{d\xi} = - \frac{X_{O_2,2}}{\xi_{st}} = -c$$

$$\frac{dX_{H_2O}}{d\xi} = \frac{X_{CO_2,st}}{\xi_{st}}$$

$$\frac{dX_{H_2O}}{d\xi} = \frac{X_{H_2O,st}}{\xi_{st}}$$

$$\frac{d\tau}{d\xi} = \frac{\tau_{st}}{\xi_{st}} = s$$
( 50 )

The balance equation for carbon across the reaction zone at  $x = x_{st}$  is

$$\left( \frac{2}{Le_{DME}} \frac{dX_{DME}}{dx} + \frac{dX_{CO_2}}{dx} \right)_{\pm} = 0$$
( 51 )

The balance equation for oxygen across the reaction zone at  $x = x_{st}$  is

$$\left( \frac{1}{Le_{DME}} \frac{dX_{DME}}{dx} + 2 \frac{dX_{O_2}}{dx} + 2 \frac{dX_{CO_2}}{dx} + \frac{dX_{H_2O}}{dx} \right)_{\pm} = 0$$
( 52 )

The balance equation for hydrogen across the reaction zone at  $x = x_{st}$  is

## Appendix

$$\left( \frac{3}{Le_{DME}} \frac{dX_{DME}}{dx} - \frac{dX_{H_2O}}{dx} \right)_{\pm} = 0 \quad (53)$$

It follow from equation (51), (52) and (53)

$$\left( \frac{3}{Le_{DME}} \frac{dX_{DME}}{dx} - \frac{dX_{O_2}}{dx} \right)_{\pm} = 0 \quad (54)$$

Integration of equation (49), and (50) into equation (54) gives

$$3m = c \quad (55)$$

Coupling relations for temperature gives

$$\left( \frac{d\tau}{dx} \frac{G_{DME}}{Le_{DME}} - \frac{dX_{DME}}{dx} \right)_{\pm} = 0 \quad (56)$$

This gives

$$\tau_{st} = mG_{DME}\xi_{st}(1 - \xi_{st}) \quad (57)$$

The adiabatic flame temperature  $T_{st}$  is given by

$$T_{st} = T_u + \frac{m}{c_p W_{N_2}} Q_{DME} \xi_{st}(1 - \xi_{st}) \quad (58)$$

## Appendix B

Table B-1 lists the experimental results of the study on critical conditions at autoignition of n-heptane, n-decane and n-dodecane. The autoignition temperatures  $T_{ig}$  are listed as a function of pressure  $p$ .

Pressure [bar]	Heptane	Decane	Dodecane
3	1123	1086	1049
4	1023	994	976
4,5	990	972	954
5	960	943	927
6	927	911	895

Table B-1: Autoignition temperatures for n-heptane, n-decane and n-dodecane.

Table B-2 lists the experimental results of the study on critical conditions at autoignition of jet fuels and jet fuel surrogates. The autoignition temperatures  $T_{ig}$  are listed as a function of pressure  $p$ .

Pressure [bar]	Surrogate C	Aachen	Princeton	JP5	JetA	JP8
3	1171	1120	1184	1167	1169	1160
4	1113	1048	1149	1099	1101	1085
5	1064	991	1107	1047	1051	1022
6	1043	933,	1080	1019	1002	967

Table B-2: Autoignition temperatures of the jet fuels and jet fuel surrogates.

## Appendix C

Table C-1 lists the experimental results of the study on critical conditions at extinction of the FACE fuels. The oxidizer strains rates at extinction  $a_2$  are listed as a function of fuel mass fraction in the fuel stream  $Y_{F,1}$ .

Fuel mass fraction	FACE A	FACE C	FACE F	FACE I	FACE G	FACE J
0,25	153	143	146	161	136	144
0,3	196	193	199	218	190	199
0,35	253	242	252	270	235	247
0,4	305	290	299	320	279	289

Table C-1: Strain rate at extinction  $a_{2,q}$  for the FACE fuels for several fuel mass fractions  $Y_{F,1}$ .

Table C-2 lists the experimental results of the study on critical conditions at autoignition of the FACE fuels. The autoignition temperatures  $T_{ig}$  in K are listed as a function of the oxidizer strain rate  $a_2$ .

Strain rate [1/s]	FACE A	FACE C	FACE F	FACE G	FACE I	FACE J
350	1181	1193	1188	1188	1182	1190
300	1176	1184	1182	1174	1174	1176
250	1169	1177	1172	1164	1165	1161
200	1156	1157	1160	1152	1154	1145
150	1136	1141	1141	1133	1133	1127

Table C-2: Autoginition temperatures  $T_{ig}$  for the FACE fuels for several oxidizer strain rates  $a_2$ .



## Appendix D

Table D-1 lists the calculated stoichiometric mixture fractions and the obtained experimental data for the study on critical limits of extinction of dimethyl ether for  $T_{st}=2000K$ . The table lists the stoichiometric mixture fraction  $\xi_{st}$ , the corresponding mixture fractions  $Y_{DME,1}$  and  $Y_{O_2,2}$ , fuel and oxidizer strain rates  $a_1$  and  $a_2$  at extinction and the duct exit velocities  $V_1$  and  $V_2$ .

$\xi_{st}$	$Y_{DME,1}$	$Y_{O_2,2}$	$a_2$	$a_1$	$V_2$ (m/s)	$V_1$ (m/s)
0,13432	1	0,1848	555	441	1,3875	1,10201
0,16	0,7945	0,1904	530	448	1,325	1,1203
0,19	0,6351	0,1975	515	455	1,2875	1,13242
0,22	0,5256	0,2051	500	454	1,25	1,13595
0,3136	0,3349	0,2330	498	474	1,245	1,1856
0,4	0,2471	0,2666	495	481	1,2375	1,20413
0,5	0,1877	0,3199	527	521	1,3175	1,30287
0,6	0,1503	0,3999	550	551	1,375	1,37759
0,7	0,1247	0,5332	610	619	1,525	1,54956
0,8	0,1060	0,7997	800	830	2	2,07719

Table D-1: Experimental data of the study on critical limits of extinction for  $T_{st}=2000K$ .

## Appendix

Table D-2 lists the calculated stoichiometric mixture fractions and the obtained experimental data for the study on critical limits of extinction of dimethyl ether for several  $T_{st}$ . The table lists the stoichiometric mixture fraction  $\xi_{st}$ , the corresponding mixture fractions  $Y_{DME,1}$  and  $Y_{O_2,2}$  and fuel and oxidizer strain rates  $a_1$  and  $a_2$  at extinction.

$\xi_{st}$	$Y_{DME,1}$	$Y_{O_2,2}$	$a_2$	$a_1$	$T_{st}$
0,22	0,5102	0,1990	404	366	1950
0,40	0,2399	0,2587	391	378	1950
0,60	0,1459	0,3881	444	441	1950
0,22	0,5179	0,2020	448	405	1975
0,40	0,2435	0,2627	447	432	1975
0,60	0,1481	0,3940	496	492	1975
0,22	0,5334	0,2081	528	474	2025
0,40	0,2508	0,2705	523	515	2025
0,60	0,1525	0,4057	590	486	2025
0,22	0,5411	0,2111	582	522	2050
0,40	0,2544	0,2744	560	554	2050
0,60	0,1547	0,4116	641	637	2050

Table D-2: Experimental data of the study on critical limits of extinction for several  $T_{st}$ .

# Curriculum Vitae

Date of birth: August 1st 1987  
Place of birth: Linz  
Nationality: Austria

## Education

07/2014 - 05/2018 Doctorate, University of Technology, Vienna  
10/2007 - 12/2013 Dipl.-Ing. in Mechanical Engineering, University of Technology,  
Vienna  
09/1998 - 07/2006 Bundesrealgymnasium Landwiedstrasse, Linz  
09/1994 - 07/1998 Volksschule Spallerhof, Linz

## Professional Experience

01/2018 - Robert Bosch AG, Steyr  
05/2017 - 10/2017 BMW Motoren GmbH, Steyr  
04/2014 - 08/2014 Miba AG, Laakirchen  
07/2006 - 01/2007 Military Service Austrian Army, Hörsching

## Peer-Reviewed Journal Articles

G. Mairinger, A. Frassoldati, R. Gehmlich, U. Niemann, A. Stagni, E. Ranzi, K. Seshadri, Autoignition of Condensed Hydrocarbon Fuels in Nonpremixed Flows at Elevated Pressures, Combustion Theory and Modelling, Pages 995 - 1009 , Volume 20, 2016

G. Mairinger, A. Frassoldati, A. Cuoci, M. Pelucchi, E. Pucher, K. Seshadri, Experimental and Computational Investigation of Autoignition of Jet Fuels and Surrogates in Nonpremixed Flows at Elevated Pressures, Submitted to Proceedings of the Combustion Institute, 2018

G. Mairinger, R. Khare, K. Narayanaswamy, M. Hunyadi-Gall, V. Raghavan, K. Seshadri, Experimental and Computational Investigation of the Influence of Stoichiometric Mixture Fraction on Structure and Extinction of Laminar, Nonpremixed Methoxymethane Flames, Submitted to Proceedings of the Combustion Institute, 2018

*P. Mairhofer, G. Mairinger, K. Seshadri, X.S. Bai, R. Seiser, E. Pucher*, Rate-ratio asymptotic analysis of the influence of stoichiometric mixture fraction on structure and extinction of laminar, nonpremixed methane flames with comparison to experiments, Proceedings of the Combustion Institute, Pages 1495-1503, Volume 36, 2017

### Conference Articles

*G. Mairinger, A. Frassoldati, A. Cuoci, E. Pucher, K. Seshadri*, Autoignition of Jet Fuels and Surrogates in Nonpremixed Flow at Elevated Pressures, 10th U.S. National Combustion Meeting, College Park, Maryland, 2017

*G. Mairinger, A. Frassoldati, R. Gehmlich, U. Niemann, A. Stagni, E. Ranzi, K. Seshadri, E. Pucher*, Autoignition of Condensed Hydrocarbon Fuels in Nonpremixed Flows at Elevated Pressures, 36th International Symposium on Combustion, Seoul, 2016

*G. Mairinger, R. Gehmlich, K. Seshadri, E. Pucher*, Autoignition of n-heptane at moderate pressure, 9th US National Combustion Meeting, Cincinnati, 2015